E-663

Inclusive Production and Polarization of $\Lambda/\bar{\Lambda}$ in Hadron Proton Interactions

By

STEPHEN ALAN GOURLAY

B.S. (Wichita State University) 1976
M.S. (Wichita State University) 1978

DISSERTATION

Submitted in partial satisfaction of the requirements for the degree of

DOCTOR OF PHILOSOPHY

in

Physics

in the

GRADUATE DIVISION

of the

UNIVERSITY OF CALIFORNIA

DAVIS

FERMILAB
LIBRARY

Approved:

Committee in Charge

Deposited in the University Library May 1985
Date Librarian

gift Pieces AAF 0580

Abstract

This experiment measured the polarization of inclusive Λ's and $\bar{\Lambda}$'s produced in the reactions $pp \to \Lambda + X$, $\bar{p}p \to \bar{\Lambda} + X$ and $K^- p \to \Lambda + X$ on liquid hydrogen. It was performed in the M4 beamline at Fermilab with an incident beam momentum of 175 GeV/c and covered the kinematic range of $0.2 < X_F < 1.0$ and $0.0 < P_T < 1.2$.

The results, when compared with previous experiments at different energies, are found to be energy independent. The polarization of Λ's produced by K^-'s has been previously studied at incident beam energies of only 32 GeV and below.* This experiment presents the first data at high energy.

The polarization for $pp \to \Lambda + X$ is positive with respect to the production plane $(\bar{p}_\Lambda \times \bar{p}_{beam})/|\bar{p}_\Lambda \times \bar{p}_{beam}|$, increases with P_T and is approximately 10% at $P_T = 0.8$ GeV/c. As a function of X_F the polarization is consistent with a non-zero value only well into the beam fragmentation region. The $\bar{p}p \to \bar{\Lambda} + X$ channel exhibits behavior that is similar in all respects with the polarization of Λ's produced by protons. In contrast to the baryon-baryon channels the polarization of Λ's produced by K^-'s is opposite in sign and is approximately 60% at $P_T = 0.8$ GeV/c. The polarization is non-zero at relatively lower values of X_F.

An estimate is made on the contribution of non-direct background from $\Sigma^0 \to \gamma\Lambda$ included in the sample. Depending on the polarization of

Σ^0's produced by K^-, which at this time is not known, the polarization of directly produced Λ's could range from 75 → 100%.

The results of the $pp \to \Lambda + X$ and $\bar{p}p \to \bar{\Lambda} + X$ channels agree favorably with current models** as does the sign of the polarization of Λ's produced by K^-'s. However the large magnitude of the polarization found in $K^-p \to \Lambda + X$ is in sharp disagreement with theoretical predictions.

*M.L. Faccini-Turluer et al., Z. Phys. C1, 19 (1979).

M. Baubillier et al., Nucl. Phys. B148, 18 (1979).

H. Abramowicz et al., Nucl. Phys. B105, 222 (1976).

H. Grassler et al., Nucl. Phys. B136, 386 (1978).

S.U. Chung et al., Phys. Rev. D11, 1010 (1975).

**T. DeGrand and H. Miettinen, Phys. Rev. D23, 1227 (1981).

B. Andersson, G. Gustafson and G. Ingelman, Phys. Lett. 85B, 417 (1979).

J. Szwed, Phys. Lett. 105B, 403 (1981).

TABLE OF CONTENTS

Abstract ii

List of Tables vi

List of Figures vii

1. INTRODUCTION 1

1.1 Lambda Physics 3

1.2 Theoretical Models 9

2. APPARATUS 11

2.1 Beamline 11

2.2 Cherenkov Counter 13

2.3 Beam Spectrometer 16

2.3.1 Beam Chamber System 20

2.4 Liquid Hydrogen Target 23

2.5 Forward Spectrometer 25

2.5.1 Proportional Chambers 29

2.5.2 Drift Chambers 32

2.6 Trigger 39

2.6.1 Pre-Trigger 39

2.6.2 Trigger Processor 43

2.6.3 Data Acquisition 47

3. ANALYSIS 48

3.1 Track Finding/Pattern Recognition 48

3.2 Particle Reconstruction and Identification 50

3.3 Monte Carlo 64

3.4 Asymmetry Analysis 81

3.4.1 Coordinate System 81

3.4.2 Analysis Method 86

3.4.3 Biases 89

4. RESULTS AND CONCLUSIONS 92

4.1 Bias Checks 93

4.1.1 A_x, A_y 93

4.1.2 K^0_S Analysis 97

4.2 $pp \to \Lambda$ Results 101

4.3 $\bar{p}p \to \bar{\Lambda}$ Results 109

4.4 $K^- p \to \Lambda$ Results 117

4.5 Systematic Errors/Backgrounds 125

4.6 Discussion 130

ACKNOWLEDGEMENTS 139

REFERENCES 140

LIST OF FIGURES

Figure Page

1.1 Definition of Production Plane and Normal $\hat{n}$ used in this Experiment 3

1.2 Coordinate System in the Λ Rest Frame 5

2.1 Cherenkov Counter 14

2.2 K^- Pulse Height vs $p/\bar{p}$ Pulse Height 15

2.3 Beam Spectrometer 17

2.4 Beam Momentum and Intercept Distributions at the Target 18

2.5 Electric Field and Equipotentials of a Proportional Chamber 20

2.6 Hydrogen Target 23

2.7 Forward Spectrometer 26

2.8 Drift Chamber Cell Structure 34

2.9 Relative Orientation of Drift Chamber Sense Wire Planes 34

2.10 Diagram of Drift Chamber Field 35

2.11 Plot of Drift Velocity vs Electric Field for Argon/CO_2 90/10 ... 35

2.12 Pre-Trigger Logic Diagram 40

2.13 Interaction Counter Hodoscope 42

2.14 Trigger Processor Diagram 44

3.1 Raw Invariant Mass Distributions (no cuts) 58

3.2 x and y Intercepts at Production Vertex 59

3.3 x and y Intercepts at Decay Vertex 60

3.4 z of Production and Decay Verticies 61

3.5 Distance of Closest Approach at Production and Decay 62

3.6 Invariant Mass Distributions After Cuts 63

3.7 Incident Particle Coordinate System and Experiment Coordinate System 69

3.8 x Intercept of the Beam at the Target and x-Slope 73

3.9 y Intercept of the Beam at the Target and y-Slope 74

3.10 Beam Momentum Distribution 75

3.11 Track Intercepts of Decay Products at Analysis Magnet Center ... 76

3.12 Distributions of Transverse Momentum of Decay 77

3.13 Momentum Distributions of $\Lambda, \bar{\Lambda}, K^0_S$ 78

3.14 P_T Distributions of $\Lambda, \bar{\Lambda}, K^0_S$ 79

3.15 X_F Distributions of $\Lambda, \bar{\Lambda}, K^0_S$ 80

3.16 Laboratory Coordinate System 81

3.17 Rest Frame Coordinate System 82

3.18 Precession of Λ Spin in Sweeping Magnet Field 85

3.19 Lambda, $\bar{\Lambda}$ and K^0_S Lifetime vs Momentum 91

4.1 Parity Nonconserving Asymmetries as a Function of P_T 95

4.2 Parity Nonconserving Asymmetries as a Function of X_F 96

4.3 Asymmetry A_x as a Function of X_F and P_T for $K^-p \rightarrow K^0_S$ 98

4.4 Asymmetry A_y as a Function of X_F and P_T for $K^-p \rightarrow K^0_S$ 99

4.5 Asymmetry A_z as a Function of X_F and P_T for $K^-p \rightarrow K^0_S$ 100

4.6 Parity Conserving Asymmetry A_z as a Function of P_T and X_F for $pp \rightarrow \Lambda$ Magnet Up/Magnet Down Data 103

4.7 Parity Conserving Asymmetry A_z as a Function of P_T and X_F for $pp \rightarrow \Lambda$ Combined Data 104

4.8 Polarization as a Function of P_T and X_F for $pp \rightarrow \Lambda$ 105

4.9 Polarization as a Function of P_T and X_F for $pp \rightarrow \Lambda$ with Fits ... 106

4.10 Comparison of Polarization for $pp \rightarrow \Lambda$ from this Experiment and Reference 18 108

4.11 Parity Conserving Asymmetry A_z as a Function of P_T and X_F for $\bar{p}p \rightarrow \bar{\Lambda}$ Magnet Up/Magnet Down Data 110

4.12 Parity Conserving Asymmetry A_z as a Function of P_T and X_F for $\bar{p}p \rightarrow \bar{\Lambda}$ Combined Data 111

4.13 Polarization as a Function of P_T and X_F for $\bar{p}p \rightarrow \bar{\Lambda}$ 112

4.14 Polarization as a Function of P_T and X_F for $\bar{p}p \rightarrow \bar{\Lambda}$ with Fits 113

4.15 Comparison of Polarization for $\bar{p}p \rightarrow \bar{\Lambda}$ with $pp \rightarrow \Lambda$ 115

4.16 Comparison of Polarization for $\bar{p}p \rightarrow \bar{\Lambda}$ from this Experiment and Reference 20 116

4.17 Parity Conserving Asymmetry A_z as a Function of P_T and X_F for $K^-p \rightarrow \Lambda$ Magnet Up/Magnet Down Data 119

4.18 Parity Conserving Asymmetry A_z as a Function of P_T and X_F for $K^-p \rightarrow \Lambda$ Combined Data 120

4.19 Polarization as a Function of P_T and X_F for $K^-p \rightarrow \Lambda$ 121

4.20 Polarization as a Function of P_T and X_F for $K^-p \rightarrow \Lambda$ with Fits 122

4.21 Comparison of Polarization for $K^-p \rightarrow \Lambda$ from this Experiment and Reference 22 123

4.22 Comparison of Polarization for $K^-p \rightarrow \Lambda$ from this Experiment and $K^+p \rightarrow \bar{\Lambda}$ from Reference 26 124

4.23 Measured and Direct Polarization as a Function of P_T for $pp \rightarrow \Lambda$ 129

4.24 Polarization of Λ's and Σ^0's Produced by K^- for Possible Values of the Measured Polarization 129

4.25 Summary of Polarization Results 134

SECTION 1

INTRODUCTION

At high energies the major part of the total cross section is due to high multiplicity inelastic interactions. Thus, in attempting to study these interactions we are faced with an overwhelming number of variables and must find ways to summarize the angular and momentum distributions of these particles. An old and simple approach is to select one particle, in this case a lambda (Λ) or anti-lambda ($\bar{\Lambda}$), and integrate over the kinematic parameters of all the other particles in the interaction. Such interactions are referred to as inclusive interactions.

The study of inclusive interactions takes on many forms and the unexpectedly high Λ polarization first discovered at Fermilab [1] yields another method to organize and present this data. The identification and study of any special regularities which appear to be empirically true that apply to very high energy phenomena may help contribute to our overall understanding and eventually lead the way to an ultimate dynamical theory.

This particular experiment investigates the hadronization process of the constituent particles (quarks) into a Λ or $\bar{\Lambda}$. In the context of the quark model the Λ is composed of a u-, d-, and an s-quark where the u and d form a spin-singlet state, so that the spin and the polarization of the Λ are those of the strange quark. Studies of Λ polarization

therefore provide information on the dynamical behavior of the s-quark.

The aim of this experiment was to compare the polarization of Λ's and $\bar{\Lambda}$'s inclusively produced in the following interactions;

$$p + p \rightarrow \Lambda + X$$

$$\bar{p} + p \rightarrow \bar{\Lambda} + X$$

$$K^- + p \rightarrow \Lambda + X$$

where X denotes all other particles produced.

The incident beam momentum of 175 GeV/c represents a new region for the study of inclusive polarization phenomena and in the case of $K^- p \rightarrow \Lambda + X$ is the first measurement at high energy.

Systematic effects which are of prime concern in polarization experiments are studied using several methods. The primary techniques are mentioned here and detailed later in Section 4.1 along with additional checks.

A large sample of $K^0_S \rightarrow \pi^+ + \pi^-$ decays was obtained using the same apparatus. The K^0_S's, which are unpolarized, were subjected to the same analysis procedure as that used for Λ's and $\bar{\Lambda}$'s. A calibration check was made by comparing the results for $pp \rightarrow \Lambda + X$ with the well-known results of previous experiments.

1.1 Lambda Physics

Production

Lambdas and $\bar{\Lambda}$'s are produced via the strong interactions which conserve parity. Therefore the spin of the Λ or $\bar{\Lambda}$ must be perpendicular to the production plane which is defined by $\hat{n} = (\bar{p}_\Lambda \times \bar{p}_{beam})/|\bar{p}_\Lambda \times \bar{p}_{beam}|$ (Figure 1.1). Any other orientation with respect to the production plane would in general violate parity conservation.

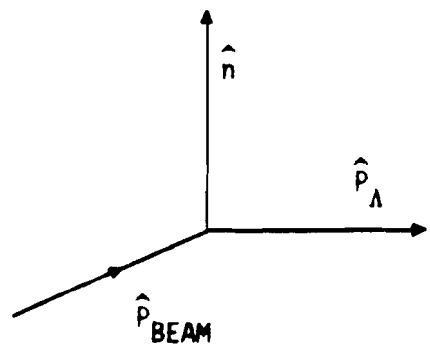

Figure 1.1 Definition of Production Plane and Normal $\hat{n}$ used in this Experiment.

The polarization is defined as $P = (N_+ - N_-)/(N_+ + N_-)$, where

N_+ = number of Λ's produced with spins in the $\hat{n}$ direction

and

N_- = number of Λ's produced with spins opposite $\hat{n}$.

A non-zero polarization would imply that Λ's or $\bar{\Lambda}$'s are produced preferentially with spins in one direction.

Decay

In contrast to its production the Λ decays via the weak interaction and therefore parity conservation is not required. The Λ is particularly suited to polarization measurements because it serves as its own spin analyzer through the π,p decay mode which has a branching ratio of approximately 2/3.

The Λ and proton each have spin 1/2 which allows the pion and proton to have relative orbital angular momentum $\ell = 0$ or $\ell = 1$. The mixture of these two angular momentum states gives rise to the parity non-conserving decay distribution. In the derivation below we assume that the spin vector of the Λ , $\hat{s}$, is collinear with the normal to the production plane as required by parity conservation in the production of the Λ.

We define

$$\hat{n} = (\bar{p}_\Lambda \times \bar{p}_{beam})/|\bar{p}_\Lambda \times \bar{p}_{beam}|$$

as the z-axis of the Λ rest frame and θ = the angle between the Λ spin and pion momentum vector (Figure 1.2).

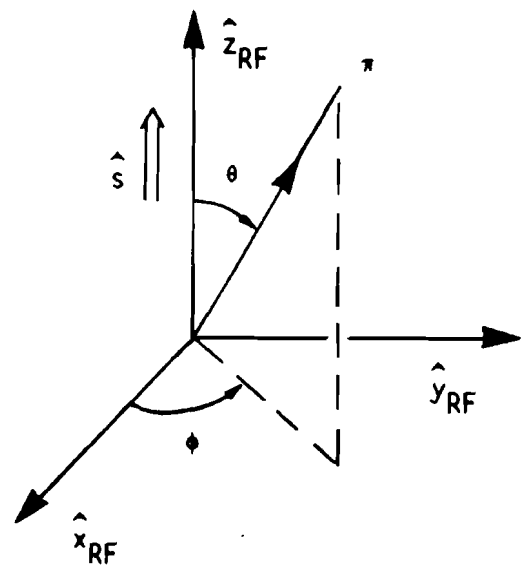

Figure 1.2. Coordinate System in the Λ Rest Frame.

Let m, m' be the z-components of the proton spin and angular momentum respectively. For the $\ell = 0$ (S-state) m' = 0 and the angular part of the wave function is $y_{\ell m'} = Y_0^0$. If the Λ spin is in the +z-direction ($J_z = +1/2$) the total wave function for the S-state is $\psi_s = a_s Y_0^0 \chi^+$ where a_s is the S-state amplitude and χ^+ represents the m = +1/2 state of the proton. For the ℓ=1 (P-state) there are two possibilities for $J_z = +1/2$, m = +1/2 and m' = 0 or m = -1/2 and m' = +1. Combining these two possibilities we have for the P-state wave function

$$\psi_p = a_p\left[\sqrt{\frac{2}{3}}\, Y_1^1 \chi^- - \sqrt{\frac{1}{3}}\, Y_1^0 \chi^+\right].$$

The total wave function combining both S- and P-states is

$$\psi_T = \psi_S + \psi_P = a_S Y_0^0 \chi^+ - \sqrt{\tfrac{1}{3}} a_P Y_1^0 \chi^+ + \sqrt{\tfrac{2}{3}} a_P Y_1^1 \chi^-.$$

Using the orthogonality properties of χ^+ and χ^- we obtain an angular distribution of

$$I^+(\theta) = 1 + \alpha \cos\theta$$

where

$$\alpha = 2a_S R_e a_P^*/(|a_S|^2 + |a_P|^2) = -0.642 \text{ [2]}$$

and is referred to as the analyzing power. In contrast the analyzing power for the Σ^- is 0.07. It should be mentioned now and will be reiterated later that due to the dominance of CP invariance in the weak interactions the sign of α for Λ decay is opposite in sign to α for $\bar{\Lambda}$ decay.

Now, if we take the Λ spin in the negative z-direction $\cos\theta$ changes sign and we have

$$I^{-}(\theta) = 1 - \alpha\cos\theta.$$

Therefore, if we have a statistical mixture of Λ's polarized along the positive and negative z-direction with average polarization P, the angular distribution of the pions becomes

$$I(\theta) = 1 + \alpha P\cos\theta.$$

In general the decay distribution of an ensemble of polarized Λ's or $\bar{\Lambda}$'s may be written

$$\frac{dn}{d\Omega} = \frac{1}{4\pi}\,[1 + \alpha\hat{P}\cdot\hat{n}]$$

and expanded as

$$\frac{dn}{d\Omega} = \frac{1}{4\pi}\,[1 + A_x\sin\theta\cos\phi + A_y\sin\theta\sin\phi + A_z\cos\theta]$$

where $A_x = \alpha P_x$, $A_y = \alpha P_y$ and $A_z = \alpha P_z$.

The asymmetries A_x and A_y represent the parity nonconserving asymmetry components which are zero since parity is conserved in Λ and $\bar{\Lambda}$ production. However, as described in Section 3.4 these components are extracted from the decay distribution as one of several bias checks performed on the data.

1.2 Theoretical Models

A model proposed by DeGrand and Miettinen [3] uses the parton model and SU(6) symmetry to relate polarizations in inclusive baryon production independent of quark dynamics.

In their model they formulate a rule that explains the observed polarizations of hyperons and makes predictions for the interactions studied in this experiment. They find that the existing data are explained by the simple rule that slow partons preferentially recombine with spins down in the scattering plane ($\bar{p}_{beam} \times \bar{p}_{\Lambda}$) while fast partons recombine with their spins up. Thus a valence s-quark, as in $K^- p \rightarrow \Lambda$ would have a polarization of sign opposite to that of sea s-quarks as in $pp \rightarrow \Lambda$ and $\bar{p}p \rightarrow \bar{\Lambda}$. The reaction $K^- p \rightarrow \Lambda$ at large X_F is an important test of the above since the leading s-quark carries all the asymmetry.

In an attempt to explain the origin of the polarization and the rule which relates various baryon polarizations they note that the velocity vector of the s-quark is not parallel to the change in momentum induced by the recombination. This implies that the quarks spin will undergo a Thomas precession which will add an $\bar{s}\cdot\bar{\omega}_T$ term to the Hamiltonian which is proportional to P_T. It is then expected that the scattering amplitude will depend on $\bar{s}\cdot\bar{\omega}_T$, whether the spin of the s-quark is up or down in the scattering plane. Building on these arguments they predict that the polarization will depend approximately linearly on P_T and weakly on X_F.

Another semiclassical model was proposed by Andersson, Gustafson, and Ingelman [4] which is less general in scope as it has been applied only to the polarization of Λ's produced by protons. They incorporate SU(6) with a string model description of the interactions among the

quarks forming the Λ. The correlation between the transverse momentum of the s-quark pulled from the sea and the transverse momentum of the Λ then gives rise to a polarization. Szwed [5] explains polarization in inclusive and exclusive processes by multiple scattering of the strange quark. Other models exist [6,7,8] which have varying success.

SECTION 2

APPARATUS

The parameters necessary for the study of Λ and $\bar{\Lambda}$ polarization were obtained using a dual spectrometer system. A "beam" spectrometer identified and measured the momentum and direction of the incident particle and a "forward" spectrometer detected interactions in the liquid hydrogen target and was used to reconstruct the subsequent decays of Λ's, $\bar{\Lambda}$'s, and K^0_S's.

2.1 Beamline

The hadrons used for this experiment were obtained from a secondary beam produced by focussing the 400 GeV/c primary protons from the main ring onto a 1.5 mm × 1.5 mm × 203 mm beryllium target. The secondary particles produced in the "meson target" were divided into six separate beamlines. The M4 beamline used in this experiment had been converted earlier from a neutral beam [9].

The particles produced at the meson target were transported 521 m via a series of quadrupoles, dipoles, and collimators to the hydrogen target of the experiment where it formed a spot 2.8 cm in the x (transverse) direction and 2.6 cm vertically. The beam had a momentum band of approximately 14% and a transmitted solid angle of 0.66×10^{-6} steradians.

The beam momentum of 175 GeV/c, chosen to maximize the transverse acceptance, was the highest momentum obtainable without unacceptable loss of image quality or solid angle. Increasing the momentum of the secondary beam produced Λ's and $\bar{\Lambda}$'s with higher average momentum which led to smaller opening decay angles in the lab.

Muons produced by the decay of low momentum pions near the meson target were used to calibrate and align the apparatus. The hadrons of the secondary beam were eliminated by dropping a large steel block (beam stop) into the beam, allowing only muons and neutrinos to pass through.

The low total flux required, 10^6-10^7 particles per second/10 second spill, to be able to identify particles and measure their momentum and position made the M4 line preferable to existing hadron beams. The production angle of 8 milliradians, while reducing the total flux, enhanced the fraction of K^-'s and $\bar{p}$'s of the negative beam.

The composition of the negative beam was approximately 6% K^-, 3% $\bar{p}$ with the balance π^-. When running in the positive beam configuration for the study of $pp \rightarrow \Lambda$ the composition was predominantly diffractively scattered protons from the meson target.

2.2 Cherenkov Counter

Incident particles were separately identified using a differential Cherenkov counter (Figure 2.1). Modeled after a design by S. Pruss of Fermilab the counter consisted of a 2.5 meter focal length primary mirror that focussed the ring image on a secondary flat mirror which had a circular hole centered on the reflected ring axis. The counter was tuned such that light from the faster K^-'s was reflected onto a second phototube. The secondary mirror was fitted with a black mask that covered all of the mirror with the exception of a narrow ring around the hole preventing the detection of scattered light from pions. For operation at 175 GeV/c the radiator was He contained in a 75 m beam pipe. Pulse height distributions indicated that on the average six photoelectrons were collected. The degree of discrimination of $p/\bar{p}$'s and K^-'s can be seen in a scatter plot of K^- pulse height vs $p/\bar{p}$ pulse height (Figure 2.2). Approximately one out of 2000 events gave an ambiguous Cherenkov signal.

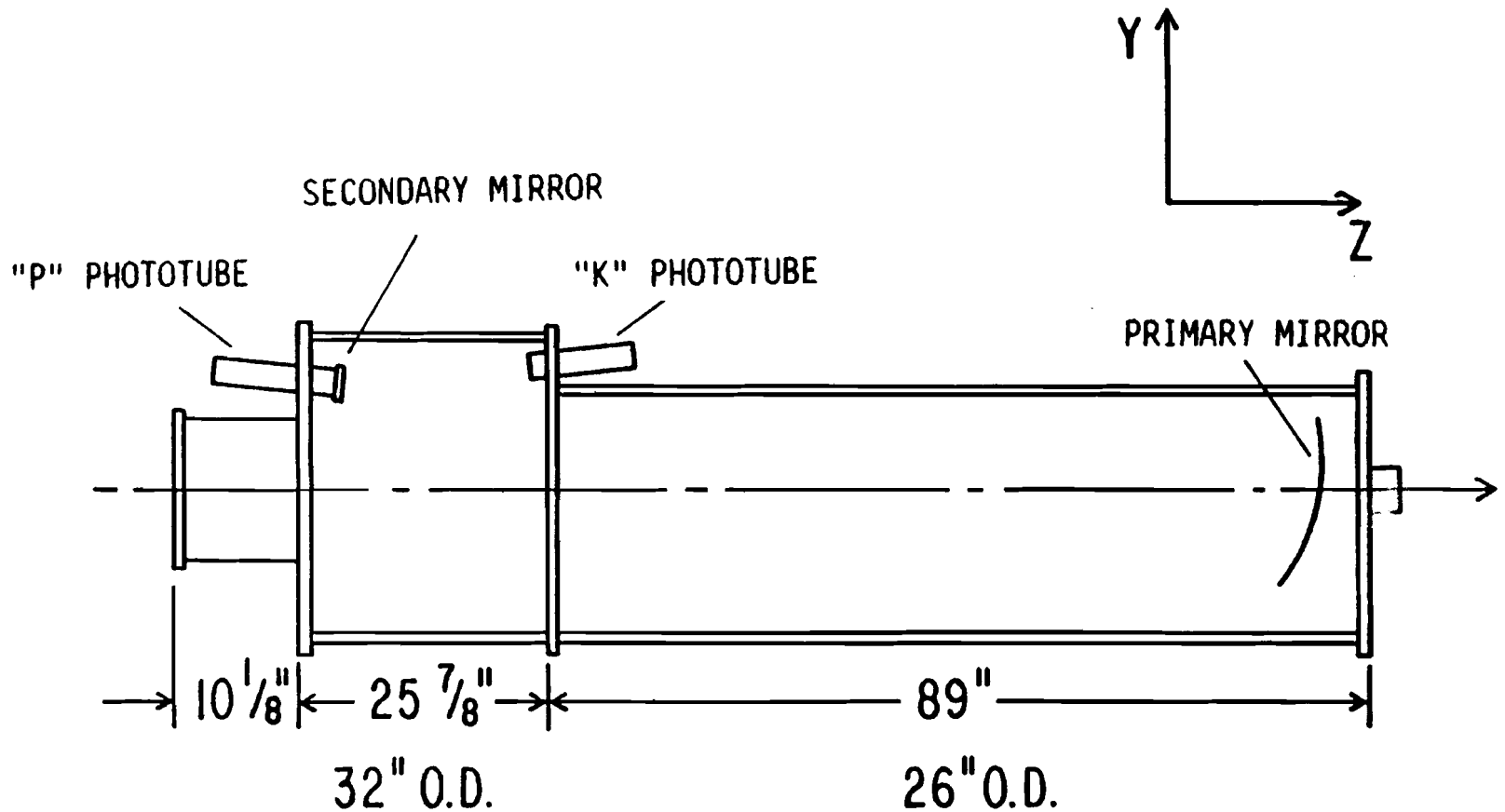

Figure 2.1. Cherenkov Counter.

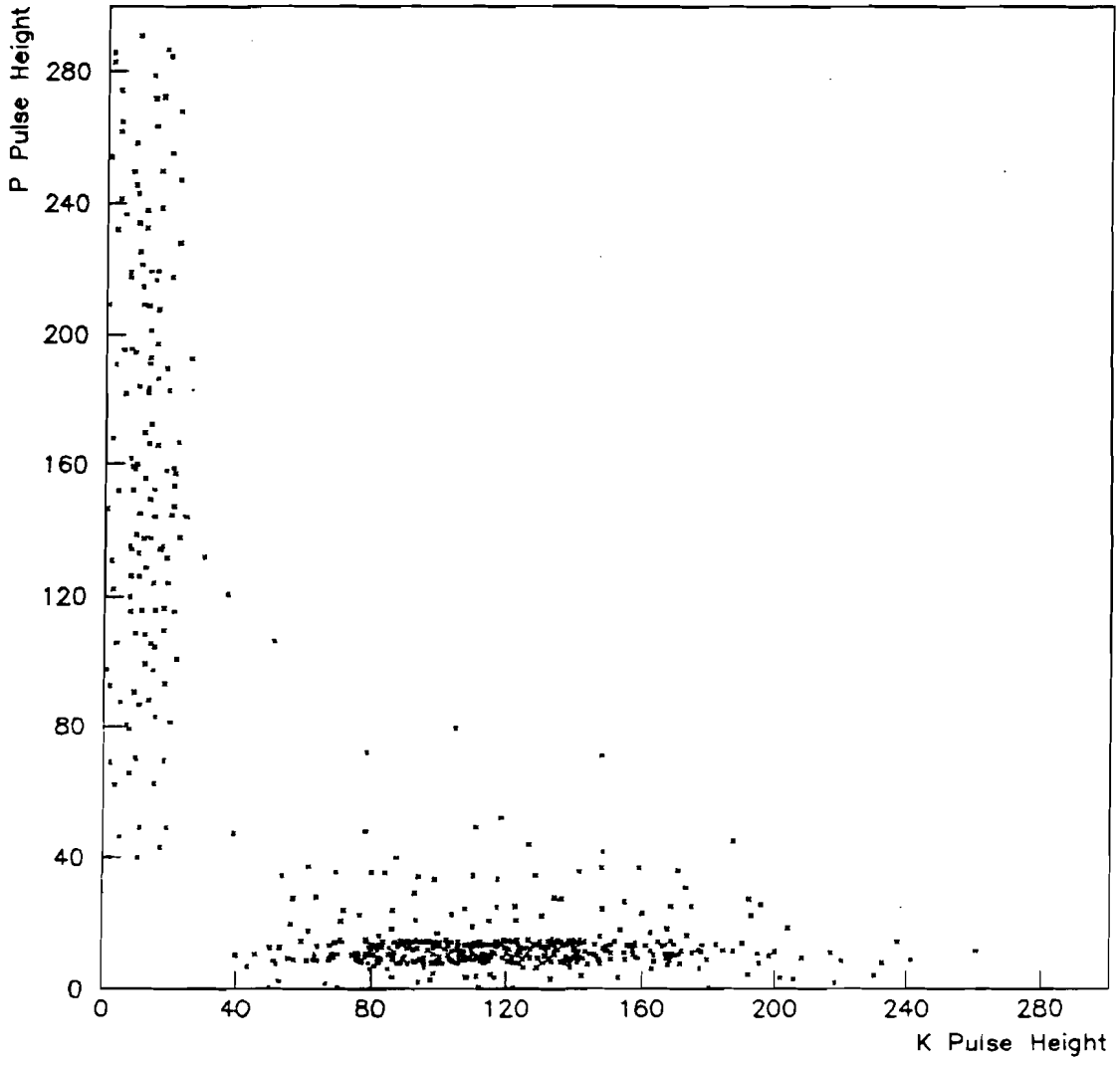

Figure 2.2. K^- Pulse Height vs $p/\bar{p}$ Pulse Height.

2.3 Beam Spectrometer

The polarization of Λ's and $\bar{\Lambda}$'s is measured with respect to the production plane which makes it necessary to know the position and momentum of the incident particle relative to the neutral V produced downstream of the hydrogen target.

The beam spectrometer system is shown in Figure 2.3. The existence of a beam particle was determined by a coincidence of signals from three 1/4" thick 60 × 30 mm (x,y) plastic scintillation counters (B_1, B_2, B_3) and anti-coincidence of a 1/4" thick counter with a 1" square hole centered on the beam to eliminate beam halo events, labeled "H".

The momentum of the secondary beam ranged from 160 - 200 GeV/c with a mean of 175 GeV/c and width δp = 6 GeV/c. The beam profile at the hydrogen target had a vertical spread, δy = 5 mm, and a horizontal spread, δx = 5.5 mm. The beam spot intersected approximately 10% of the surface of the target. The momentum and intercept distributions for the negative beam are shown in Figure 2.4. The tails of the intercept distributions were cut off due to the "H" counter located 7.335 m upstream of the target. Resolutions of important parameters are given in Table 3.2 at the end of Section 3.3.

The momentum and direction of the beam were measured with 4 x,y planes of proportional chambers and two bending magnets. The magnets were operated from the same power supply in series with opposite field integrals giving a net translation of the beam in the positive x-direction of 14 cm. The z-locations of the beam spectrometer elements, defined relative to the analysis magnet center, are given in Table 2.1.

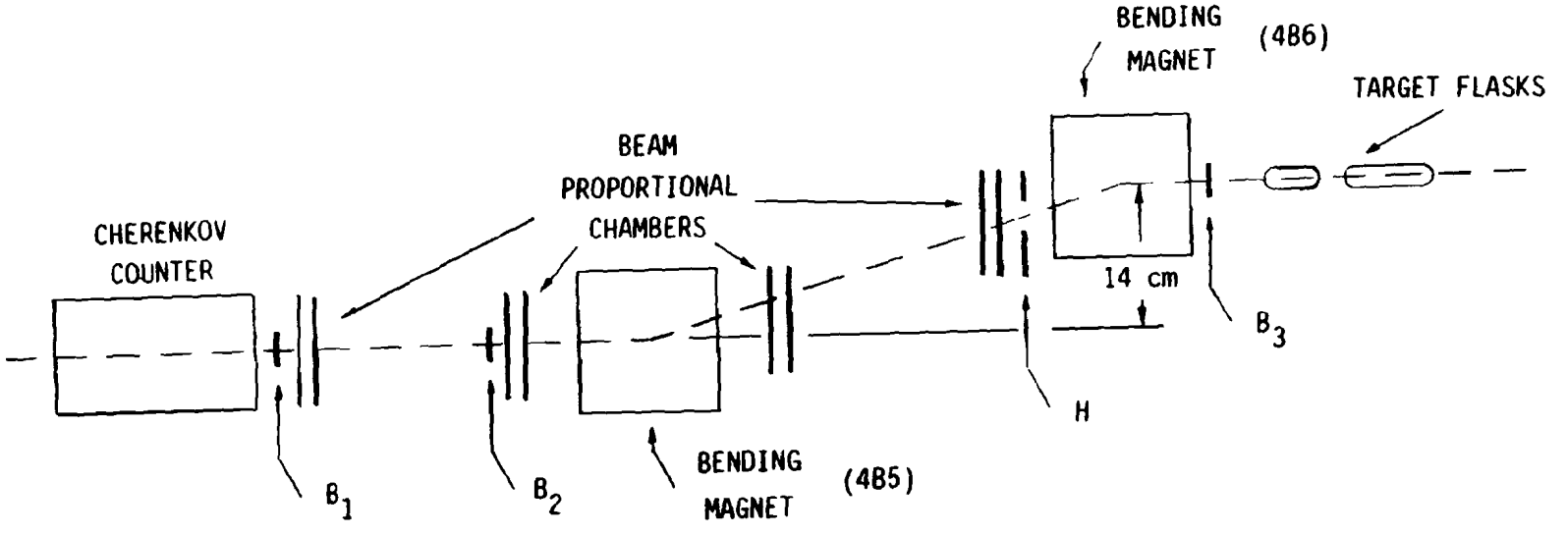

Figure 2.3. Beam Spectrometer.

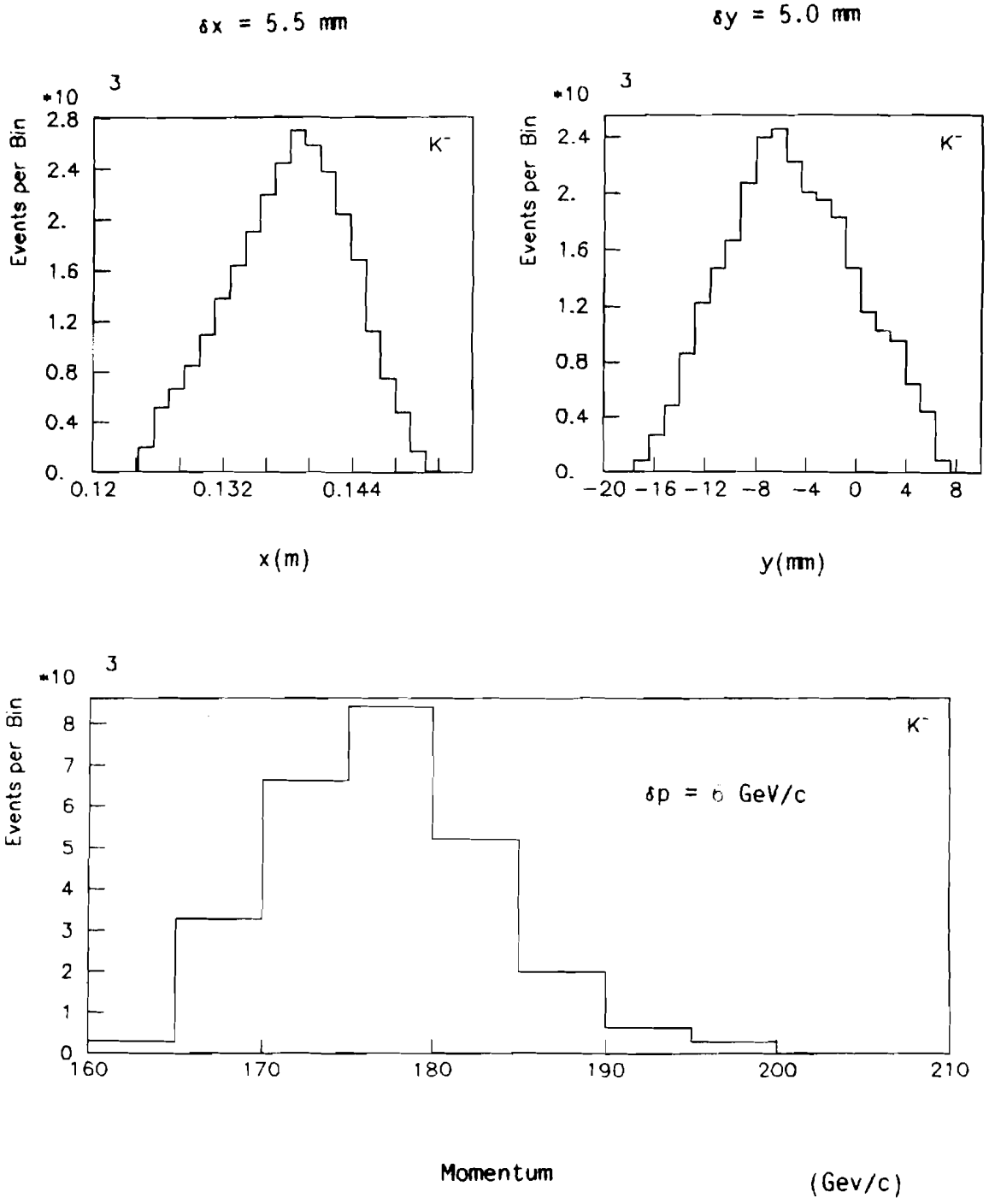

Figure 2.4. Beam Momentum and Intercept Distributions at the Target.

Table 2.1. z-Locations of Beam Spectrometer Elements.

Element		z (meters)
Cherenkov Counter	(Downstr. Face)	-61.074
B1 Counter		-60.737
Beam Chamber 1X	(Wire Plane)	-60.548
Beam Chamber 1Y	(Wire Plane)	-60.353
B2 Counter		-48.064
Beam Chamber 2X	(Wire Plane)	-47.921
Beam Chamber 2Y	(Wire Plane)	-47.705
4B5 Magnet	(Upstr. Face)	-47.237
4B5 Magnet	(Center Line)	-45.713
4B5 Magnet	(Downstr. Face)	-44.189
Beam Chamber 3X	(Wire Plane)	-43.761
Beam Chamber 3Y	(Wire Plane)	-43.576
Halo Counter		-31.548
Beam Chamber 4X	(Wire Plane)	-31.307
Beam Chamber 4Y	(Wire Plane)	-31.112
4B6 Magnet	(Upstr. Face)	-30.548
4B6 Magnet	(Center Line)	-29.274
4B6 Magnet	(Downstr. Face)	-27.750
B3 Counter		-27.499
Target	(Upstr. Aluminum Face)	-27.213

2.3.1 Beam Chamber System

The devices used to measure the location of a passing incident charged particle are referred to as "beam chambers." Detectors of this general type are called proportional wire chambers or PWC's which make use of the electromagnetic interaction of charged particles with atomic electrons. The chamber consists of a plane of 64 "sense" wires or anodes spaced 1 mm apart at ground potential. The sense plane is sandwiched between two cathode planes of 0.04 mm aluminum foil maintained at a potential of approximately -5.3 kV. A diagram of the electric field, which has a 1/r dependence near the sense wire, and equipotentials for a proportional chamber is shown in Figure 2.5.

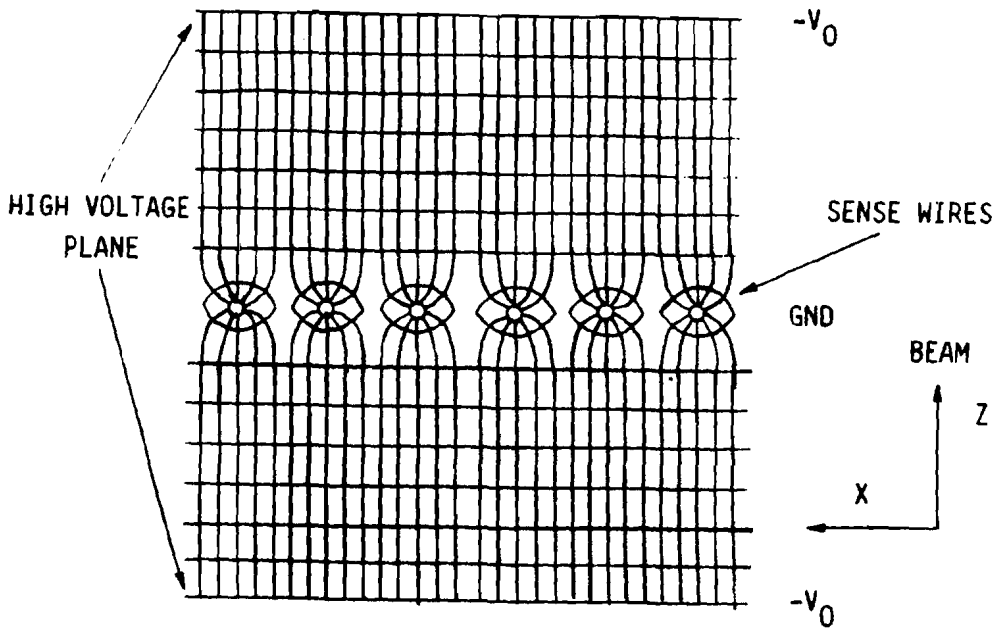

Figure 2.5. Electric Field and Equipotentials of a Proportional Chamber.

The sense wires form an array of nearly independent detectors. If they were totally independent the resolution of the chamber would be $s/\sqrt{12}$ where s is the wire spacing. However, if a particle passes through a region centered between wires both wires will be "hit" and the resolution can be better than $s/\sqrt{12}$ depending on the size of the sharing region, which is a function of the voltage and physical characteristics of the chamber.

Charge multiplication takes place in the high fields surrounding the wire which induces a signal on the anode or sense wire. The signal is amplified and converted to a digital pulse which is saved for subsequent transferral to the on-line computer via the beam chamber read out system. The chambers were constructed by the Research Services Department at Fermilab. A gas mixture of 20% CO_2, 0.15% Freon 13B1 with a balance of Argon was used. Efficiencies of the chambers were approximately 98% during data taking.

The relatively high rate of beam (10^5 - 10^6 particles per second) necessitated the ability to record multiple wire signals in the beam chambers. This required the use of fast memory units. Each chamber is connected to a 64-channel memory unit that records the condition of each wire at 50 ns intervals in 16 words of memory. The words are addressed sequentially with the newest information overwriting the oldest. Thus at any one time 16 × 50 = 800 ns of the history of a given wire was stored in the memory system. The memory circuits of each chamber were controlled by a 20 MH_z memory system clock distributed from a memory control module. On receiving a "trigger," indicating a desirable event, the memory system clock is interrupted at the end of the current memory cycle. This initiated the parallel loading of data into a linear array

of storage devices called shift registers. The loading of the data is timed relative to the event trigger for each beam chamber memory unit. The data was shifted out serially using a commercially available CAMAC module called a scanner [10]. The address of a given hit wire is determined in the scanner by counting the transport clock pulses arriving with the data. The addresses are stored in the scanner module until read out by the on-line computer through the CAMAC system. More details of the system may be found in Reference 11.

2.4 Liquid Hydrogen Target

A diagram of the liquid hydrogen target used in this experiment is shown in Figure 2.6. The target was built by the Hydrogen Target Group at Fermilab and consisted of two flasks, one 25.4 cm and one 45.7 cm made of 0.127 mm Mylar. The two flasks were surrounded by a 0.127 mm Mylar vacuum window and a foam vacuum vessel made of 1.91 cm foam and 0.254 mm Mylar on the sides and tapering to 1.27 cm foam and 0.127 mm Mylar on the downstream end.

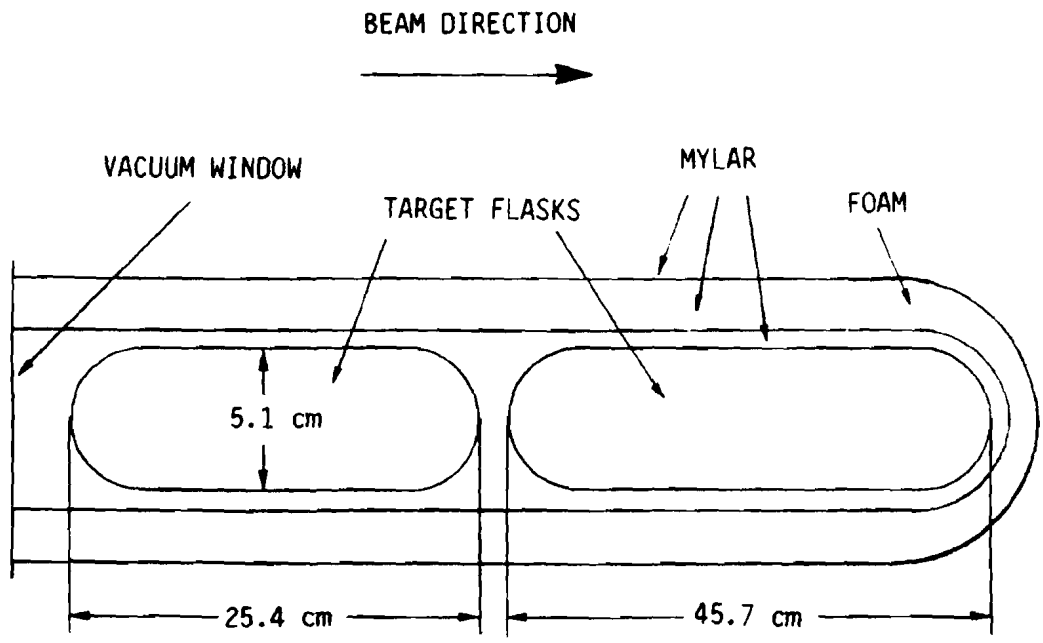

Figure 2.6. Hydrogen Target.

The two-flask configuration was used in previous experiments for detailed background studies. In this experiment all data were taken with both flasks full. The background rate from interactions in the material surrounding the target was about 10% of the rate with both flasks full on Hydrogen. For K^-p interactions the 71.1 cm's of hydrogen represented 0.06 interaction lengths and for pp or $\bar{p}p$ interactions it was 0.12 interaction lengths. When cold and evacuated, the flasks contracted by 0.3%. In this experiment the target vapor pressure was 15 psi, indicating a density of 0.0708 gm/cm^3 and a temperature of 26K.

2.5 Forward Spectrometer

Once the beam spectrometer has determined that an incident particle of the desired type has intersected the hydrogen target the forward spectrometer (Figure 2.7) performs the task of first, deciding if an interaction occurred and second, it establishes as much as possible the existence of a neutral V. The counters and detectors of the spectrometer record the information necessary to reproduce the kinematics of the interaction and, if they exist, reconstruct the decays of Λ's, $\bar{\Lambda}$'s and K^0_S's.

Since only neutral particles were desired immediately downstream of the interaction point, a magnet of $P_\perp$ = 0.785 GeV/c was placed 1.15 m from the center of the hydrogen target to sweep directly produced charged particles out of the spectrometer. The aperture of the magnet was 25.4 cm × 15.2 cm and was 1.83 m in length.

The neutral particles, unaffected by the magnetic field with the exception of precession of the Λ or $\bar{\Lambda}$ spin (see Section 3.4.1), were allowed to decay in a 14.6 m evacuated pipe. The vacuum decay pipe was sealed at each end by an aluminum window. The window closest to the target (upstream) had a diameter of 30.5 cm and was 0.08 mm thick. The pipe increased in diameter to 90.8 cm at the downstream end and was capped with a 0.8 mm thick window.

Four stations of detector planes were placed symmetrically around an analyzing magnet of $p_\perp$ = 0.2 GeV/c. The analysis magnet pole face was 1 m along the beam direction with a useful aperture of 1.18 m × 0.53 m. Both the sweeper and the analyzing magnet bent particles in the x plane.

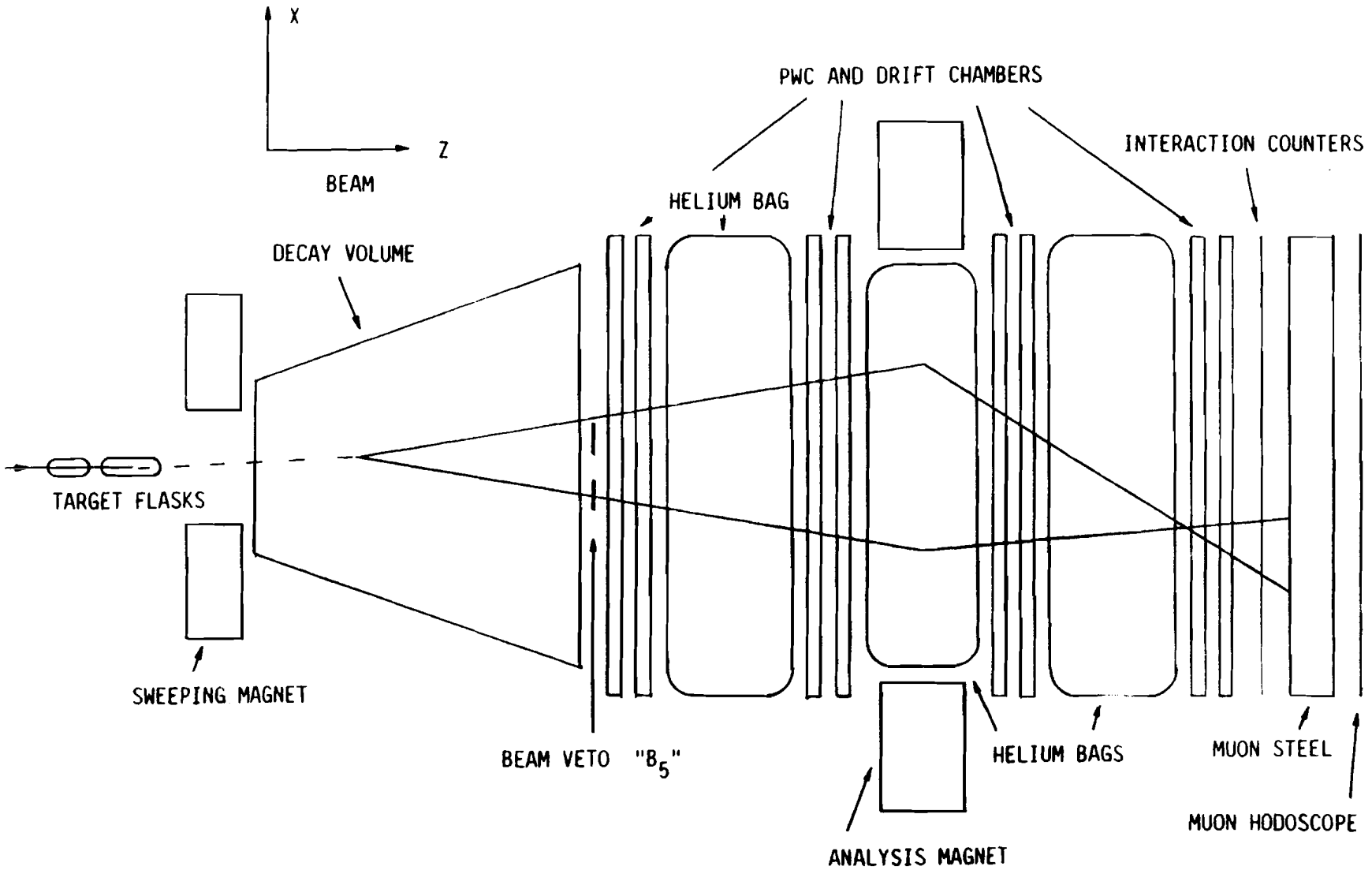

Figure 2.7. Forward Spectrometer.

Each of the four stations consisted of one x and one y proportional chamber and two packages of drift chamber planes. One package contained X,Y planes and another U,V planes with wires rotated 45° with respect to the x,y view. Helium bags with 0.127 mm polyethylene windows were placed between the chamber stations to reduce absorption and multiple scattering. The helium bags placed between the chamber stations upstream and downstream of the analysis magnet were 4.5 m long. The bag inside the aperture of the analysis magnet was 2 m long. Replacement of the air in the volume between the chambers by the 4.5 m bags reduced the effective radiation length by more than a factor of 10.

Downstream of the last chamber station was a hodoscope of scintillation counters (called I-counters) used as part of the fast trigger to indicate an interaction in the target. A hole in the hodoscope prevented triggering on non-interacting particles. Alternating with thick steel blocks were two sets of scintillator hodoscopes used to trigger on muons traversing the apparatus which were used for calibration and alignment purposes.

The z-locations of the detector elements of the forward spectrometer are shown in Table 2.2.

Table 2.2. z-Locations of Forward Spectrometer Elements.

Element	z (meters)
Target, Upstr. Aluminum Face	-27.213
Decay Pipe, Upst. Face of Flange	-22.925
Decay Pipe, Upst. Face of Downst. Flange	- 8.315
PWC 1X	- 7.833
PWC 1Y	- 7.689
B5 Counter	- 7.212
Drift Chamber 1X	- 7.036
Drift Chamber 1Y	- 6.960
Drift Chamber 1U	- 6.704
Drift Chamber 1V	- 6.628
Drift Chamber 2V	- 1.878
Drift Chamber 2U	- 1.802
Drift Chamber 2Y	- 1.712
Drift Chamber 2X	- 1.636
PWC 2Y	- 1.415
PWC 2X	- 1.215
Analysis Magnet (Geometrical Center)	0.000
Analysis Magnet (Magnetic Center)	0.040
PWC 3X	1.775
PWC 3Y	1.924
Drift Chamber 3X	2.119
Drift Chamber 3Y	2.195
Drift Chamber 3U	2.298
Drift Chamber 3V	2.374
Drift Chamber 4V	7.123
Drift Chamber 4U	7.199
Drift Chamber 4Y	7.300
Drift Chamber 4X	7.376
PWC 4X	7.592
PWC 4Y	7.744
Interaction Counters	8.381
Muon Hodoscope (Front)	11.225
Steel, 1st Block, Upst. Face	11.740
Steel, 2nd Block, Downst. Face	15.571
Muon Hodoscope (Rear)	15.715

2.5.1 Proportional Chambers

The proportional chambers used in the forward spectrometer incorporate the same physics in their operation as the beam chambers described in Section 2.3.1. The basic difference is the size, which ranges from 0.78 m to 1.5 m for the large PWC's compared to 0.064 m for the beam PWC's. The large size produces problems of stability. The electromechanical instabilities were eliminated by increasing the diameter of the outside wires in the sense plane which sacrificed some efficiency. Each chamber also had support wires of AWG 30 wire-wrap wire glued perpendicular to the sense wires.

The sense wire plane was composed of 20 or 25 μ gold-plated tungsten wires at 45 grams tension spaced 2 mm apart. The high voltage or cathode plane was made of 64 μ phosphor-bronze wires at 150 gms tension with 1 mm spacing oriented perpendicular to the sense wires. The typical cathode voltage was -4.5 kV. The gas used was the same as for the beam proportional chambers.

The sense wire diameter and number of wires in each of the four types of planes used is shown in Table 2.3.

Table 2.3. Number and Size of Proportional Chamber Sense Wires.

Chamber	Sense Wire Diameter	Number of Wires
upstream X	25 microns	576
upstream Y	25 microns	384
downstream X	20 microns	768
downstream Y	20 microns	576

upstream and downstream are with respect to the analysis magnet)

The ionization electrons produced by a charged particle passing through a chamber are multiplied by gas amplification in the vicinity of the sense wire. This signal is amplified to produce a +3.5 V, 60 ns pulse that fires a one-shot. A one-shot is a solid-state device that emits a digital pulse when it sees a voltage transition at its input, in this case the amplified signal from a sense wire. It will not fire again until it receives a reset signal allowing it to accept another pulse. A subsequent event "trigger" would then send a 290 ns load pulse that latched the one-shot output into a shift register chain. A 10 MH_z clock generated by a scanner module for each chamber synchronously shifted the data through the shift register chain. Clusters of hits were converted by the scanner module from a binary pattern to an address of the last wire of the cluster along with the cluster length. The data could then be efficiently transferred to the on-line computer via CAMAC. The resolutions and efficiencies of the proportional chambers are give in Table 2.4.

Table 2.4. Proportional Chamber Efficiencies and Resolutions.

Plane	Efficiency	Resolution
1X	0.98	534μ
1Y	0.94	536μ
2X	0.98	538μ
2Y	0.95	543μ
3X	0.97	546μ
3Y	0.96	529μ
4X	0.93	504μ
4Y	0.94	530μ

2.5.2 Drift Chambers

Each of the four chamber stations contained two sets of drift chamber planes, (X, X', Y, Y') and (U, U', V, V'). The sense wires, 20 μ gold-plated tungsten, of the primed and unprimed planes were offset from each other by 1/2 the spacing between adjacent sense wires (1 cell length = 49.21 mm) (Figure 2.8). The sense wires of the (U, U', V, V') package were rotated at 45° with respect to those of the (X, X', Y, Y') package (Figure 2.9).

Ionization electrons created in the gas drifted to the sense wire, which was at ground potential, in a uniform electric field of 1.2 kV/cm provided by a plane of 100 μ beryllium copper high voltage wires 3.18 mm apart and spaced 4.76 mm from the sense wire plane. The voltage for each wire was distributed through a linear resistor chain to obtain the required uniform field (Figure 2.10).

The four planes in a package comprised a gas enclosure with windows of 0.003" Mylar laminated with 0.001" Aluminum. The gas used was 10% CO_2, 0.15% Freon 13B1 and a balance of Argon. Gasses with a higher organic content tend to grow "whiskers" on the wires. One of the drawbacks of this gas is that the drift velocity depends more strongly on the electric field than it does in some hydrocarbon mixtures. Figure 2.11 shows the drift velocity as a function of electric field. With a field of 1.2 kV/cm used for these chambers the drift velocity was approximately 44 cm/μs.

The package sizes and the number of sense wires in each plane is shown in Table 2.5. There were a total of 420 sense wires in the drift chamber system.

Table 2.5. Package Sizes and Number of Wires in Each Drift Chamber Plane.

Upstream Chambers 120 × 175 cm		Downstream Chambers 150 × 120 cm	
Plane	Number of Wires	Plane	Number of Wires
X	12	X	15
X'	12	X'	15
Y	8	Y	12
Y'	8	Y'	12
U	13	U	16
U'	13	U'	16
V	13	V	16
V'	13	V'	16

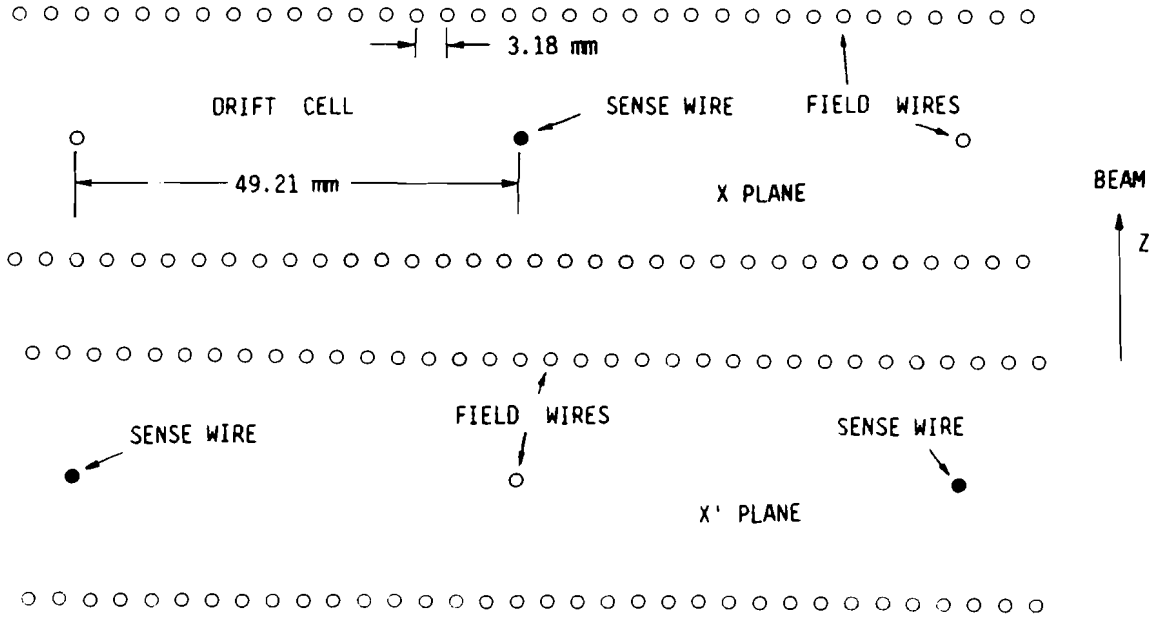

Figure 2.8. Drift Chamber Cell Structure.

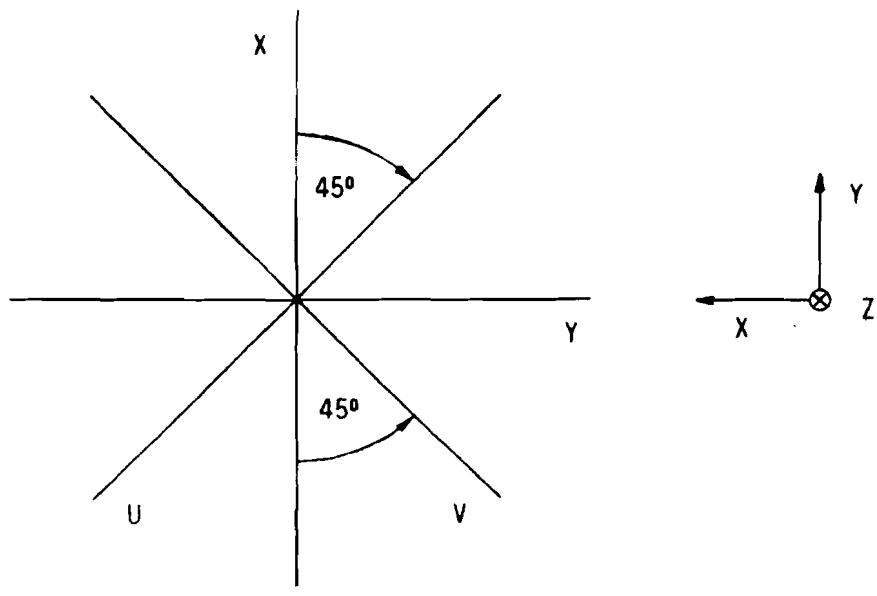

Figure 2.9. Relative Orientation of Drift Chamber Sense Wire Planes.

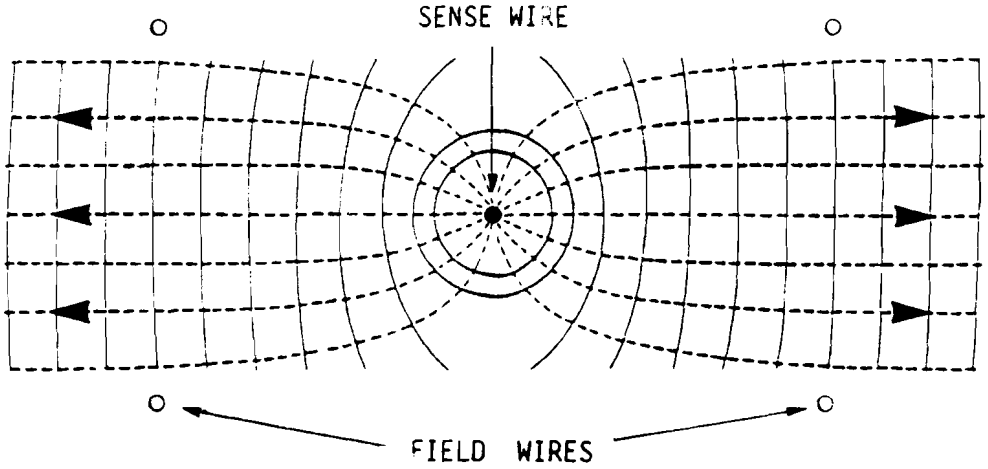

Figure 2.10. Diagram of Drift Chamber Field.

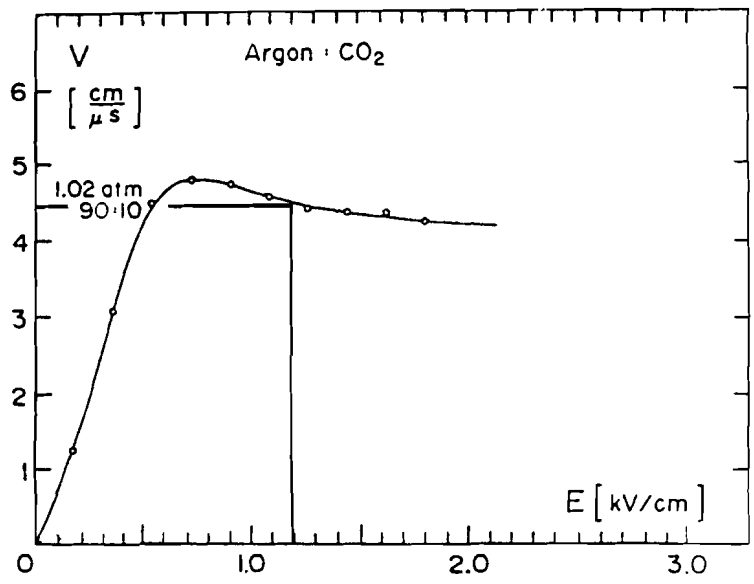

Figure 2.11. Plot of Drift Velocity vs Electric Field for Argon/CO_2 90/10 [12].

Each chamber station was serviced by its own CAMAC crate that contained a control module which generated a 20 MH_z clock [13]. The clock was used to digitize the time between the arrival of an amplified signal from a sense wire (RUN) and a common STOP signal generated by an event trigger. Receipt of a RUN pulse reset the time digitizers to zero. The incoming pulse was stretched to 50 ns which resulted in a 100 ns dead time between input pulses which helped prevent signals from late arrivals or δ-rays produced at the sense wire. The time between a RUN/reset signal and the first low-high clock transition is stretched 16:1 and digitized in each channel (1 channel/sense wire). The time between the first low-high transition and the STOP signal is digitized by counting clock transitions and the time from STOP to the next low-high clock transition is stretched 160:1 and digitized at 40 MH_z and subtracted from all channels in that crate.

Each drift chamber wire was aligned relative to the proportional chambers using the hit information from the calibration muons passing through the spectrometer. The drift time was converted to a hit coordinate by fitting to equations of the form

$$x1 = x_0 - v_1 * (t_0 - t)$$

$$x2 = x_0 + v_2 * (t_0 - t)$$

where

x_0 = wire location
t_0 = overall delay time
v_1 = drift velocity on one side of wire
v_2 = drift velocity on other side of wire
t = digitized drift time.

Alignment constants were also obtained for the non-linear regions of each cell near the sense wire and at the cell edges. The resolution and efficiency of each combined primed and unprimed plane, given in Table 2.6, were determined using calibration muons and K^0_S/Λ data events.

The performance and efficiency of the drift chambers was frequently monitored during the course of the experiment. Low efficiency was an indication of several possible problems. The most common problem was contamination of the gas due to small leaks in the chambers. If the efficiency of a chamber reached an unacceptable value it was flushed at high pressure with good gas. Other problems included oscillation of the gas gain circuitry, dead channels caused by shorting of the inductive couplers between the sense wire outputs and the digitizers, corroded contacts on the amplifier cards and noise pickup between amplifiers.

Table 2.6. Drift Chamber Efficiencies and Resolutions.

Plane	Efficiency	Resolution
1X,X'	0.55	512μ
1Y,Y'	0.82	523μ
1U,U'	0.83	539μ
1V,V'	0.71	573μ
2X,X'	0.60	528μ
2Y,Y'	0.67	482μ
2U,U'	0.77	494μ
2V,V'	0.61	505μ
3X,X'	0.52	543μ
3Y,Y'	0.69	474μ
3U,U'	0.79	544μ
3V,V'	0.62	537μ
4X,X'	0.55	566μ
4Y,Y'	0.59	500μ
4U,U'	0.67	527μ
4V,V'	0.53	604μ

2.6 Trigger

During the 1 second beam spill with 10^6 particles incident on the hydrogen target there were approximately 60,000 interactions of various types. The "dead" time of the experiment, the time required to record an event and reset the electronics, allowed the writing of approximately 50 data events per 1 second spill onto magnetic tape. Therefore it was clearly necessary to preselect events in an efficient and unbiased manner in order to enhance the number of potential neutral V's written onto tape. A two-stage trigger was used for this purpose. The first stage or Pre-Trigger indicated the existence of a beam particle incident on the target and a charged particle outside of the beam region in the forward spectrometer. The second stage was a TTL Trigger Processor that used the proportional chamber hit multiplicity to determine if the data should be written onto tape.

2.6.1 Pre-Trigger

The elements of the Pre-Trigger are shown in Figure 2.12. A beam particle was defined by the correct Cherenkov signal in coincidence with three scintillation counters B_1, B_2, B_3 and anti-coincidence with the "H" or halo counter. When running in the negative beam configuration the "correct" Cherenkov signal was either K^- or $\bar{p}$ and for the positive beam proton only. All of the above combined constituted a ϕ or "straight-through" trigger,

$$\phi = \text{Cherenkov} \cdot B_1 \cdot B_2 \cdot B_3 \cdot \bar{H} \ .$$

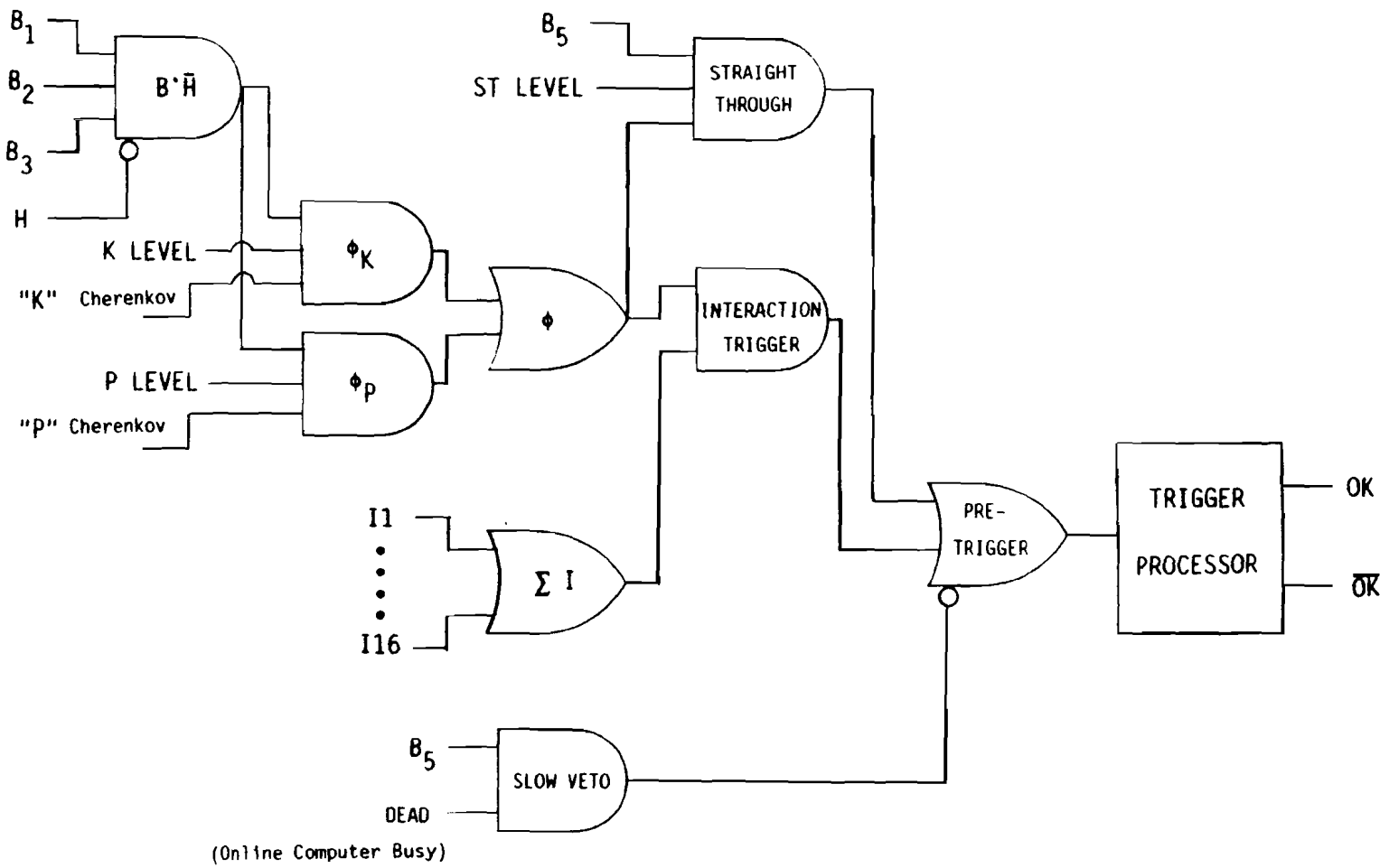

Figure 2.12. Pre-Trigger Logic Diagram.

This trigger was used by itself to select events for alignment of the beam and forward spectrometers with each other and was also incorporated in the total event trigger.

Charged particles not in the region of the beam, presumably associated with interactions in the target, were detected by an array of scintillation counters. This I-counter hodoscope had a 125 × 85 mm hole which allowed the noninteracting beam particles to pass through without triggering the experiment. The fields of the sweeping and analyzing magnet were periodically reversed which required the hole to be switched from left to right. This was done by enabling one of two pairs of horizontal counters in the array (Figure 2.13).

The logical sum of the 16 I-counters (ΣI) ANDED with ϕ defined an interaction trigger. Diffractive events were vetoed with a scintillation counter, labeled B_5, placed just upstream of the first proportional chamber station. The logical AND of ϕ, ΣI and $\bar{B}_5$ defined the Fast or Pre-Trigger:

$$\text{Pre-Trigger} = \phi \cdot \Sigma I \cdot \bar{B}_5 \ .$$

A Pre-Trigger initiated scanning of the proportional chamber data which was used by the Trigger Processor for the second level of decision making.

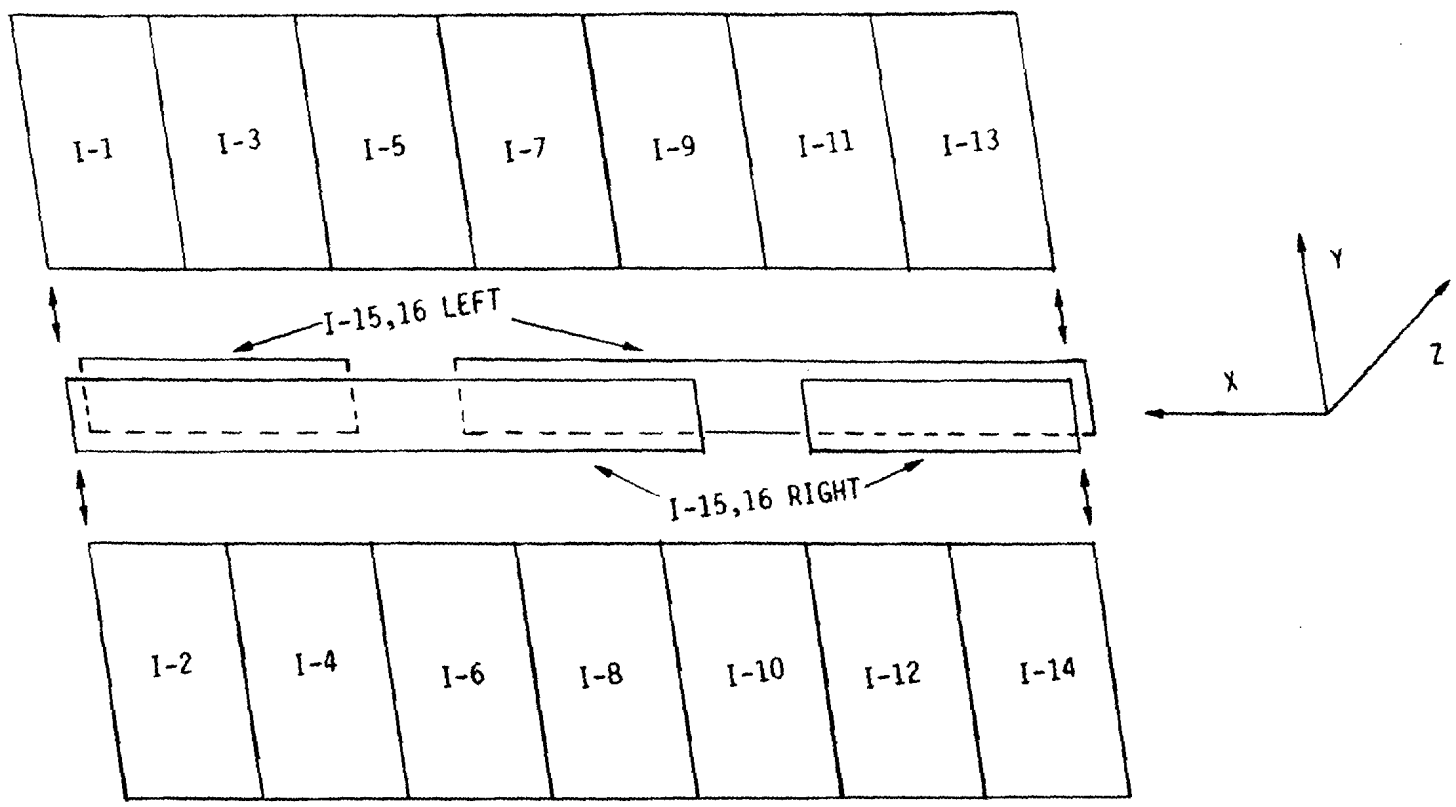

Figure 2.13. Interaction Counter Hodoscope.

2.6.2 Trigger Processor

The inclusive Λ cross-section is a small fraction of the total cross section and thus it is convenient and in fact sometimes necessary to reduce the amount of data actually written onto tape while enhancing the number of useful events per tape.

In our experiment this was accomplished using a simple on-line Trigger Processor. Based on the hit multiplicity in specified regions of the 8 PWC planes the processor issued a signal that would either initiate the data acquisition process or reset the experiment to be ready for another trigger. The presence of an allowed hit pattern indicated the existence of at least two tracks in the spectrometer. Details of the Trigger Processor and its function are given below.

Description

The layout of the processor is shown schematically in Figure 2.14. A Pre-Trigger indicating an interaction in the target initiated the serial scanning of data of the 8 PWC planes at 10 MH_z. The data and synchronous clock were routed first to circuits which regenerated the clock and data signals as well as allowing the overall delay and phasing to be adjusted. The clock and data from each PWC plane were then routed through a digital discriminator whose function was to count hits (singles or clusters of adjacent hits) within a specified region of the chamber. The windows were determined by two 10-bit counters each of which defined an edge of a window. The counter inputs were set by the on-line computer via CAMAC and were checked every spill.

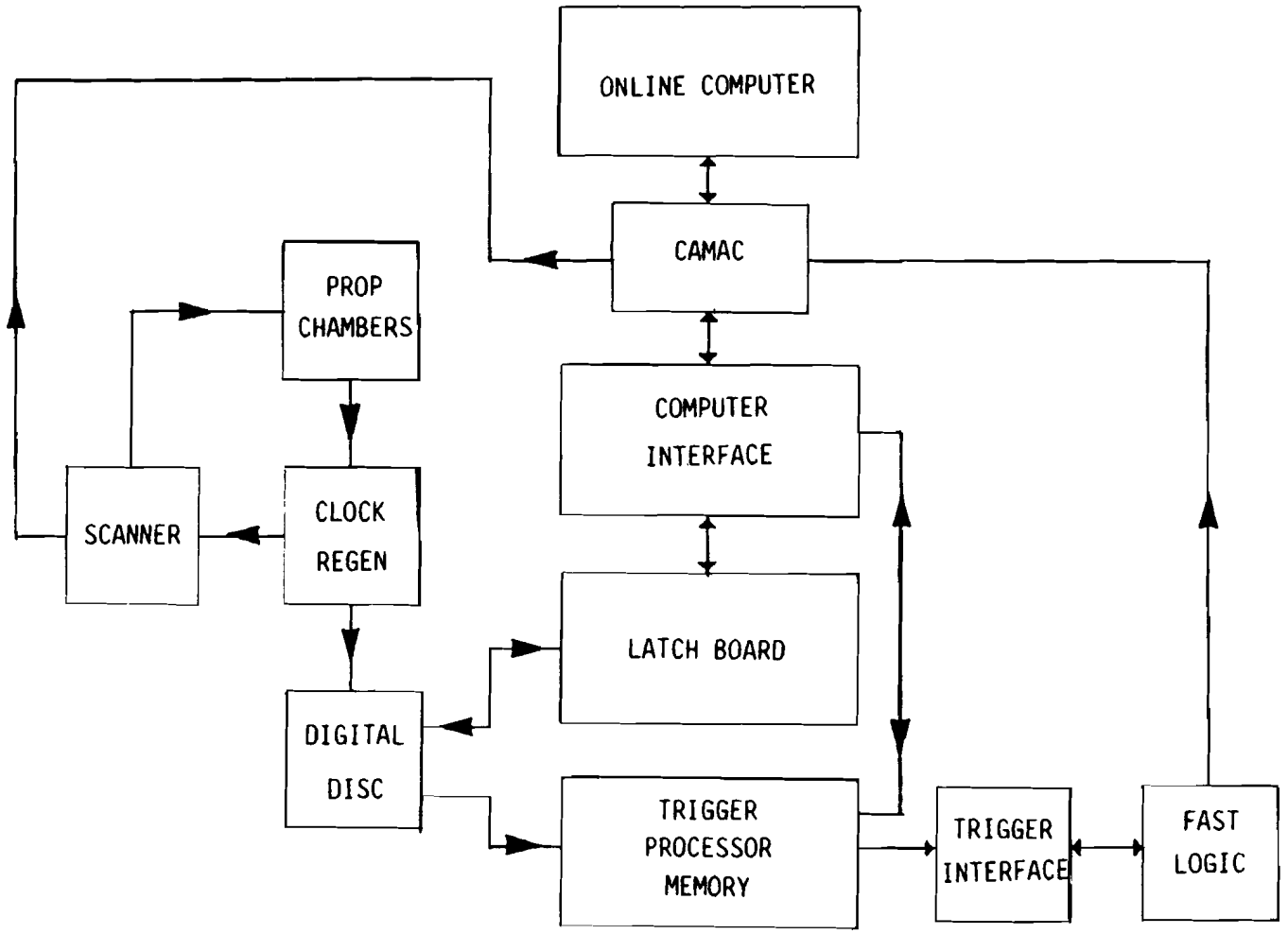

Figure 2.14. Trigger Processor Diagram.

The hits/clusters were encoded into 2 bits that with the 8 planes served as a 16 bit address for a 64K look-up memory programmed with allowable patterns of hits in the 8 chambers. The memory was programmed and checked by the on-line computer. All communication with the processor was done through the Computer Interface. It allowed the computer to perform the multiple functions of reading or writing into the memory, setting or checking the windows, and testing the processor. After the scanning of the PWC's was finished the memory was addressed and the logic level determined whether the experiment should be reset and made ready for another Pre-Trigger or whether the data for that event should be written onto disk. The time required for this decision was short compared to the 100 μs scan time for the proportional chambers.

Operation

The window widths and positions were determined by a Monte Carlo of inclusive Λ production with the aim of eliminating triggers due to particles not completely removed by the sweeper magnet upstream as well as tuning the acceptance to favor neutral V's.

Any group of adjacent hits in a chamber was counted as a single hit. Due to the existence of spurious hits in the chambers the optimal hit pattern was all permutations of two or more hits per plane while allowing one plane to have just one hit. The average PWC efficiency was 96%. If each chamber were required to have at least two hits the trigger efficiency would be only 52%. Relaxing this requirement by one hit gives an efficiency of 87%.

Performance

The performance of the trigger processor was monitored by periodically taking a data tape for which all Pre-Triggers were written onto disk ignoring the output of the processor. Without the trigger processor in the trigger we obtained approximately 0.02 neutral V's (K^0's, Λ's, and $\bar{\Lambda}$'s) per trigger, with the processor the ratio went to 0.08 giving us a factor of four in trigger efficiency while contributing negligibly to the experiment dead time. See Table 2.7 for a summary of trigger rates.

Table 2.7. Average Trigger Rates per Spill.

Definition	Protons	$K^-/\bar{p}$
Secondary Beam	2.8×10^5	3.3×10^5
$B_1 \cdot B_2 \cdot B_3 \cdot \bar{H}$	2.5×10^4	1.3×10^5
ϕ	8.2×10^3	4.5×10^3
Pre-Trigger	638	325
OK	75	45

2.6.3. Data Acquisition

The final and one of the most important tasks was to retrieve and store the data generated by the apparatus. Whenever the two-stage trigger was satisfied the experiment was disabled. The small memory available necessitated writing the information for that event onto disk. This had to be done as efficiently and quickly as possible in order to minimize the "dead time" i.e., the amount of time needed to transfer the data from the electronics modules to intermediate storage and reset the experiment. At the end of the one second beam spill the information on disk was transferred to tape. With the time remaining of the 10 seconds between beam spills the data on disk was examined by the on-line computer (Data General Corp. ECLIPSE S/200). During this time many diagnostic functions were performed which included testing the memory and window settings of the trigger processor. This activity continued until the beginning of the next spill when the experiment was enabled.

SECTION 3

ANALYSIS

The analysis process is broken down into several discreet steps. The first aspect is to decode the chamber information on the raw data tape and convert to useful units such as meters, seconds, etc. This information is then subjected to a pattern recognition algorithm which attempts to reconstruct all possible particle tracks (their momenta, slopes, and intercepts) in each event. These sets of tracks are then searched for prospective Λ's, $\bar{\Lambda}$'s and K^0_S's. At this stage the information is available to do the physics which includes, besides the actual polarization measurement, bias checks, acceptance corrections, etc. A necessary component of the final stage of the analysis is the generation of Monte Carlo events which simulate the environment in which the data were taken and allows corrections to be made for the effect of geometrical acceptance on the data events and to determine background contributions to the polarization.

3.1 Track Finding/Pattern Recognition

A set of pattern recognition and track finding subroutines is used to extract from the "hits" in the spectrometer system 3-dimensional space-tracks in as unbiased a manner as possible. It should be stressed that at this point in the analysis all possible tracks regardless of the kinematic configuration were reconstructed.

The general algorithm is outlined below.

1. Take all possible pairs of hits in the elevation view (Y-views) separated by at least one chamber station and search for tracks in a road of width given by the chamber resolution.

2. These tracks are then linked to the other views via the information from the X,Y,U and V chambers at each of the 4 stations in the spectrometer.

3. The confidence level of each track is checked and improvements to the fit are attempted by adding and/or throwing away hits on or near the track. The sharing of hits between tracks was not allowed unless the removal of a shared hit caused an otherwise good track to be lost.

4. The up- and downstream segments in the bend view (x-view) were required to meet at the center of the analysis magnet. Tracks were also required to have an intercept in the vicinity of the target. The slopes, intercepts, and momenta of the successful candidates were written onto tape for later use in the analysis.

3.2 Particle Reconstruction and Identification

The tracks found by the pattern recognition/track-finding algorithm were used to reconstruct possible Λ's, $\bar{\Lambda}$'s and K^0_S's for polarization analysis. A series of topological cuts were made to determine the final sample of candidates. Mass cuts were made only after a candidate passed all geometrical cuts. The data reduction sequence is described below.

Beam Cuts

This series of cuts generated a set of events of known particle type and well defined phase space parameters which were important in accurately determining the production plane.

1. Events with no beam track or more than one beam track were rejected.

2. Each event was required to have an x and y track with at least 3 hits.

3. In the x-view (bend view) the furthest upstream and downstream beam chambers were required to have a hit.

4. The measured beam momentum, P, was required to be greater than 160 GeV/c and less than 200 GeV/c.

5. The Cherenkov counter was used to determine the incident particle type.

Neutral V Cuts

These cuts were used to test all possible pairs of tracks recorded in the forward spectrometer under the hypothesis of the decay of a neutral particle to two charged secondaries contained within the fiducial volume defined by the downstream end of the sweeping magnet and the most upstream chamber station.

1. An event was required to have at least one pair of nonparallel full space-tracks with a good χ^2 and opposite charge.

2. Cuts were made on the analysis magnet aperture (X_M, Y_M).

3. The two tracks of a potential neutral V were required to pass within a minimum distance of each other at the decay point (C_{Decay}).

4. The Z coordinate of the closest approach of the decay (Z_D) was required to be between the sweeping magnet and the first chamber station.

5. A cut was made on the distance of closest approach between the beam and the momentum vector of the neutral (C_{Prod}).

6. The Z of the closest approach of production (Z_p) was required to be from the target.

7. All combinations were traced back through the sweeping magnet and the z position of the intercept was calculated. The neutral V's from real decays were focussed inside the sweeping magnet while directly produced charged particles intercepted the target. Therefore a cut was made on the z intercept (Z_{Dir}) which helped eliminate directly produced oppositely charged pairs that could fake neutral decays.

Masses for the combinations that survive the above cuts are calculated under the hypothesis of Λ, $\bar{\Lambda}$ and K^0. Mass cuts then eliminate approximately 10% of the possible combinations that passed the geometrical cuts. Further cuts were made in an attempt to separate Λ's and $\bar{\Lambda}$'s from K^0_S's.

Separation Cuts

1. Any combination with a good mass that looked like it decayed in the sweeping magnet was rejected. This cut served to eliminate Λ's or $\bar{\Lambda}$'s with unacceptable errors in the precession (Section 3.4.1) due to the particle traversing an unknown field length. It also eliminated combinations that could fake other neutral V's due to the uncertain $p_\perp$ the decay products received in the sweeper.

2. A cut was made to reduce the overlap between K^0_S's and Λ's or $\bar{\Lambda}$'s by calculating the ratio of the energy of the positive particle and the negative particle assuming alternately $\pi^\pm$, p or $\bar{p}$. The ratio had a definite range of values depending on the identity of the neutral and in the cases where there was no overlap the ambiguity was resolved.

$$K^0: \quad 0.09 < \frac{E_{\pi^+}}{E_{\pi^-}} < 10.6$$

$$\Lambda: \quad 3.09 < \frac{E_p}{E_{\pi^-}} < 14.6$$

3. A cut on the $p_\perp$ of the decay is made to separate K^0_S's from Λ's and $\bar{\Lambda}$'s.

Additional cuts were made to eliminate regions of the apparatus where the acceptance was not well known, such as small cracks between the interaction counters and dead or inefficient regions of the drift and proportional chambers caused by beam loading and degradation.

Table 3.1 lists the losses in the data reduction sequence for the total data sample. The subset for each cut does not include events lost due to previous cuts in the sequence. Where appropriate the cuts are labeled with the symbols used in the preceding discussion.

In Figures 3.1-3.6 are shown some of the distributions used in the data reduction process described above. Superimposed on the data distributions (points with error bars) are the Monte Carlo generated distributions (unbroken lines). The distributions are with all cuts except the ones indicated for that distribution. Table 3.2 shows the final results after all cuts have been made.

Table 3.1 Data Reduction Losses.

Total Number of Events = 2,540,725

	Cut	Losses	Fraction Of Total
BEAM CUTS	Events w/o one beam track	266,766	0.105
	Events w/invalid Cherenkov	3,669	0.001
	Events w/invalid momentum	61,916	0.025
NEUTRAL V CUTS	Events w/less than two tracks	1,265,792	0.498
	(The 943,512 events w/two or more tracks contain 1,244,529 possible combinations)		-
	Combinations w/the same charge	476,855	0.383
	(This leaves 767,674 combinations w/opposite charge)		
	Analysis magnet cut ($-0.48 < X_M < 0.70$) ($-0.28 < Y_M < 0.25$)	28,404	0.037
	C_D ($0.0 < C_D < 0.01$)	434,159	0.565
	Z_D ($-0.226 < Z_D < -6.0$)	44,712	0.058
	C_p ($0.0 < C_p < 0.01$)	16,889	0.022
	Z_p ($-0.275 < Z_p < -0.25$)	80,606	0.105
	Z_{DIR} ($-0.31 < Z_{Dir} < -0.252$)	73,670	0.096

(Table 3.1 cont.)

	Cut	Losses	Fraction Of Total
MASS CUT	V candidates w/bad masses	28,302	0.037
	(Now make cuts on the 60,932 events that passed the neutral V and mass cuts.)		
CUTS ON GOOD MASS EVENTS	Bad $P_\perp$ of decay	3,690	0.061
	Bad E^+/E^-	385	0.006
	(This leaves 56,857 good Λ's, $\bar{\Lambda}$'s and K^0_S's.)		
ADDITIONAL CUTS	B_5 counter, cracks, and dead or inefficient regions	7,323	0.129
RARE CHANNELS	$\bar{p}p \rightarrow \Lambda, K^0_S$, $pp \rightarrow \bar{\Lambda}, K^0_S$ $K^-p \rightarrow \Lambda$, etc.	9,319	0.164
	(The final sample contains 40,215 useful events)		

Table 3.2. Final Data Set.

Channel	Number of Events
$pp \rightarrow \Lambda$	10,480
$\bar{p}p \rightarrow \bar{\Lambda}$	4,797
$K^- p \rightarrow \Lambda$	8,253
$K^- p \rightarrow K^0_S$	16,685

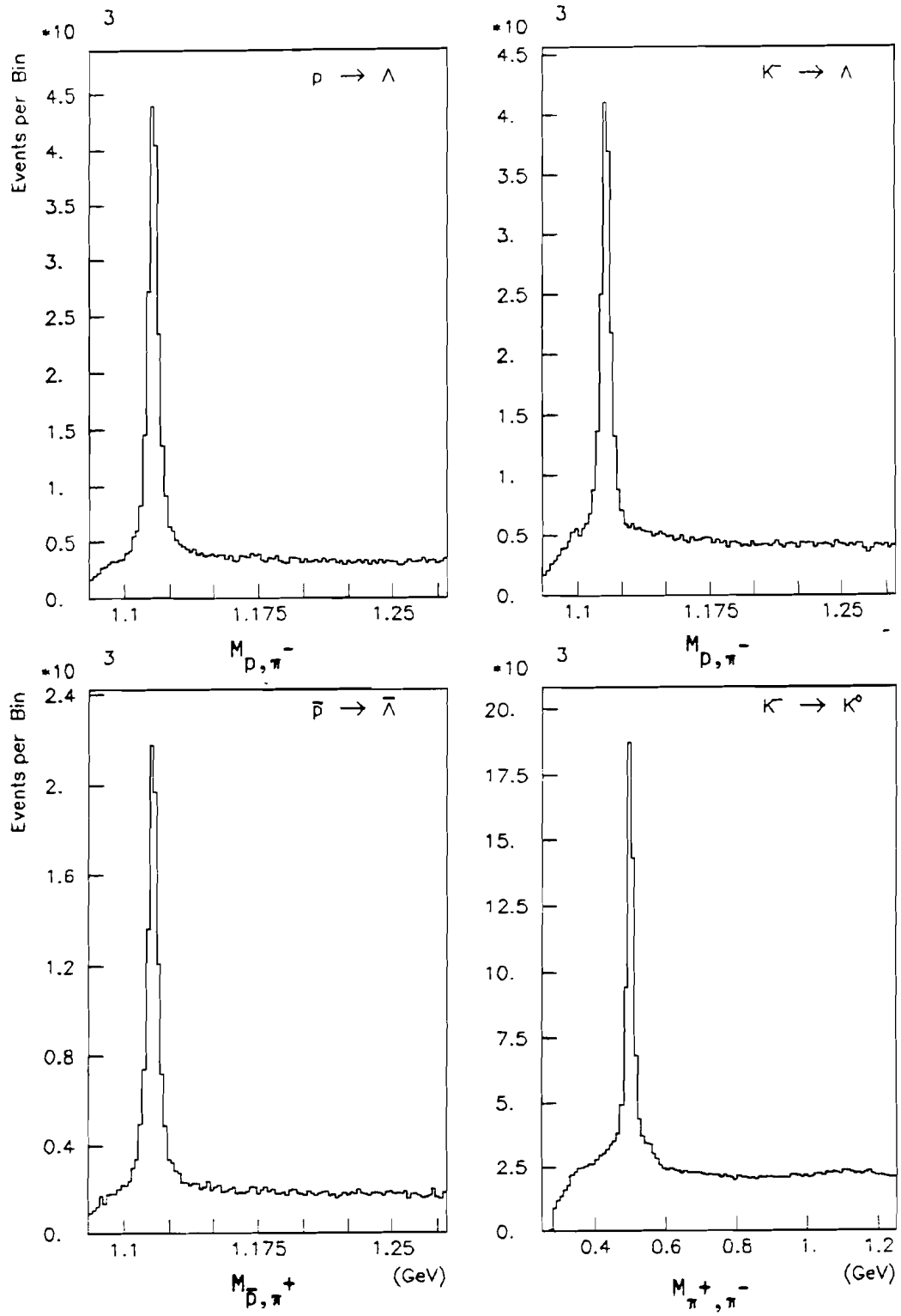

Figure 3.1. Raw Invariant Mass Distributions.
(Neutral V Cuts Imposed Only)

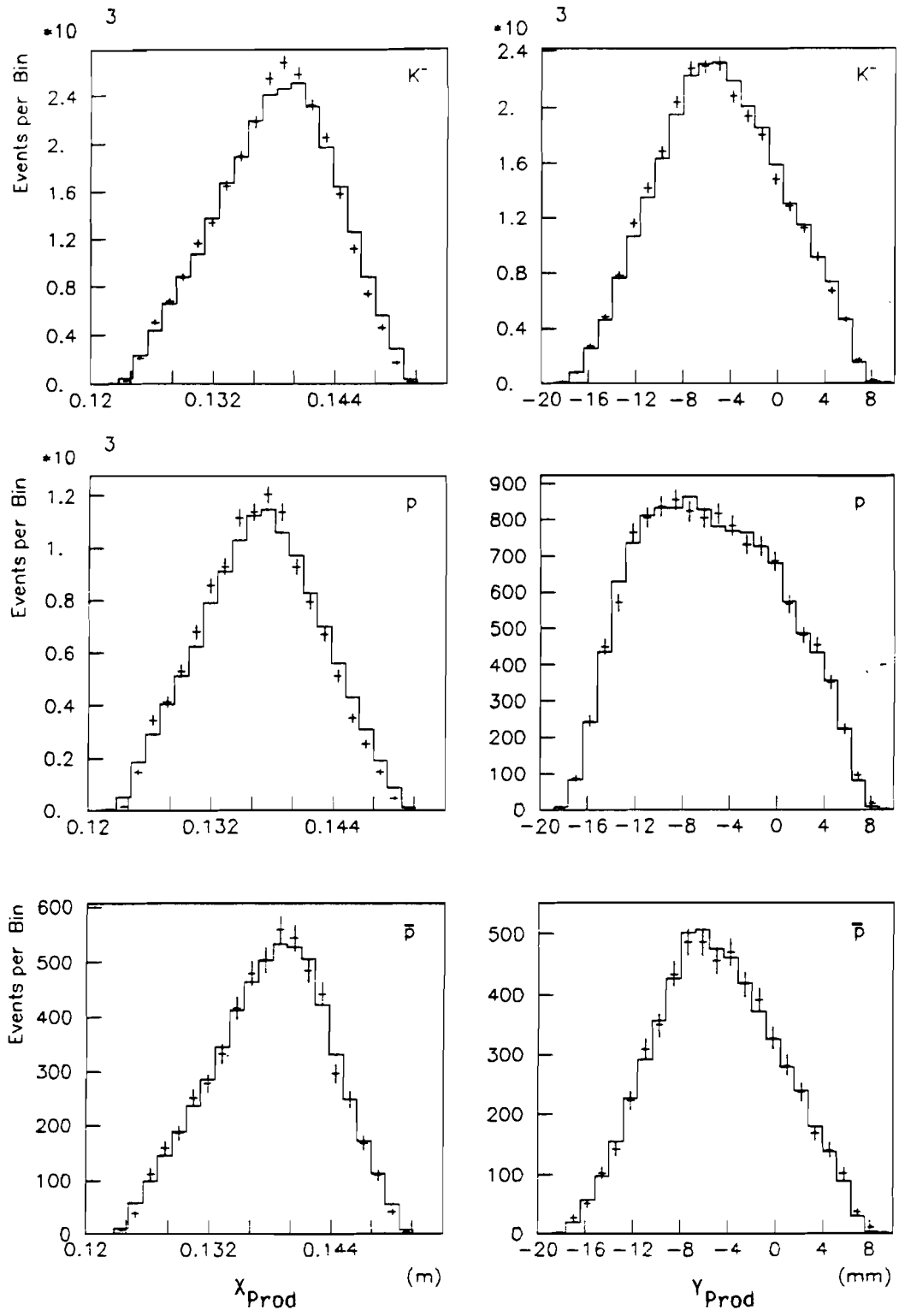

Figure 3.2. x and y Intercepts at Production Vertex. Points with error bars represent the data and unbroken lines represent Monte Carlo.

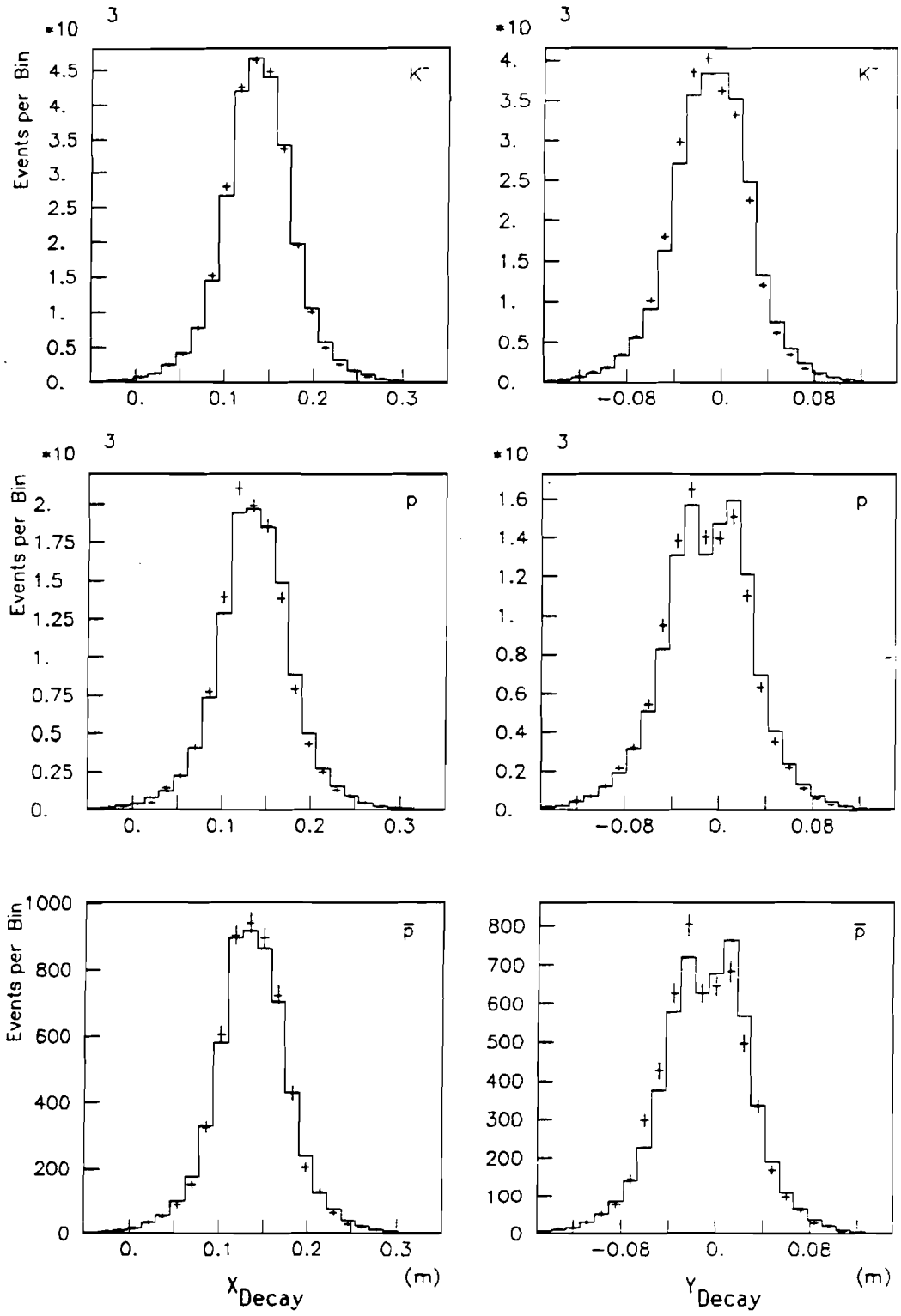

Figure 3.3. x and y Intercepts at Decay Vertex.
Points with error bars represent the data
and unbroken lines represent Monte Carlo.

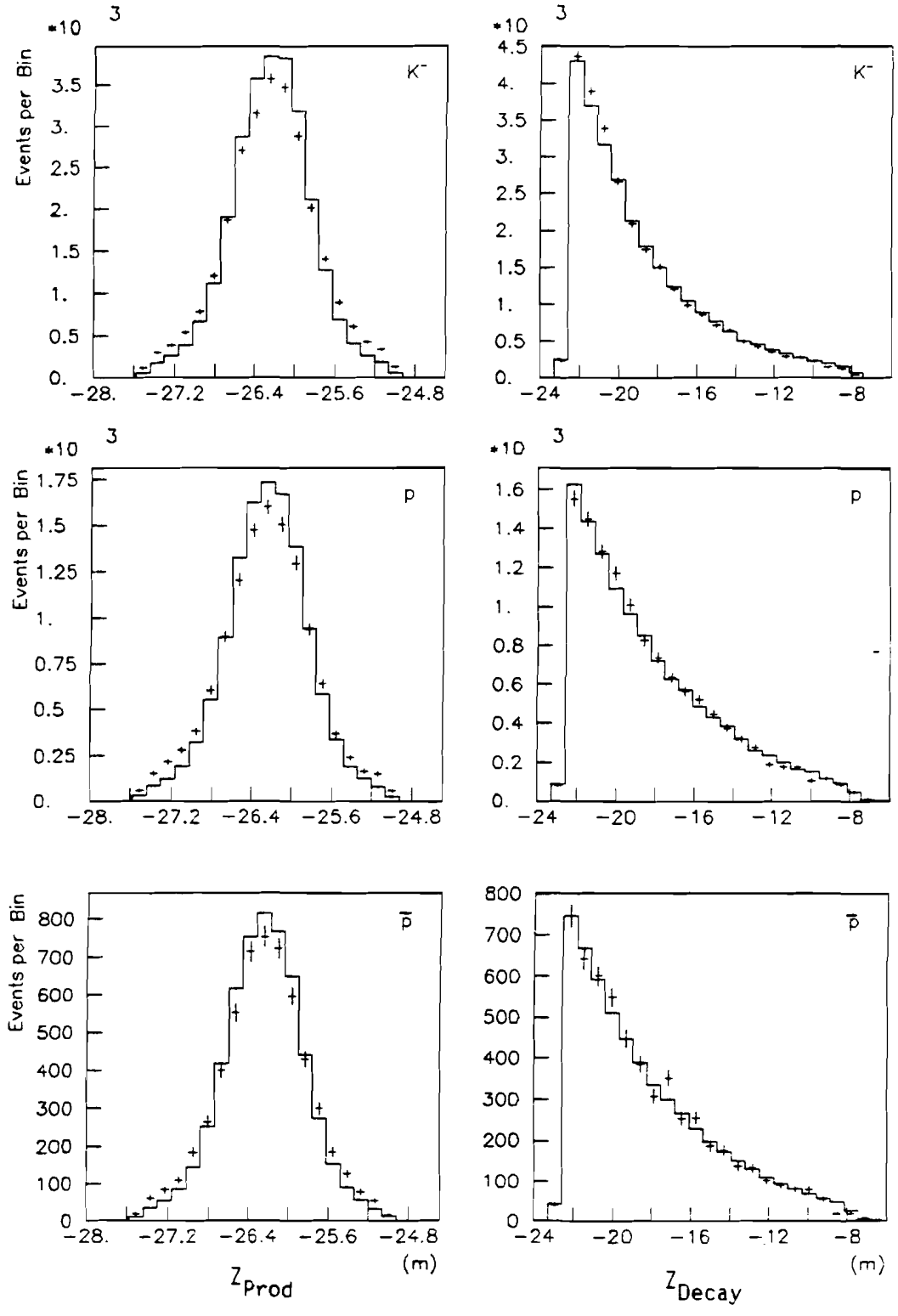

Figure 3.4. z of Production and Decay Verticies.
Points with error bars represent the data
and unbroken lines represent Monte Carlo.

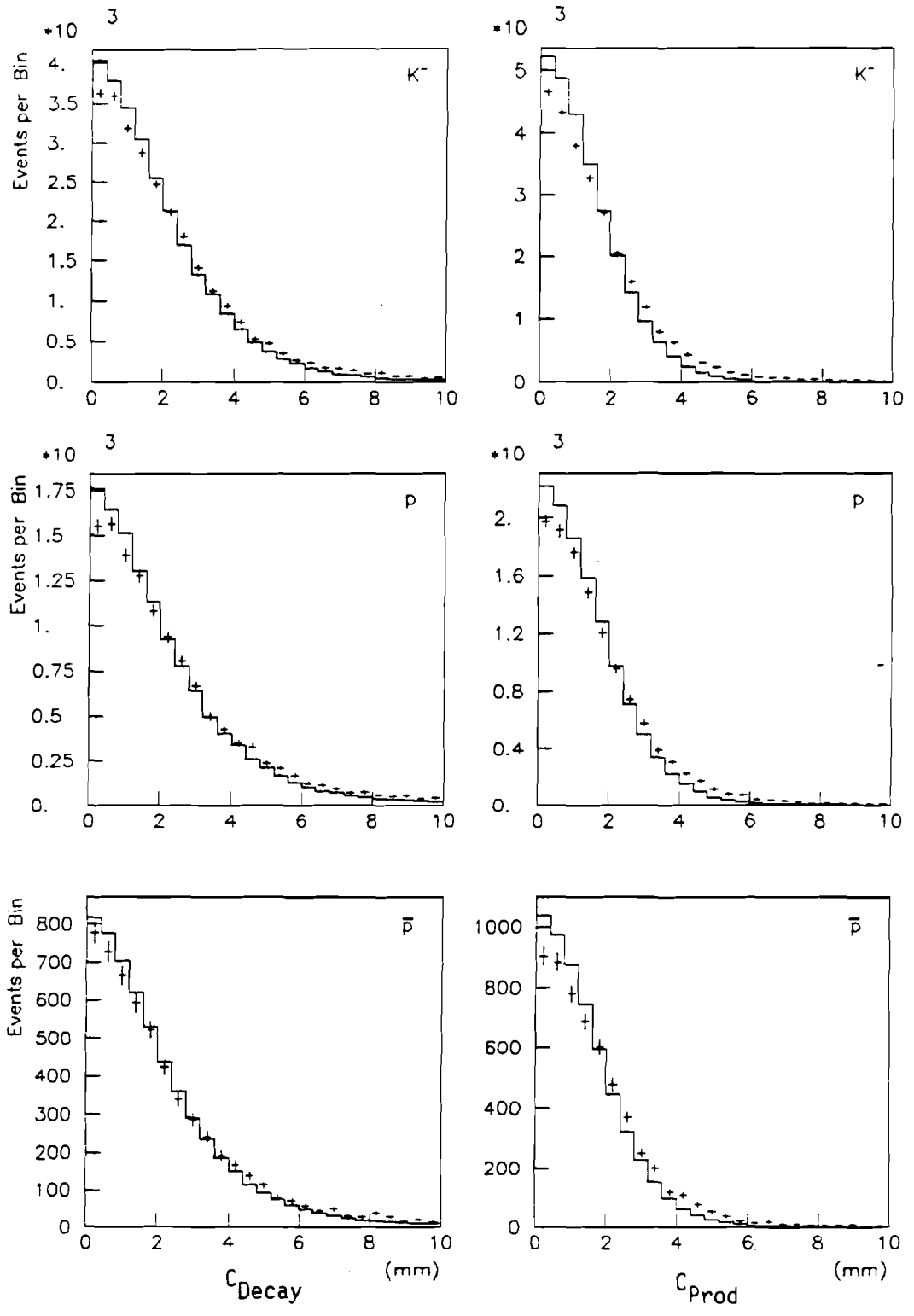

Figure 3.5. Distance of Closest Approach at Production and Decay. Points with error bars represent the data and unbroken lines represent Monte Carlo.

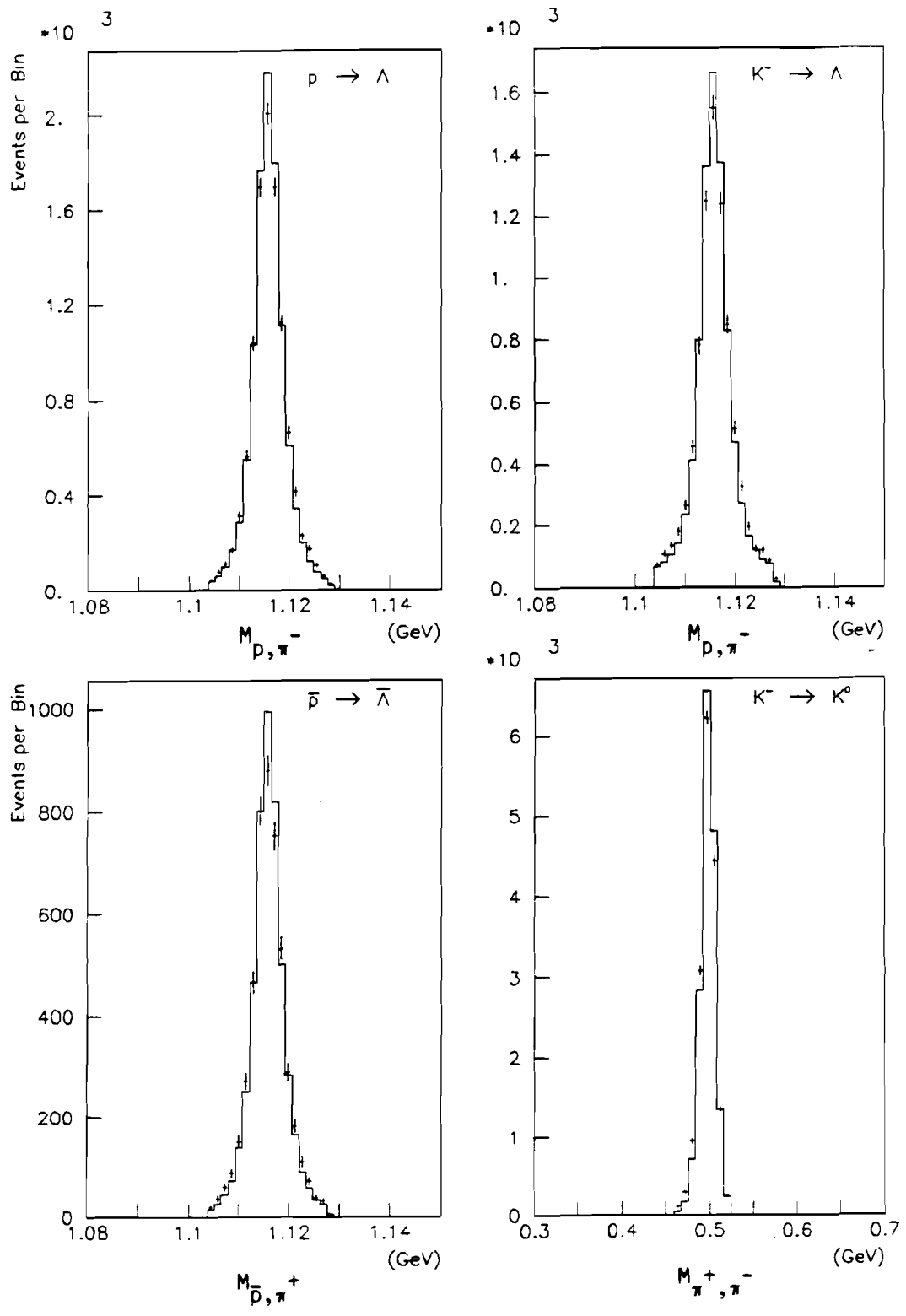

Figure 3.6. Invariant Mass Distributions After Cuts. Points with error bars represent the data and unbroken lines represent Monte Carlo.

3.3 Monte Carlo

The analysis of high energy physics experiments requires the use of a Monte Carlo program to study the effects of chamber and counter efficiencies and geometrical acceptances on the results of the experiment. A Monte Carlo is a computer program which generates a series of pseudo random numbers which are used to produce fake distributions of parameters used in the analysis of the data. In this experiment it was particularly important to detect and understand the possible biases which could result in the existence of a false polarization. The fake events generated by the Monte Carlo were used to determine the corrections that were applied to the real data events. Therefore it was necessary to generate Monte Carlo events in which the distributions of kinematic parameters matched the real data as closely as possible.

Beam

The beam momentum distribution of the data was divided into five equally populated bins. The z-location of the beam focus was found for each momentum bin in the x and y views. For each momentum bin the beam slope was plotted against the corresponding intercept at the z-focus for that view. The slope and intercept distributions at the different z foci were used as input for the Monte Carlo. A beam track was then generated by randomly selecting a momentum value from the data distribution and a slope and intercept from the appropriate two-dimensional slope-intercept distributions for that momentum. Using this method generated incident particle distributions that mimicked the data.

Fiducial cuts representing the beam counters B_1, B_2, B_3 and the halo counter H were made. Any track candidate failing these cuts was rejected and the process was repeated with a new set of variables. At this point the coordinates of a track passing the cuts were shifted to mimic multiple scattering.

The amount of the scattering was chosen from a scattering angle distribution calculated using a method derived by Goudsmit and Saunderson [14]. The location of the scatters in the experiment with respect to the center of the analysis magnet and the ratio L/L_R where L is the length and L_R is the radiation length is given in Table 3.3. The distributions for the scatterers in the experiment were parameterized by a function of Z, A and the thickness in grams of the scatterer. Three values of the parameter sufficiently represented the range of scatterers.

Cuts on the x and y slope and intercept at the target were imposed and hits from the surviving tracks were "quantized" to reflect the 1 mm wire spacing of the beam proportional chambers. Hit sharing between two adjacent wires was modeled for each plane.

Λ, $\bar{\Lambda}$, K^0 Generation

At this point in the program a fake Λ, $\bar{\Lambda}$, or K^0_S was produced. The relative ratios of Λ, $\bar{\Lambda}$, K^0_S were important in background studies and were determined from the data sample for each of the three incident particles, p, $\bar{p}$, and K^-. The z of the production point was determined by allowing for attenuation of the incident beam in hydrogen.

Table 3.3. Summary of Scatterers Found in This Experiment.

z (meters)	$L/L_R \times 100$	Element
-60.548	0.1685	Beam Chamber 1X
-60.353	0.1685	Beam Chamber 1Y
-60.350	0.1150	Air (35 cm)
-60.173	0.0177	He Tube Window
-54.085	0.2061	He Gas (1190 cm)
-48.244	0.0177	He Tube Window
-48.064	0.8760	B2 Counter
-47.999	0.1602	Air (48.73 cm)
-47.921	0.1685	Beam Chamber 2X
-47.705	0.1685	Beam Chamber 2Y
-45.806	1.2820	Air (389.84 cm)
-43.761	0.1685	Beam Chamber 3X
-43.614	0.1602	Air (48.73 cm)
-43.576	0.1685	Beam Chamber 3Y
-43.371	0.0177	He Tube Window
-37.563	0.2013	He Gas (1162 cm)
-31.753	0.0177	He Tube Window
-31.548	0.1280	Halo Counter
-31.526	0.1492	Air (45.4 cm)
-31.307	0.1685	Beam Chamber 4X
-31.112	0.1685	Beam Chamber 4Y
-29.483	1.1936	Air (362.3 cm)
-27.499	0.8760	B3 Counter
-27.440	0.1492	Air (45.4 cm)
-27.212	0.0442	Upstream Vac Window
-26.411	0.0442	Target Flask
-26.287	2.659	1/3 Target Hydrogen
-26.157	0.0442	Target Flask
-26.144	0.0442	Target Flask
-26.051	2.6590	1/3 Target Hydrogen
-25.814	2.6590	1/3 Target Hydrogen
-25.687	0.0442	Target Flask
-25.685	0.1957	Foam and Mylar
-24.310	0.9104	Air (277 cm)
-22.925	0.0885	Upst. Decay Pipe Wnd.
-8.315	0.8920	Dnst. Decay Pipe Wnd.
-8.074	0.1584	Air (48.2 cm)
-7.833	0.2190	PWC 1X
-7.689	0.2190	PWC 1Y
-6.872	0.5874	Drift Chamber 1XY
-6.691	0.5874	Drift Chamber 1UV
-6.517	0.0265	He Bag Window
-4.253	0.0785	Helium

(Table 3.3 cont.)

z (meters)	$L/L_R \times 100$	Element
-1.989	0.0265	He Bag Window
-1.846	0.5874	Drift Chamber 2UV
-1.664	0.5874	Drift Chamber 2XY
-1.415	0.2190	PWC 2Y
-1.215	0.2190	PWC 2X
-0.982	0.1530	Air (46.5 cm)
-0.750	0.0265	He Bag Window
0.000	0.0261	Helium Bag
0.75	0.0265	He Bag Window
1.26	0.3369	Air (102.5 cm)
1.775	0.2190	PWC 3X
1.924	0.2190	PWC 3Y
2.186	0.5874	Drift Chamber 3XY
2.370	0.5874	Drift Chamber 3UV
2.485	0.0265	He Bag Window
4.749	0.0785	Helium Bag
7.012	0.0265	He Bag Window
7.179	0.5874	Drift Chamber 4UV
7.361	0.5874	Drift Chamber 4XY
7.592	0.2190	PWC 4X
7.744	0.2190	PWC 4Y

The momentum p and transverse momentum P_T of the Λ or $\bar{\Lambda}$ and K^0_S were generated by using an acceptance corrected 2 dimensional p, P_T plot of the data for each combination of incident beam particle and outgoing neutral. The acceptance was determined by generating a flat two dimensional distribution in p and P_T. The input was obtained by dividing the data distribution by the acceptance. For each generated event a value of p and P_T was randomly selected from the input distributions. The outgoing particles' momentum vector was determined by a random polar angle in the incident particle coordinate system and then transformed to the experiment coordinate system (Figure 3.7).

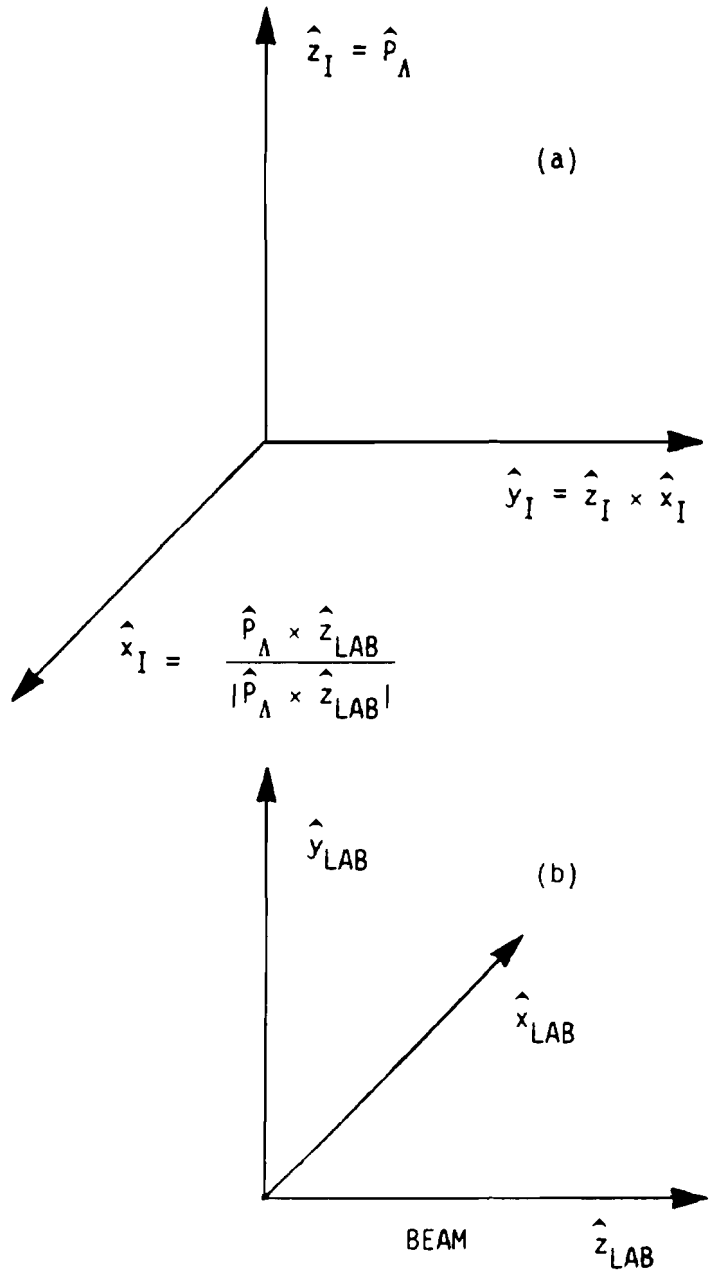

Figure 3.7. (a) Incident Particle Coordinate System.
(b) Experiment Coordinate System.

The decay point was selected according to the exponential decay distribution for that particle. The K^0_S decay distribution included the effects of K^0_L - K^0_S interference. For the case of decay in the sweeping magnet the decay products were traced through the magnet. The production plane normal of the Λ or $\bar{\Lambda}$ was precessed in the sweeper field.

The K^0_S decay was generated by selecting the π^+ momentum isotropically distributed in the K^0_S rest frame. The pion momentum vector for the Λ or $\bar{\Lambda}$ was distributed according to

$$1 - \alpha P \cos\theta$$

where θ is the angle between the pion momentum vector and the production plane normal. The decay product momenta were transformed to the incident particle frame and then to the experiment frame.

Forward Tracks

The decay products of the Λ, $\bar{\Lambda}$ or K^0_S were propagated through the forward spectrometer, the intercept at each chamber plane defining an unperturbed "hit." The decay $\pi \rightarrow \mu + \nu$ was allowed and the muon tracked through the spectrometer. Fiducial cuts at magnet apertures and the interaction counter hodoscope were made. All losses were accumulated and summarized at the end of the program.

The efficiency and resolution of each drift chamber wire and the efficiency of each proportional chamber plane were obtained from special muon runs distributed throughout the data taking. After multiple

scattering the hits in each drift chamber were spread by a Gaussian whose width was that of the resolution for that wire. The proportional chamber hits were "quantized" for the 2 mm wire spacing. A percentage of hits were removed to represent inefficiencies for that wire or plane. Hits were also removed to model the deadened wires in the beam region of the drift chambers and the support strings of the proportional chambers. Regions of low efficiency in the proportional chambers due to degradation by the beam were also modeled. The efficiencies were determined as a function of time. The number of data events used to calculate the efficiencies of a particular time period were used to normalize the number of Monte Carlo events generated with those specific efficiencies.

The raw or unperturbed parameters for each event were recorded and compared with the parameters of the reconstructed events to measure the resolution of parameters important to the analysis (Table 3.4). All surviving events were written onto a file in the same format as the data events and injected into the analysis sequence just prior to the pattern recognition and track finding programs. The Monte Carlo's ability to reproduce the experimental data was checked by comparing the distributions of kinematic variables between real and Monte Carlo generated events. Several of these comparisons are shown in Figures 3.8-3.15. The points with error bars are data and the unbroken lines are Monte Carlo generated distributions.

Table 3.4. Resolutions.

Beam Spectrometer		
x-slope	δx_s	25 μr
y-slope	δy_s	17 μr
Beam Momentum	$\delta p/p$	0.004
Forward Spectrometer		
Single Track Momentum	$\delta p/p$	0.021
x-Slope (single track)	δx_s	95 μr
y-Slope (single track)	δy_s	72 μr
Azimuthal Angle of π in Λ Rest Frame	$\delta\phi$	0.057 μr
$\cos\theta_z$ in Λ Rest Frame	$\delta\cos\theta$	0.028
z of Decay	δz_D	26.1 cm
Combined System		
Azimuthal Angle of Production Plane in Lab Frame	$\delta\eta$	0.023 rad
Lambda Mass	δM_Λ	3.5 MeV
K^0_S Mass	$\delta M_{K^0_S}$	8.5 MeV
Feynman X	δX_F	0.021
Transverse Momentum	$\delta P_T/P_T$	0.033
z of Production	δz_P	3 .8 cm

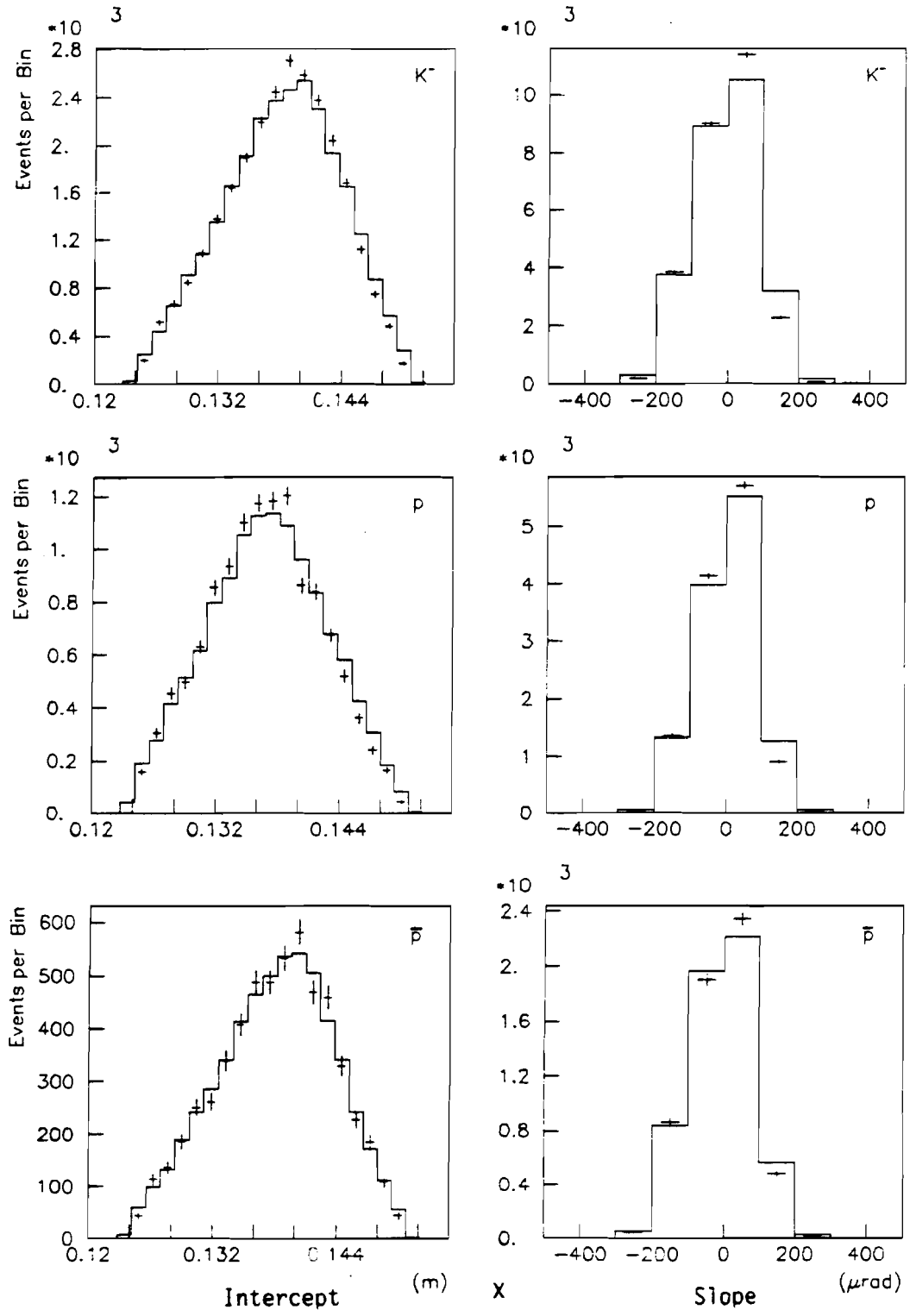

Figure 3.8. x Intercept of the Beam at the Target and x-Slope. Points with error bars represent the data and unbroken lines represent Monte Carlo.

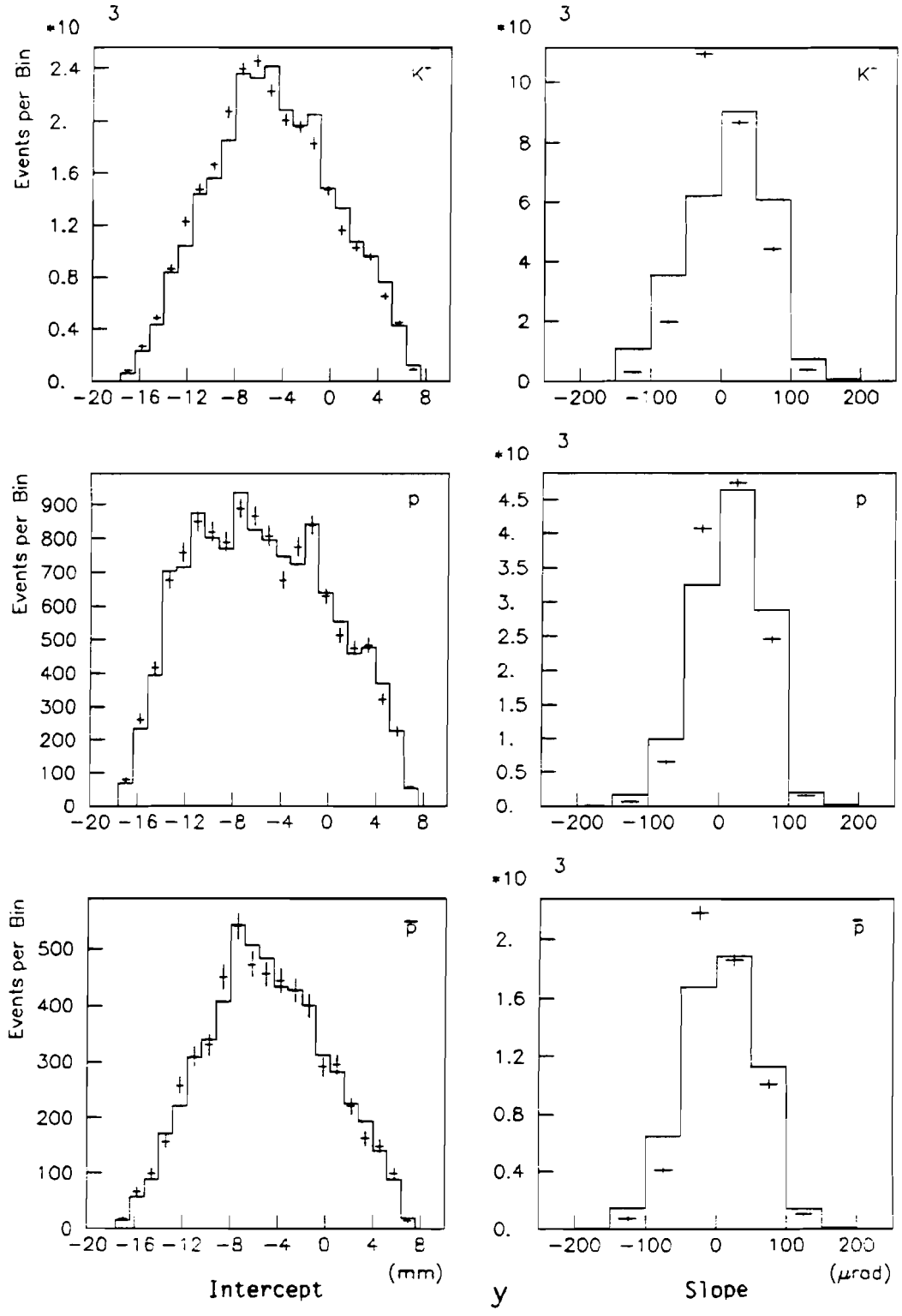

Figure 3.9. y Intercept of the Beam at the Target and y-Slope. Points with error bars represent the data and unbroken lines represent Monte Carlo.

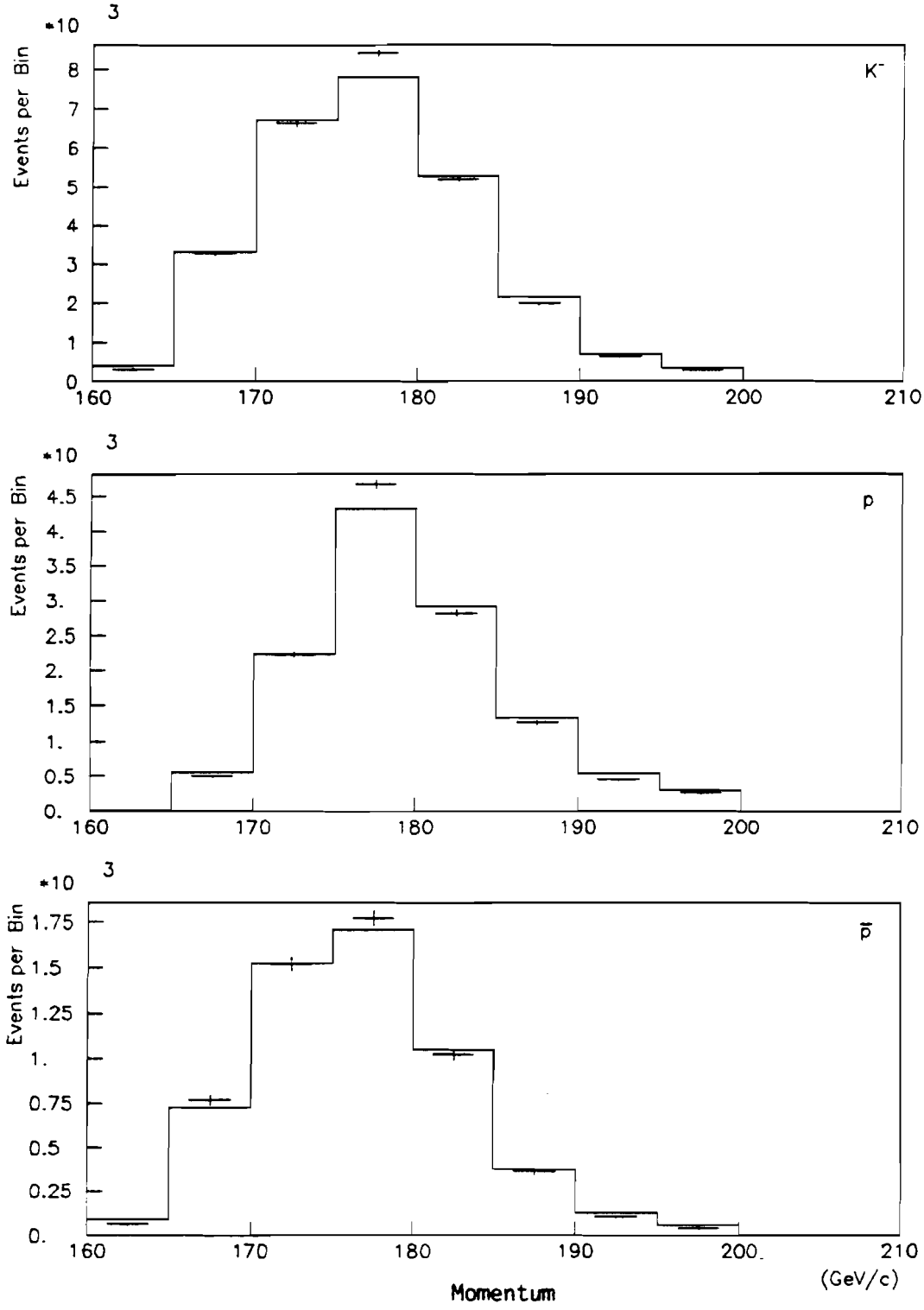

Figure 3.10. Beam Momentum Distribution.
Points with error bars represent the data
and unbroken lines represent Monte Carlo.

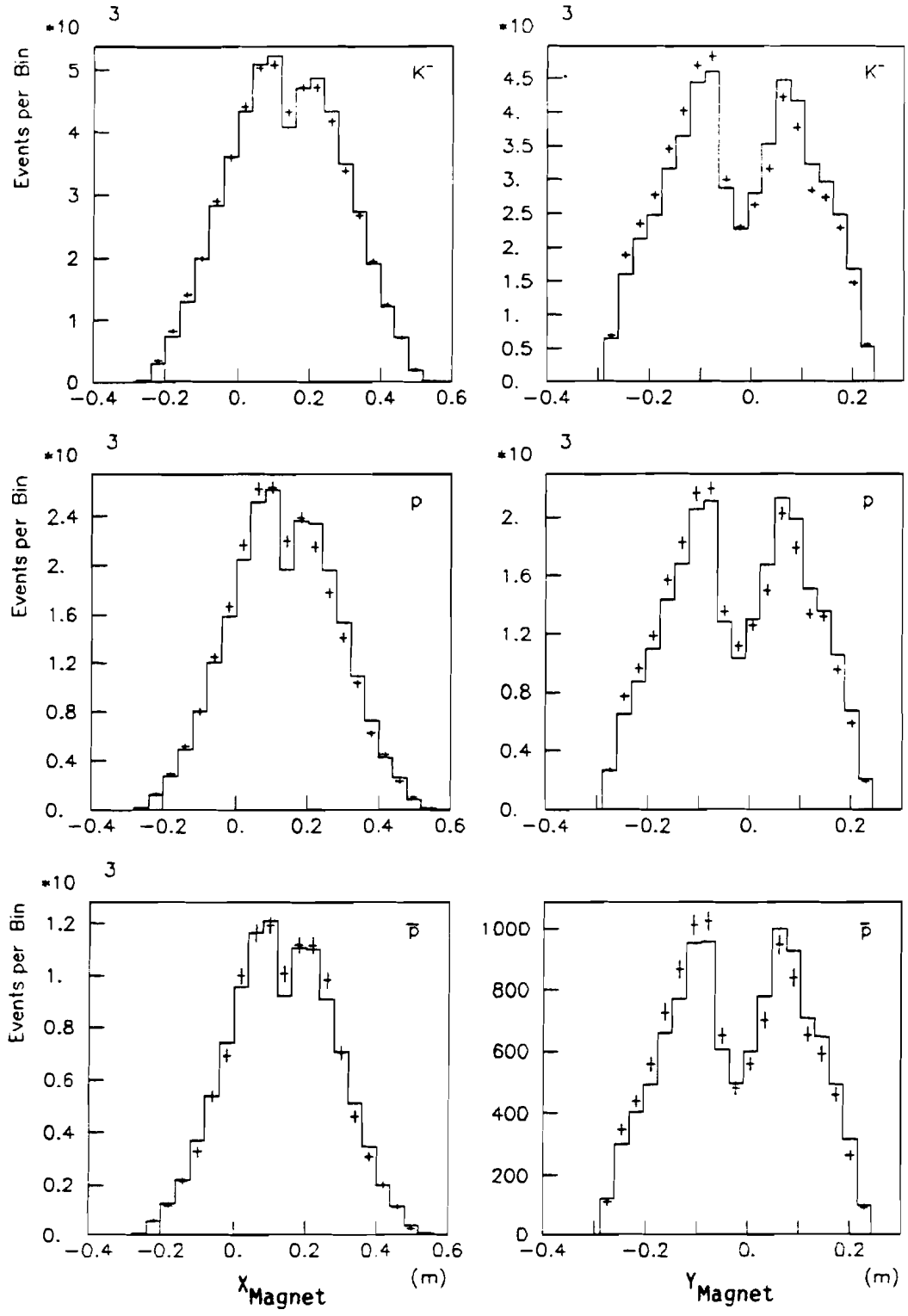

Figure 3.11. Track Intercepts of Decay Products at Analysis Magnet Center.
Points with error bars represent the data and unbroken lines represent Monte Carlo.

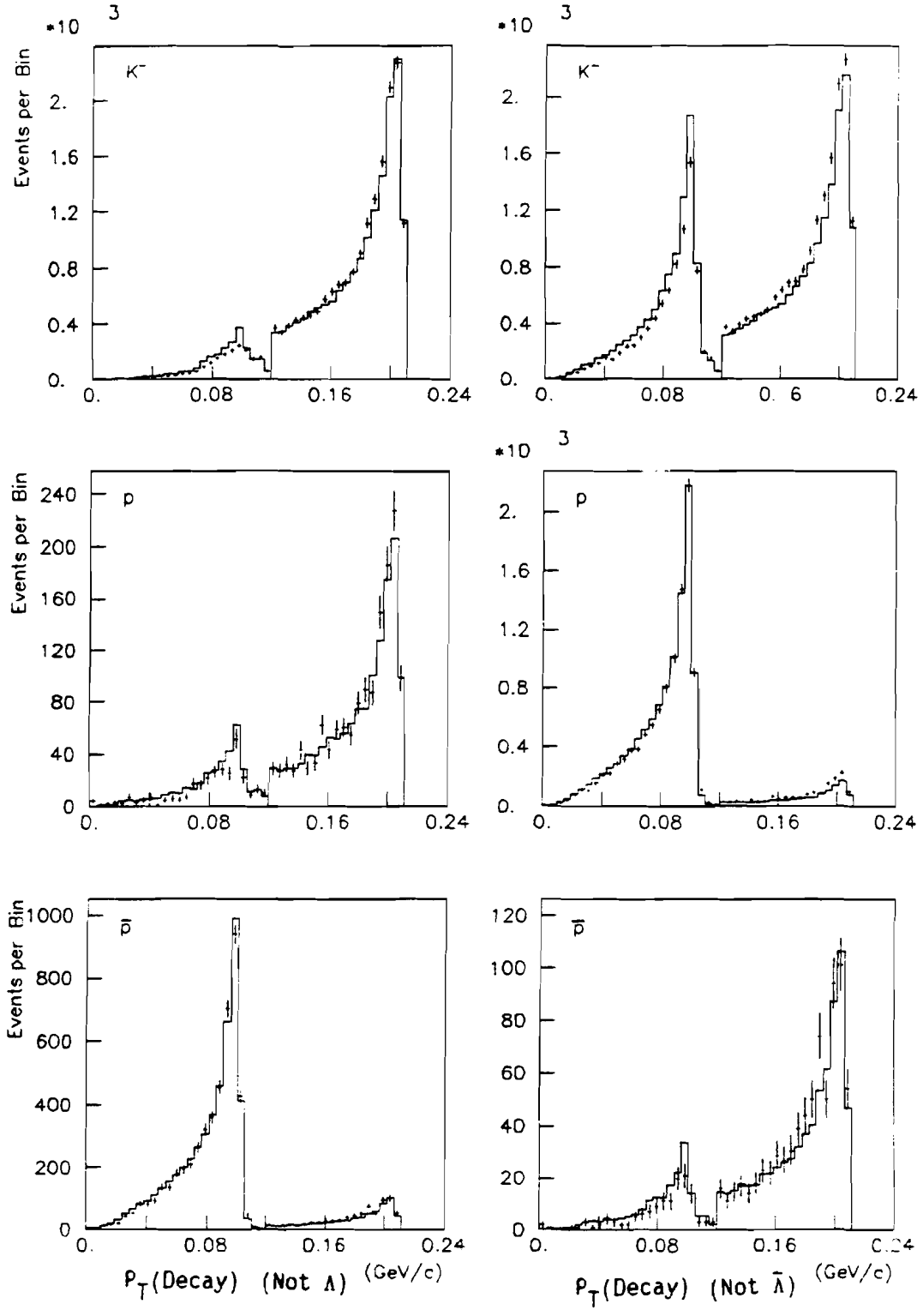

Figure 3.12. Distributions of Transverse Momentum of Decay. Points with error bars represent the data and unbroken lines represent Monte Carlo.

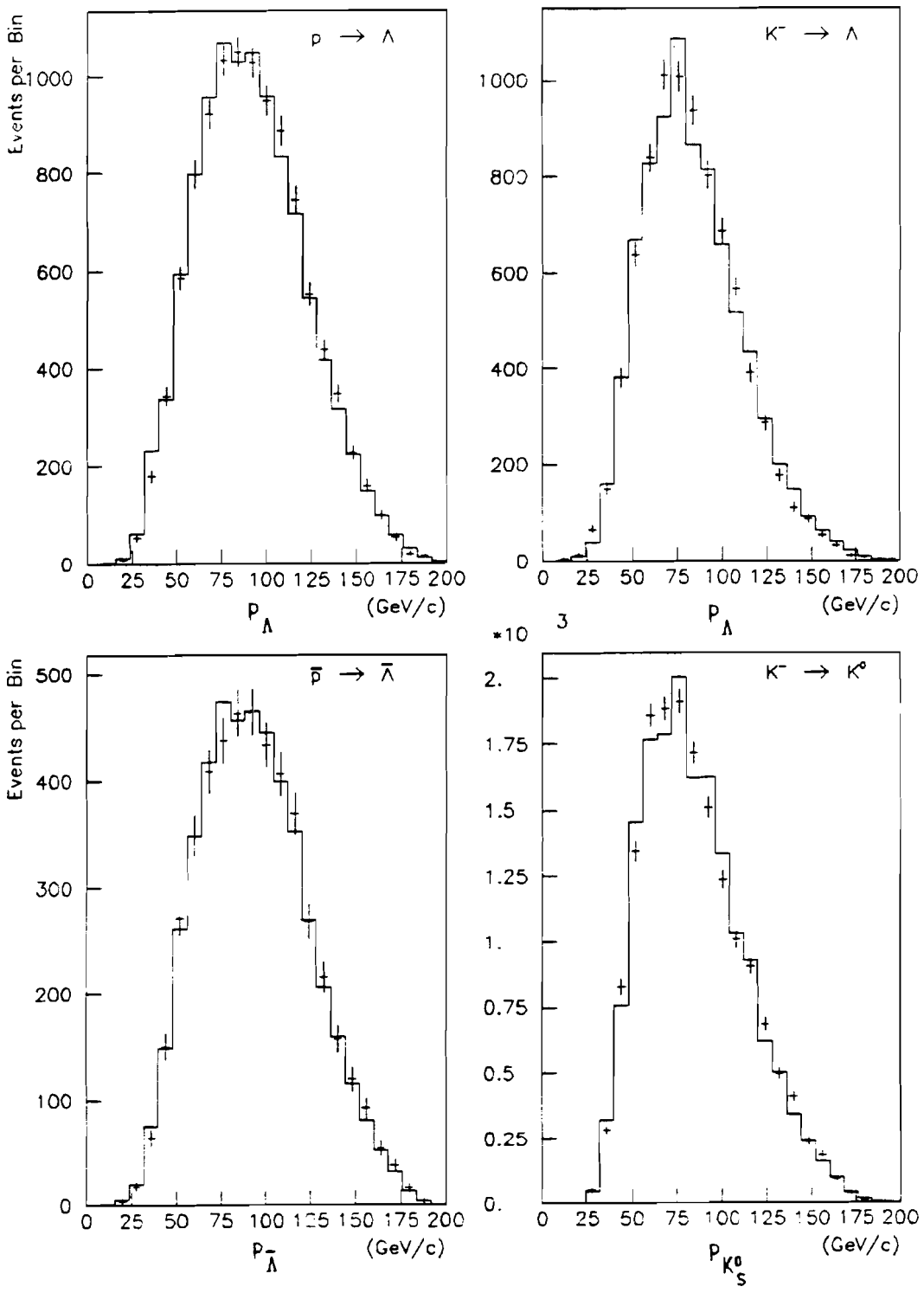

Figure 3.13. Momentum Distributions of $\Lambda, \bar{\Lambda}, K^0_S$.
Points with error bars represent the data
and unbroken lines represent Monte Carlo.

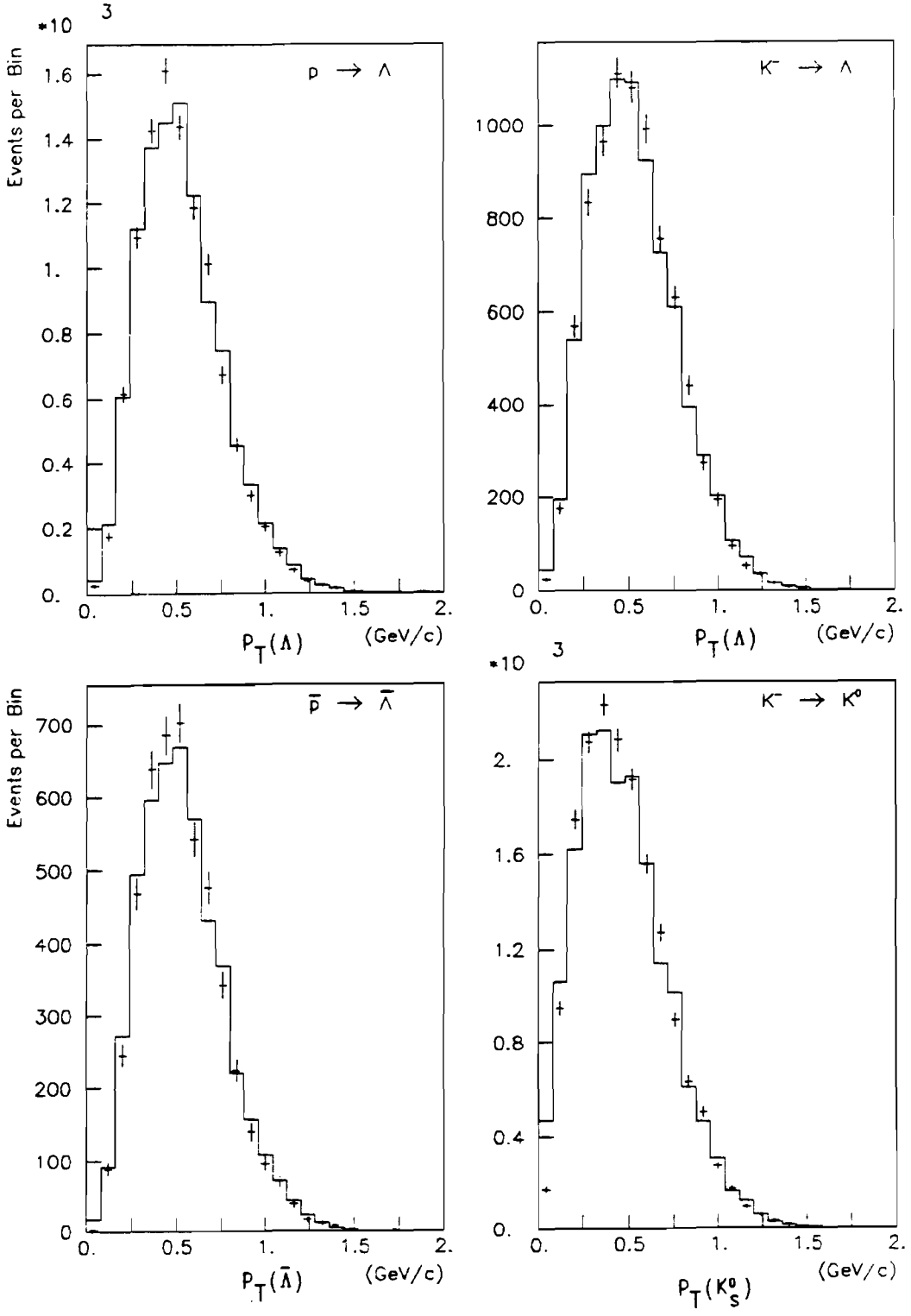

Figure 3.14. P_T Distributions of $\Lambda, \bar{\Lambda}, K^0_S$.
Points with error bars represent the data and unbroken lines represent Monte Carlo.

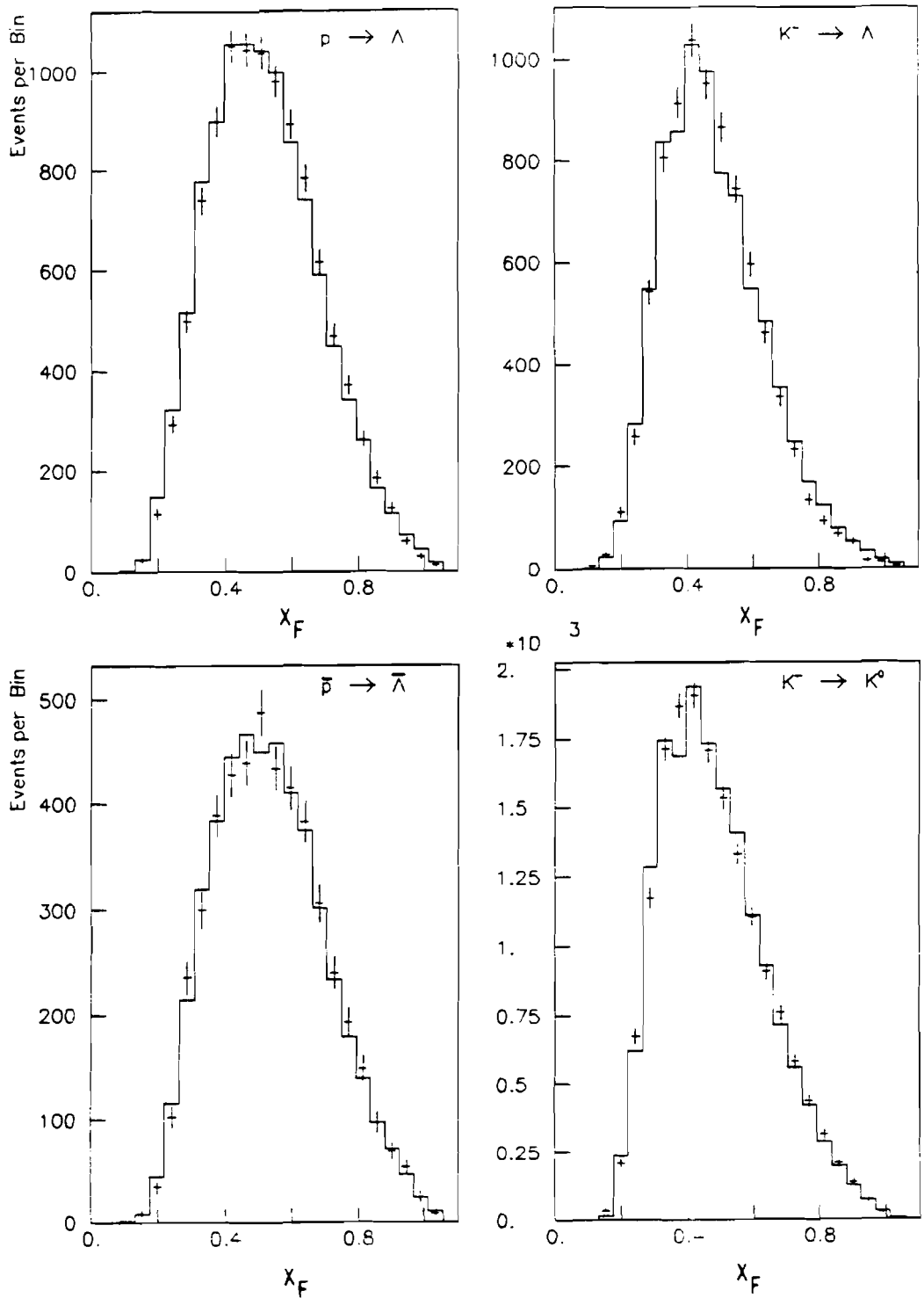

Figure 3.15. X_F Distributions of $\Lambda, \bar{\Lambda}, K^0_S$.
Points with error bars represent the data
and unbroken lines represent Monte Carlo.

3.4 Asymmetry Analysis

This section details the analysis procedure used to extract the parity-conserving asymmetry A_z and the parity-nonconserving asymmetries A_x, A_y from the decay distribution which is derived in Section 1.2.2.

$$\frac{dn}{d\Omega} = \frac{1}{4\pi}\left[1 + A_x \sin\theta\cos\phi + A_y \sin\theta\sin\phi + A_z\cos\theta\right]. \qquad (3.1)$$

3.4.1 Coordinate System

Described below are the steps in obtaining the coordinate system in which Equation 3.1 is valid. The laboratory coordinate system which is directly related to the apparatus is shown in Fig. 3.16, where Z_{lab} is approximately the beam direction, Y_{lab} measures vertically and X_{lab} is horizontal.

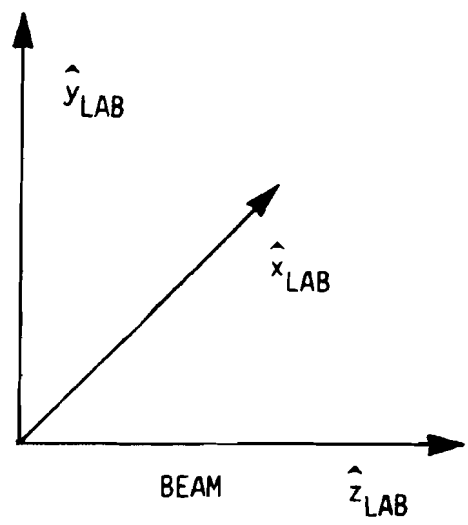

Fig. 3.16 Laboratory Coordinate System.

The laboratory frame is then rotated into the neutral "V" frame and boosted along the direction of the "V". The rest frame coordinate system (Figure 3.17) is defined by $\hat{z}_{RF} = \hat{n}$ (production plane normal), $\hat{x}_{RF} = \hat{z}_{RF} \times \hat{z}_{LAB}/|\hat{z}_{RF} \times \hat{z}_{LAB}|$ and $\hat{y}_{RF}$ is defined to form a right-handed coordinate system.

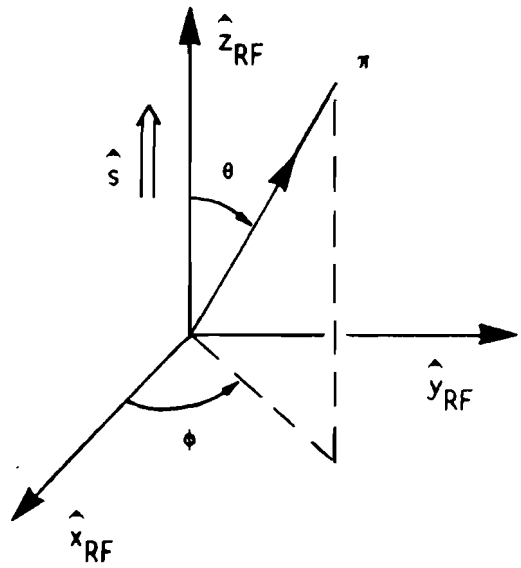

Fig. 3.17 Rest Frame Coordinate System.

An important feature of this experiment is that the production plane for each inclusive Λ or $\bar{\Lambda}$ produced is not fixed with respect to the laboratory coordinate system but the production plane normal can assume any orientation transverse to the beam direction. This has the effect of uniformly illuminating the apparatus which minimizes geometrical biases, in particular those that might be induced by the orientation of the fields of the sweeping and analysis magnets.

Some other polarization experiments have a fixed production plane and hence suffer from magnet dependent biases. These biases are usually cancelled by changing the incident beam angle such that the production plane changes sign. In this experiment the production plane orientation is different for each event.

Precession of Λ and $\bar{\Lambda}$ Spin

The Λ and $\bar{\Lambda}$ possess a non-zero magnetic moment. The interaction of the Λ or $\bar{\Lambda}$ with the field of the sweeping magnet as it emerges from the target causes the spin to precess around the direction of the magnetic field in the rest frame of the Λ or $\bar{\Lambda}$. The angle that the spin vector makes with the magnetic field remains constant and the angle that the projection of the Λ or $\bar{\Lambda}$ spin traces out in the plane normal to the magnetic field is called the precession angle, ϕ_p. The effect of the precession is to rotate the spin vector such that it is no longer collinear with the normal to the production plane. The angle between the pion and the normal to the production plane is found by precessing $\hat{z}_{RF}$ to match the configuration of the spin at the time of decay downstream of the sweeping magnet.

The precession angle ϕ_p in the Λ or $\bar{\Lambda}$ rest frame is given by

$$\phi_p = 0.0196 \int \bar{B} \cdot d\bar{\ell} \ (\text{kg-m})^{-1} \text{ radians}$$

and is proportional to the spin component perpendicular to the magnetic field direction. The $p_\perp$ of the sweeping magnet was 0.781 GeV/c which gives a maximum precession angle of 28 degrees. Figure 3.18 shows the precession of a Λ spin for the field in the $+\hat{y}$ direction. The precession for a $\bar{\Lambda}$ would be opposite to that of the Λ since $\bar{\mu}_{\bar{\Lambda}} = -\bar{\mu}_{\Lambda}$.

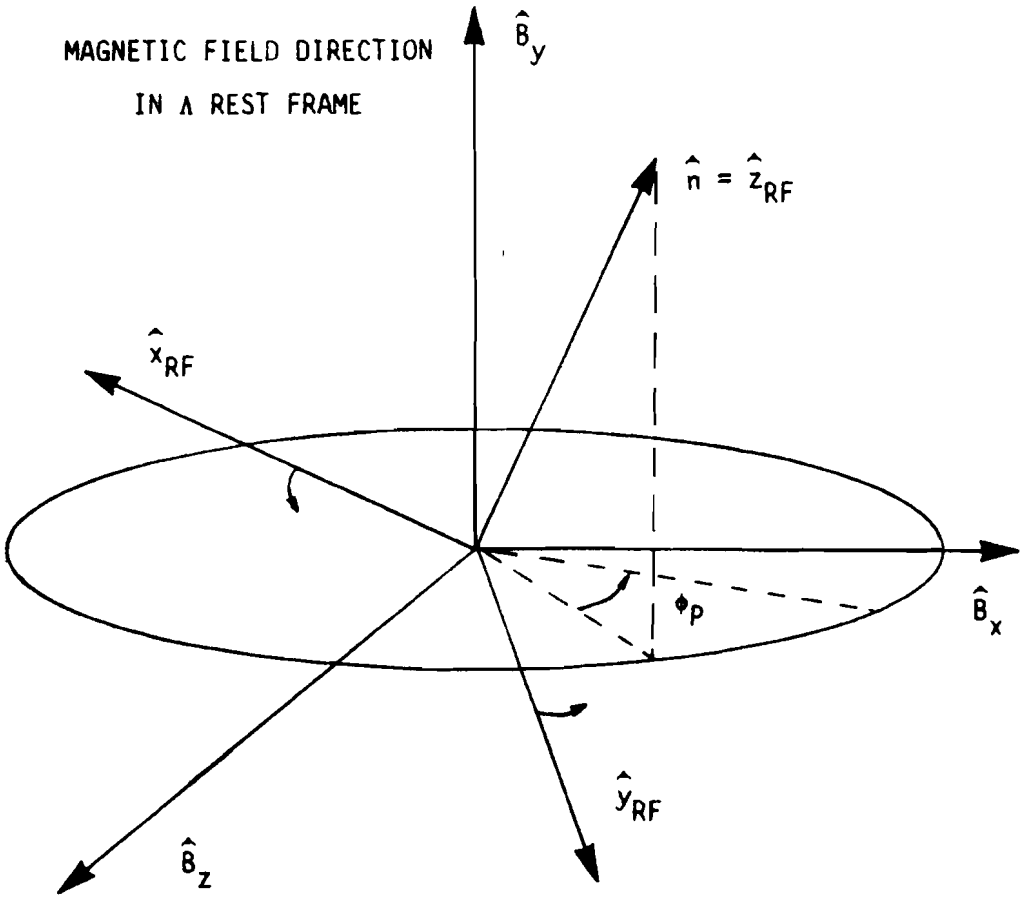

Figure 3.18. Precession of Λ Spin in Sweeping Magnet Field.

3.4.2 Analysis Method

Equation 3.1 assumes a continuous distribution in the variables $\cos\theta$ and ϕ as well as 4π acceptance. The distribution must be modified to allow for finite binning of the data in $\cos\theta$ and ϕ and the loss in acceptance induced by the apparatus. The binning was chosen such that the bin width was much larger than the error in the $\cos\theta$ and ϕ measurement (Section 3.3). The largest number of bins consistent with this constraint was about 20. In order to maximize the statistical power the data were analyzed with succeedingly fewer bins until the error remained constant. Optimal binning was achieved with ten bins in $\cos\theta$ and ϕ. The values of A_x, A_y and A_z were independent of the binning down to 5 bins.

The probability for a given $\cos\theta$ bin i and ϕ bin j is obtained by integrating over solid angle $\Delta\Omega$.

$$P_{ij} = \frac{1}{4\pi} \iint_{\Delta\Omega} [1 + A_x \sin\theta\cos\phi + A_y \sin\theta\sin\phi + A_z \cos\theta]\, d\Omega$$

$$= \frac{1}{4\pi} [\Delta x \Delta\phi + 2A_x I(x)_i \sin(\tfrac{\Delta\phi}{2})\cos\phi_j + 2A_y I(x)_i \sin(\tfrac{\Delta\phi}{2})\sin\phi_j + A_z x_i \Delta x \Delta\phi]$$

where $x_i = \cos\theta_i$

and

$$I(x) = \int_{x-\frac{\Delta x}{2}}^{x+\frac{\Delta x}{2}} \sqrt{1-x^2}\, dx.$$

The acceptance of the experiment was not uniform in solid angle hence the decay distribution is modified by a factor A_{ij} for each $\cos\theta$, ϕ bin. A_{ij} was calculated using the Monte Carlo by dividing M_{Rij}, the number of Monte Carlo events surviving all geometrical and kinematic cuts by M_{Gij}, the number of raw Monte Carlo events generated. The modified distribution is then given by

$$P_{Mij} = \frac{1}{4\pi} \left[A_{ij}\Delta x\Delta\phi + 2A_x A_{ij} I(x)_i \cos\phi_j \sin\left(\frac{\Delta\phi}{2}\right)\right.$$

$$+ 2A_y A_{ij} I(x)_i \sin\phi_j \sin\left(\frac{\Delta\phi}{2}\right)$$

$$\left. + A_z A_{ij} \Delta x \Delta\phi \cos\theta_i\right]$$

Summing over i and j, PM_{ij} becomes

$$\sum_{ij} P_{ij} \approx \sum_{ij} A_{ij} \frac{\Delta x \Delta\phi}{4\pi}$$

where due to the symmetry of A_{ij} the other terms may be neglected.

The symmetry properties of A_{ij} extend separately to both $\cos\theta$ and ϕ allowing a convenient separation of the distribution into parts containing only $\cos\theta$ and functions of ϕ. Summing over j the normalized distribution for $\cos\theta$ is

$$P_{Mi} = \frac{1}{\sum_{ij} A_{ij}} \sum_j A_{ij}[\ 1 + A_z \cos\theta_i]$$

Summing over i the normalized distribution for ϕ is

$$P_{Mj} = \frac{1}{\Delta x \Delta\phi \sum_{ij} A_{ij}} \Big[\ 2A_x \sum_i I(x)_i\ A_{ij} \sin(\tfrac{\Delta\phi}{2}) \cos\phi_j$$

$$+\ 2A_y \sum_i I(x)_i\ A_{ij} \sin(\tfrac{\Delta\phi}{2}) \sin\phi_j\ \Big]$$

$$+\ \frac{\sum_i A_{ij}}{\sum_{ij} A_{ij}}$$

In each case above the neglected terms introduce an error which is negligible compared to the statistical error.

The data were binned in kinematic variables p_T and X_F and fit using least squares to obtain the best values of A_x, A_y and A_z.

3.4.3 Biases

One of the most important problems confronting the analysis of polarization data is that of biases which introduce non-zero polarization. Geometrical biases induced by the acceptance are most likely and other biases, in order of decreasing likelihood, could be caused by polarization of the incident beam and parity nonconserving polarization in production. In this experiment there were several methods to determine and correct for the existence of biases.

The measurement of the parity nonconserving asymmetries A_x and A_y of the general Λ or $\bar{\Lambda}$ decay distribution afford a unique method for detecting biases. Since parity is conserved in the strong interactions A_x and A_y should both be zero. A_x is a measure of the transverse bias and A_y measures biases longitudinally. That A_x and A_y be zero is a necessary condition for confidence in the measurement of A_z, the parity-conserving asymmetry. Described below are additional bias checks.

K^0 Analysis

A relatively large sample of K^0_S's (4×10^4) was obtained from the reaction $K^- + p \rightarrow K^0_S + X$. The final sample included events which fit the K^0_S hypothesis and had a decay $p_\perp$ greater than 0.12 GeV/c thus ensuring a clean sample of K^0_S's. These events were analyzed for asymmetries in the $\cos\theta$ distribution using exactly the same method as used for Λ's and $\bar{\Lambda}$'s. Since K^0_S's have spin zero A_x, A_y and A_z should all be zero.

Magnetic Field Switching

Biases depending on the orientation of the sweeping and analyzing magnet fields were allowed for by periodically reversing the field direction of both the sweeping and analyzing magnets from $+\hat{y}$ to $-\hat{y}$ in the experiment coordinate system. The field direction of the two magnets relative to each other was always the same. The results, presented in Section 4, will show the data separately for magnet up and magnet down as well as combined. As expected, due to the rotation of the production plane normal, there are no significant systematic effects between magnet up and magnet down.

Lambda Lifetime

Lifetime measurements afford a sensitive check of the longitudinal acceptance of the experiment since they depend on the measured decay length and momentum of the neutral V's. Figure 3.19 shows the Λ, $\bar{\Lambda}$ and K^0_S lifetimes as a function of their momentum compared with the current value [15] represented by the horizontal lines in the plot. The current values, $\tau_\Lambda = 2.632 \pm 0.02 \times 10^{-10}$ and $\tau_{K^0_S} = 0.8923 \pm 0.0022 \times 10^{-10}$, compare favorably with the lifetimes measured in this experiment, $\langle\tau_\Lambda\rangle = 2.56 \pm 0.06 \times 10^{-10}$ and $\langle\tau_{K^0_S}\rangle = 0.87 \pm 0.01 \times 10^{-10}$ where the Λ and $\bar{\Lambda}$ measurements are combined.

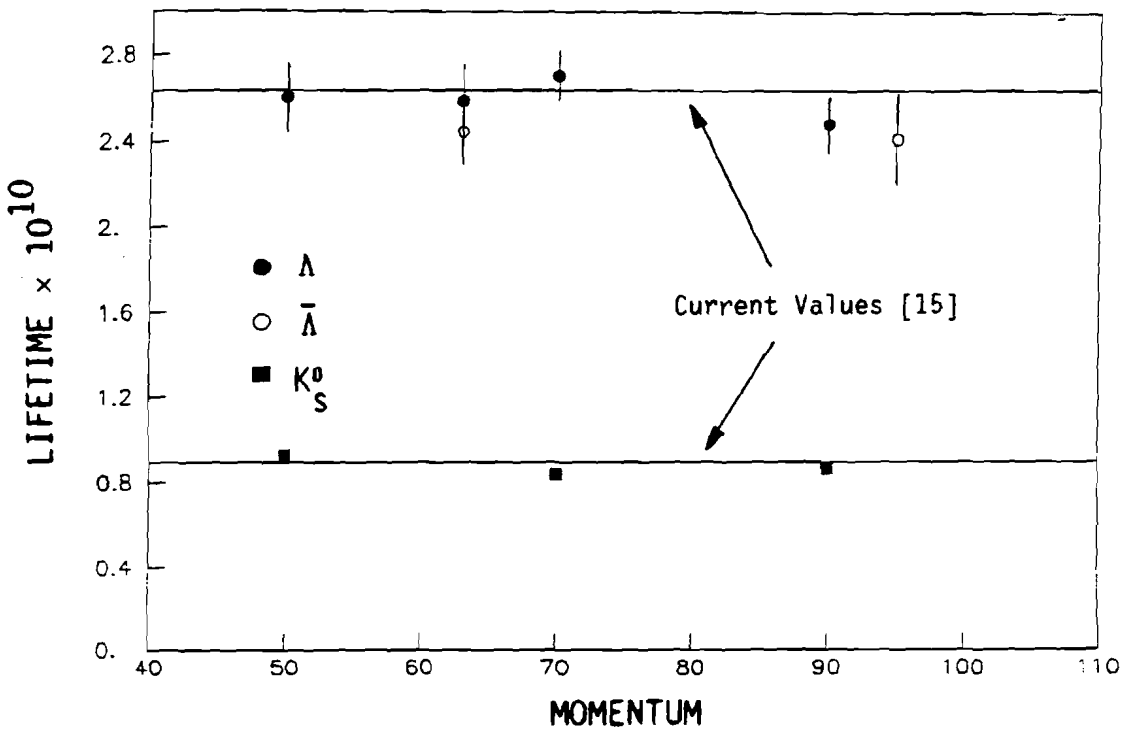

Figure 3.19. Lambda, $\bar{\Lambda}$ and K^0_S Lifetimes vs Momentum.

SECTION 4

RESULTS AND CONCLUSIONS

The results of the asymmetry analysis, $A_x = \alpha P_x$, $A_y = \alpha P_y$, and $A_z = \alpha P_z$ are presented as a function of X_F and P_T. The data for magnet up/magnet down were examined separately for magnet orientation dependent biases. Since no significant biases were detected the data were combined for the final analysis presented here. The combined data were fit to $A_i = \alpha P_i = \beta_i P_T$, where $i = x, y, z$, recognizing that the polarization must be zero at $P_T = 0$. Since a similar constraint is not known to exist for the polarization as a function of X_F and given that statistics are limited, the average values of A_x and A_y were calculated as a bias check.

4.1 Bias Checks

In order to establish a firm foundation on which to present the data it is necessary to first examine the results of the bias analysis.

4.1.1 A_x ,A_y

In addition to comparing data distributions of kinematic and geometric variables to Monte Carlo generated distributions the entire analysis procedure may be checked by determining the parity nonconserving components of the Λ or $\bar{\Lambda}$ and K^0_s decay distributions. These measurements are more sensitive to second order correlation effects between parameters. As described in Section 3.4.3, A_x and A_y measure in a global fashion the ability of the analysis procedure to correct the acceptance of the apparatus. A_x and A_y are directly related to the physical apparatus and hence are sensitive to geometrically induced biases. Figures 4.1 and 4.2 show the results of the parity nonconserving asymmetry analysis for the three Λ and $\bar{\Lambda}$ production channels as a function of P_T and X_F with the same binning as used for the subsequent A_z analysis. The results, given in Table 4.1, indicate that there is no significant bias.

Table 4.1. Results of Asymmetry Analysis for Λ and $\bar{\Lambda}$.

Slope from the fit $A_i = \beta_i P_T$

Channel	β_x	β_y
$p\ p \to \Lambda$	-0.014 ± 0.033	0.044 ± 0.032
$\bar{p}\ p \to \bar{\Lambda}$	0.049 ± 0.048	0.009 ± 0.046
$K^- p \to \Lambda$	0.022 ± 0.036	0.028 ± 0.036

Average asymmetry for data binned in X_F

Channel	$\langle A_x \rangle$	$\langle A_y \rangle$
$p\ p \to \Lambda$	-0.007 ± 0.019	0.003 ± 0.018
$\bar{p}\ p \to \Lambda$	0.029 ± 0.027	-0.004 ± 0.026
$K^- p \to \Lambda$	-0.005 ± 0.021	0.031 ± 0.021

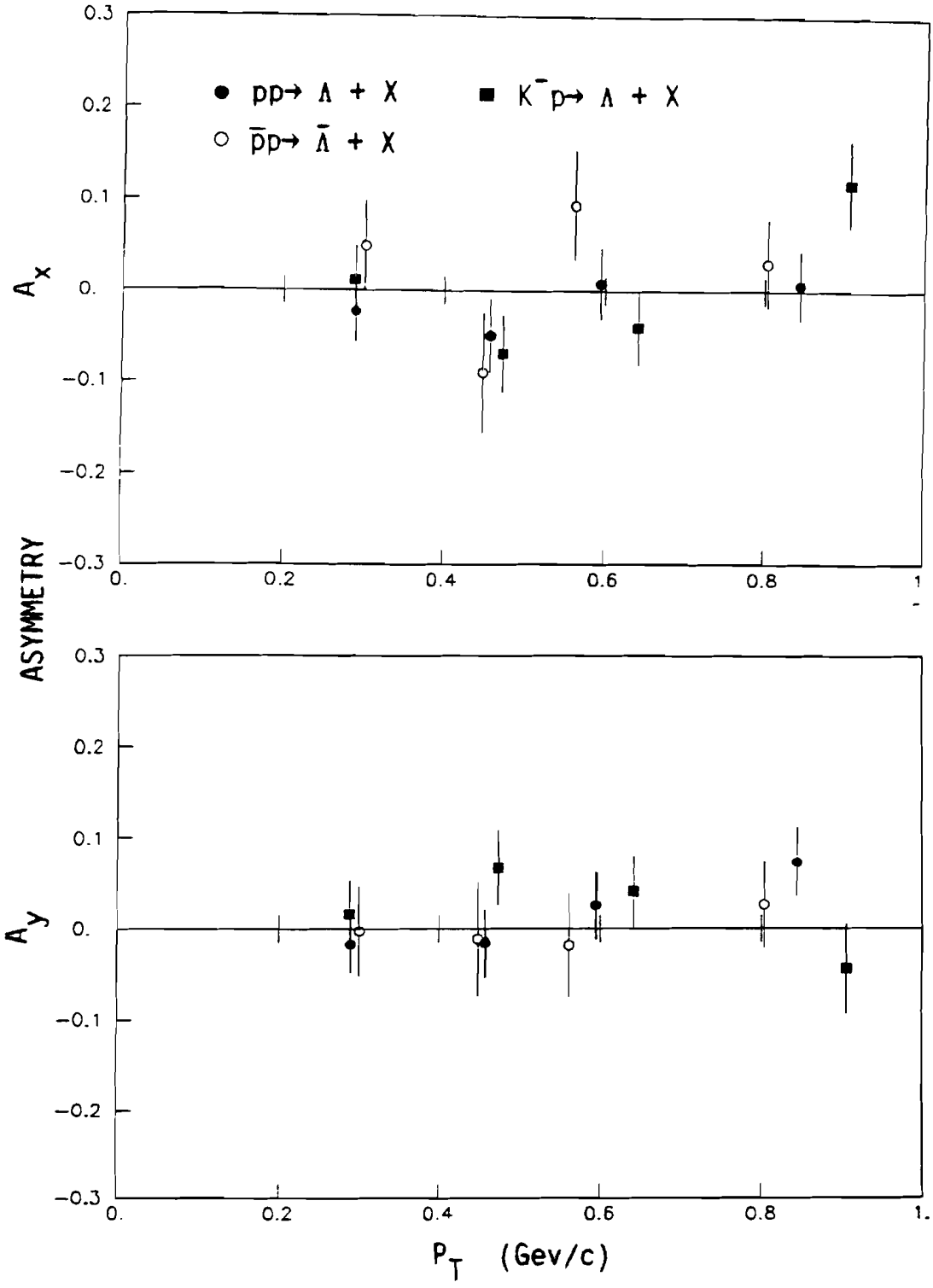

Figure 4.1. Parity Nonconserving Asymmetries as a Function of P_T.

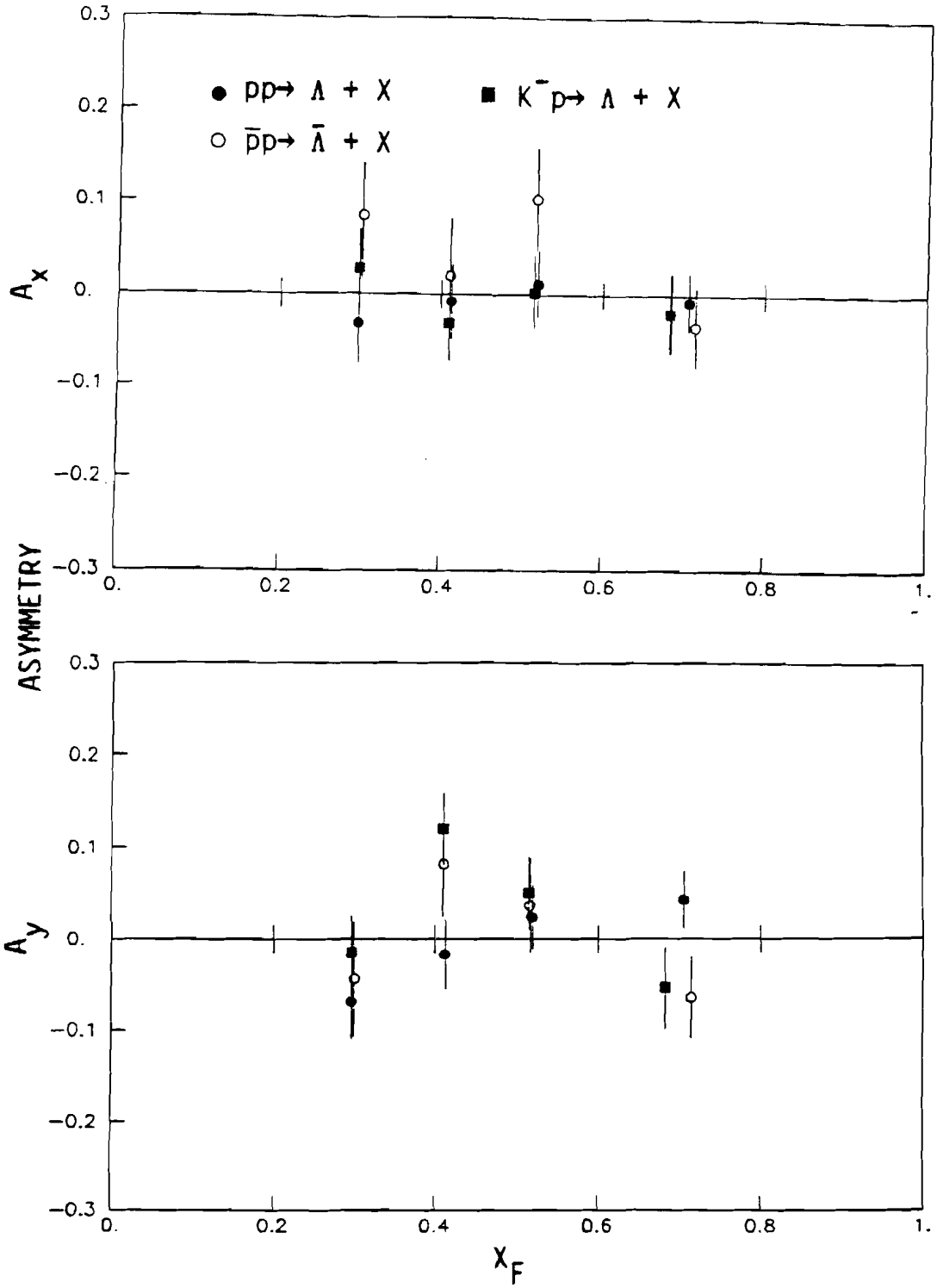

Figure 4.2. Parity Nonconserving Asymmetries as a Function of X_F.

4.1.2 K^0_S Analysis

Additional information may be obtained by analyzing the spin zero K^0_S's for asymmetries. Although the Λ and K^0_S decays studied are both two-body the apparatus is more uniformly sampled by the pions from the K^0_S due to its symmetric decay. The protons from the Λ decay primarily sample the center of the spectrometer while the pions illuminate the edges. However, the measurement of asymmetries yields generally useful information on the acceptance and the effect of K^0_S background contributions for the Λ and $\bar{\Lambda}$ analysis. Figures 4.3 - 4.5 and Table 4.2 show the results of the K^0_S asymmetry analysis.

Table 4.2. Results of Asymmetry Analysis for K^0_S.

Slope from the fit to $A_i = \beta_i P_T$			
Channel	β_x	β_y	β_z
$K^- p \rightarrow K^0_S$	0.037 ± 0.027	-0.021 ± 0.032	0.006 ± 0.022

Average asymmetry for data binned in X_F			
Channel	$\langle A_x \rangle$	$\langle A_y \rangle$	$\langle A_z \rangle$
$K^- p \rightarrow K^0_S$	0.026 ± 0.015	-0.027 ± 0.017	-0.002 ± 0.012

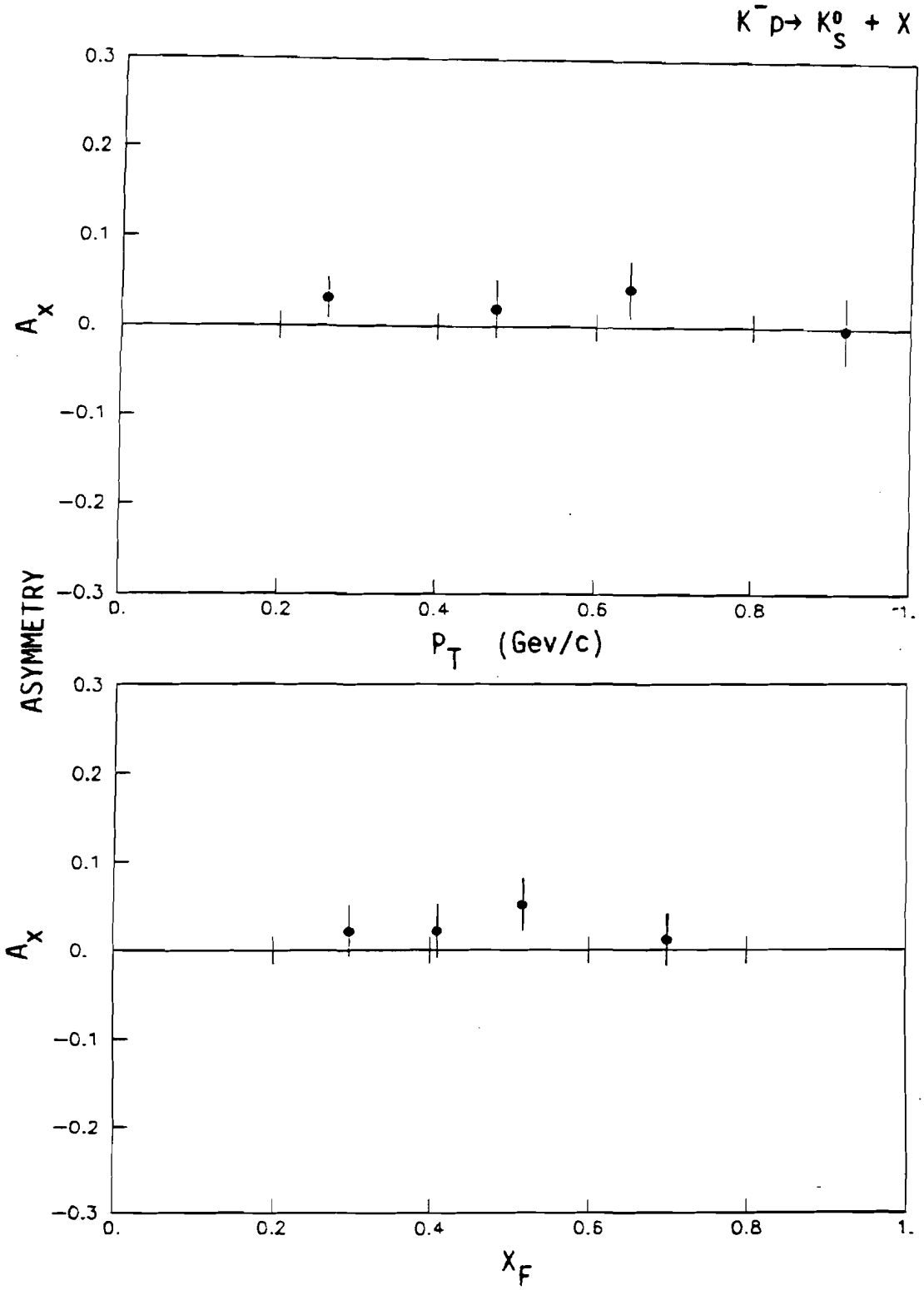

Figure 4.3. Asymmetry A_x as a Function of X_F and P_T for $K^- p \to K^0_S$.

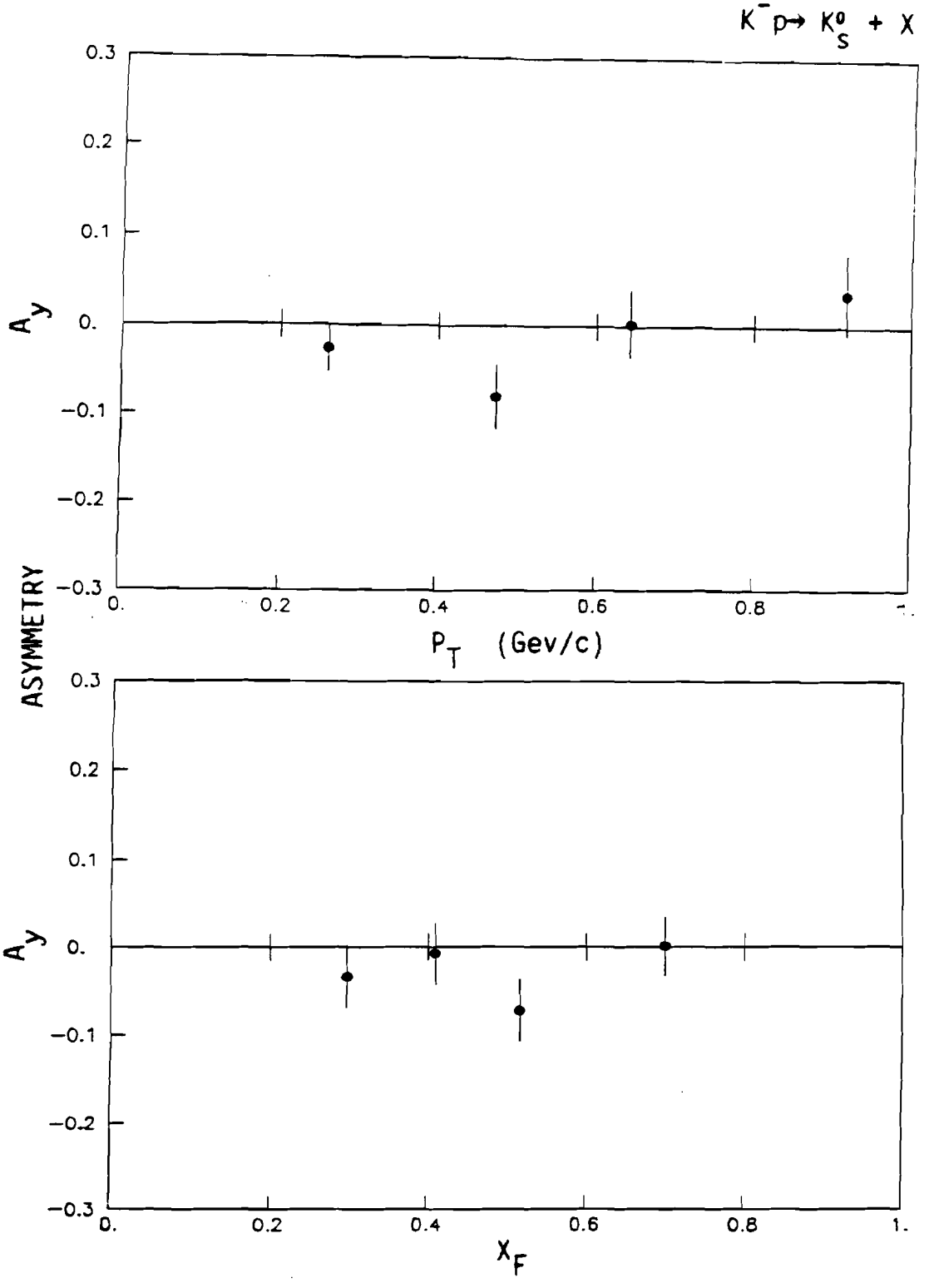

Figure 4.4. Asymmetry A_y as a Function of X_F and P_T for $K^-p \rightarrow K^0_S$.

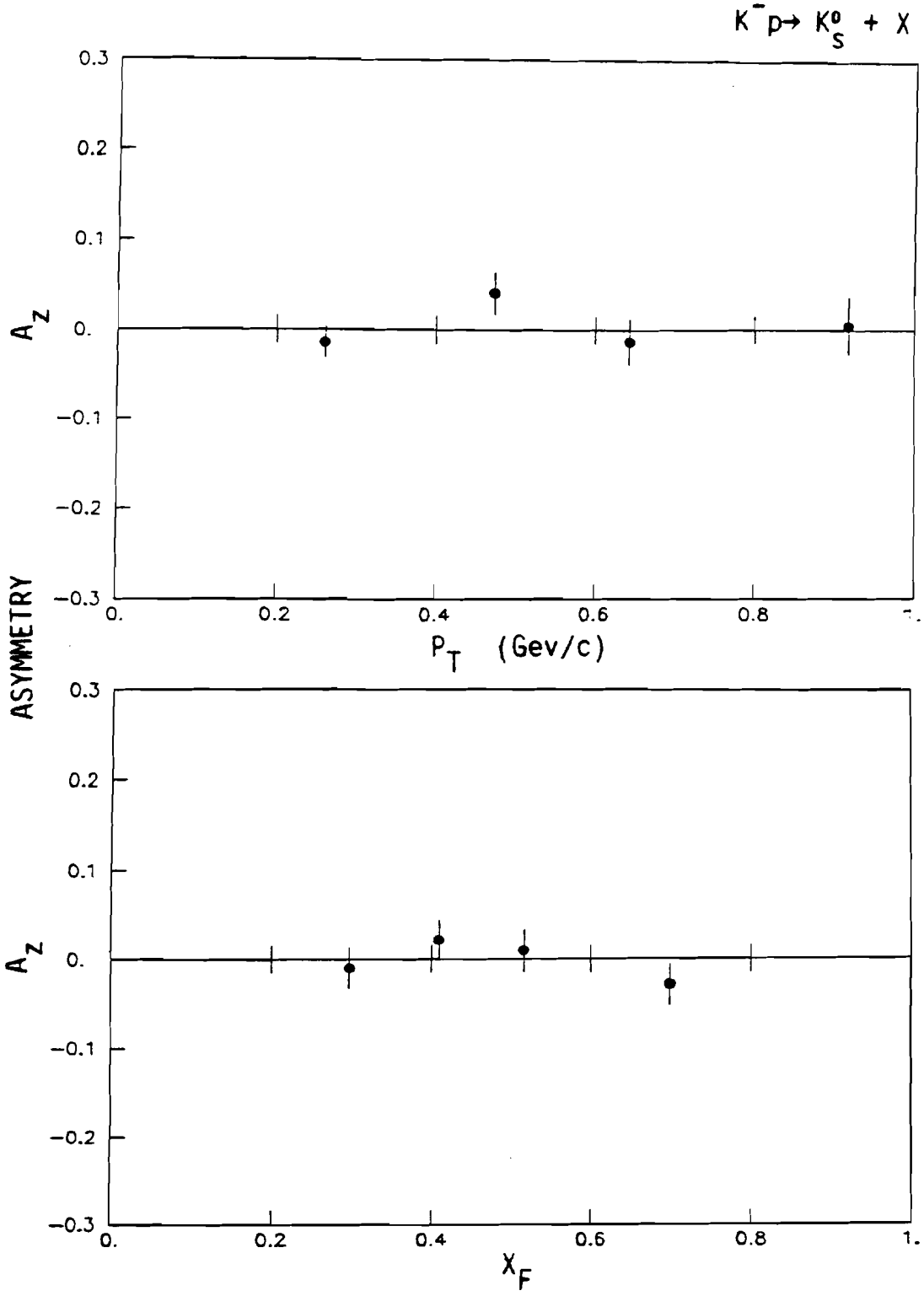

Figure 4.5. Asymmetry A_Z as a Function of X_F and P_T for $K^- p \to K^0_S$.

4.2 pp→ Λ Results

The data for the channel pp→ Λ were divided into equally populated bins in P_T and X_F. Figure 4.6 shows the asymmetry as a function of P_T and X_F for the magnet up/magnet down data and Figure 4.7 shows the combined data. The polarization was extracted from the asymmetry for the combined data by $P_z = A_z/\alpha_\Lambda$ where $\alpha_\Lambda = -0.642$ [16] and is plotted in Figure 4.8. The results of linear fits to the data as a function of P_T and X_F are given in Table 4.3 and Figure 4.9. The polarization is consistent with a linearly increasing P_T dependence. However, the results of the 2 parameter fit to the data as a function of X_F indicate that a linear hypothesis over the full range of X_F is not valid. Due to a lack of sufficient data for a more detailed study of X_F dependence no quantitative analysis was attempted.

Table 4.3. Results of pp→ Λ Polarization Analysis.

$$P_z = \beta_z P_T$$

β_z	$\langle P_z \rangle$	$P_z(P=0.8)$	χ^2
0.130 ± 0.046	0.063 ± 0.026	0.104 ± 0.035	2.4

$$P_z = \gamma_z X_F + \delta_z$$

γ_z	δ_z	$\langle P_z \rangle$	χ^2
0.183 ± 0.016	-0.04 ± 0.03	0.061 ± 0.026	10.6

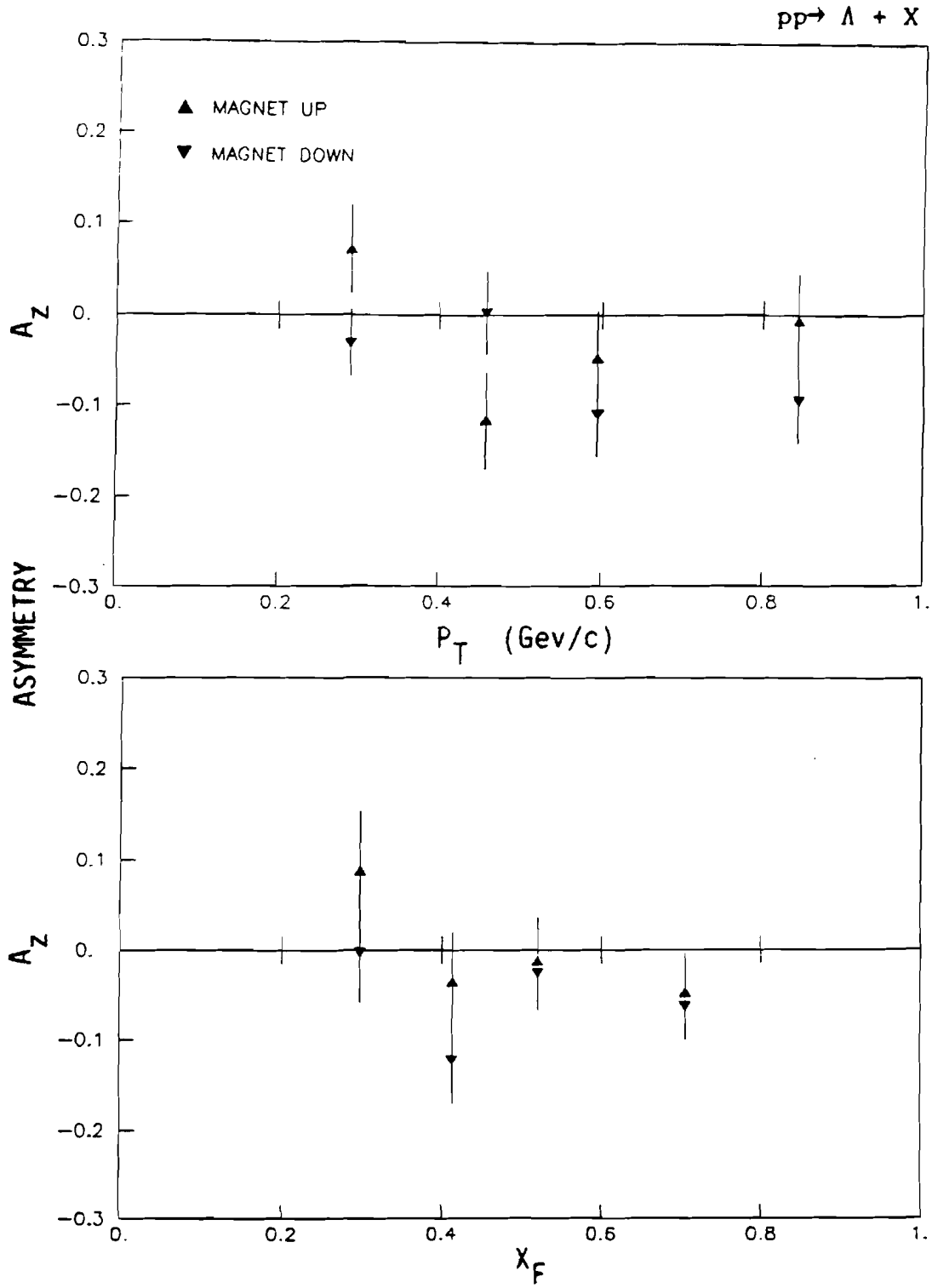

Figure 4.6. Parity Conserving Asymmetry A_Z as a Function of P_T and X_F for pp→ Λ Magnet Up/Magnet Down Data.

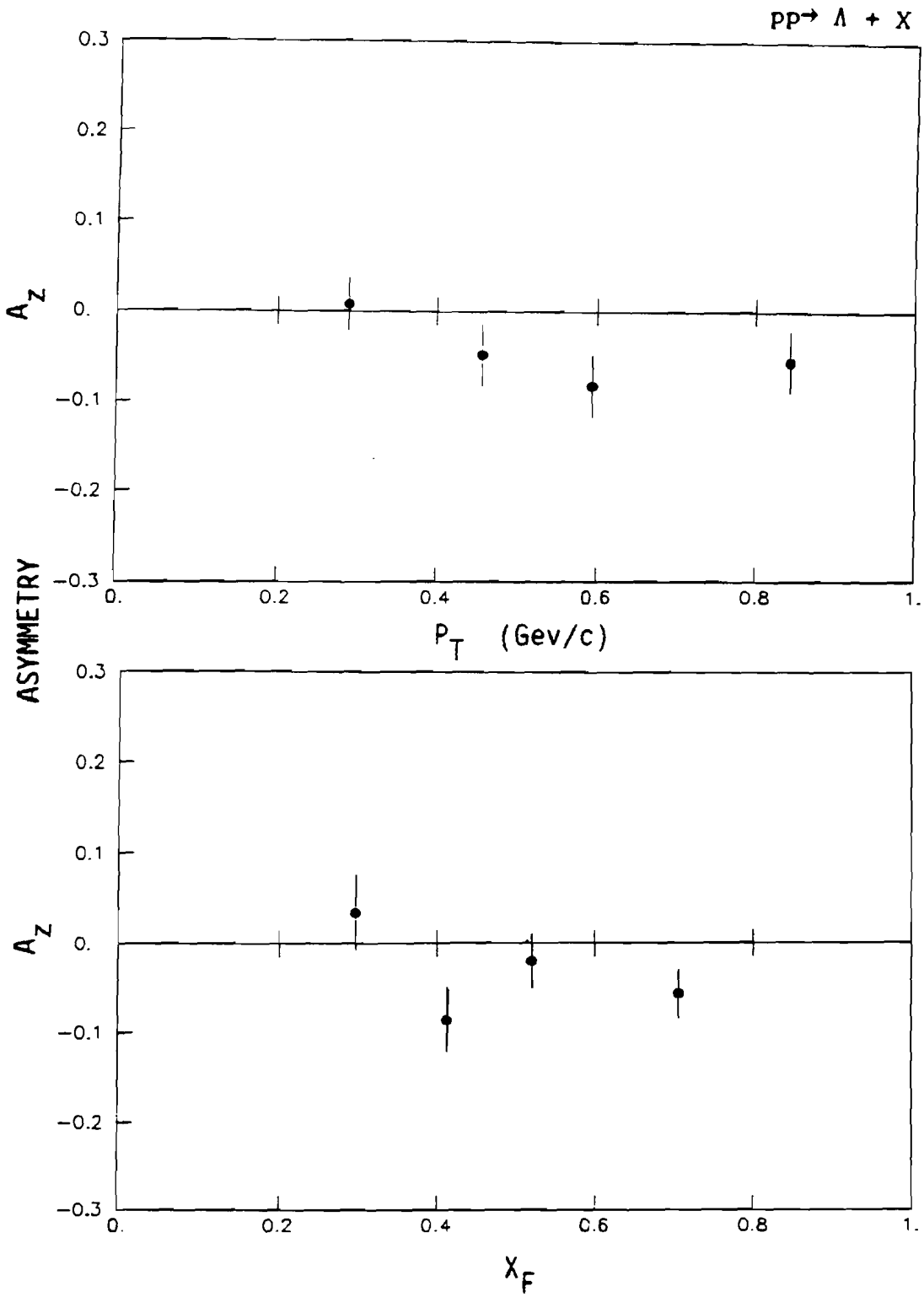

Figure 4.7. Parity Conserving Asymmetry A_z as a Function of P_T and X_F for pp→ Λ Combined Data.

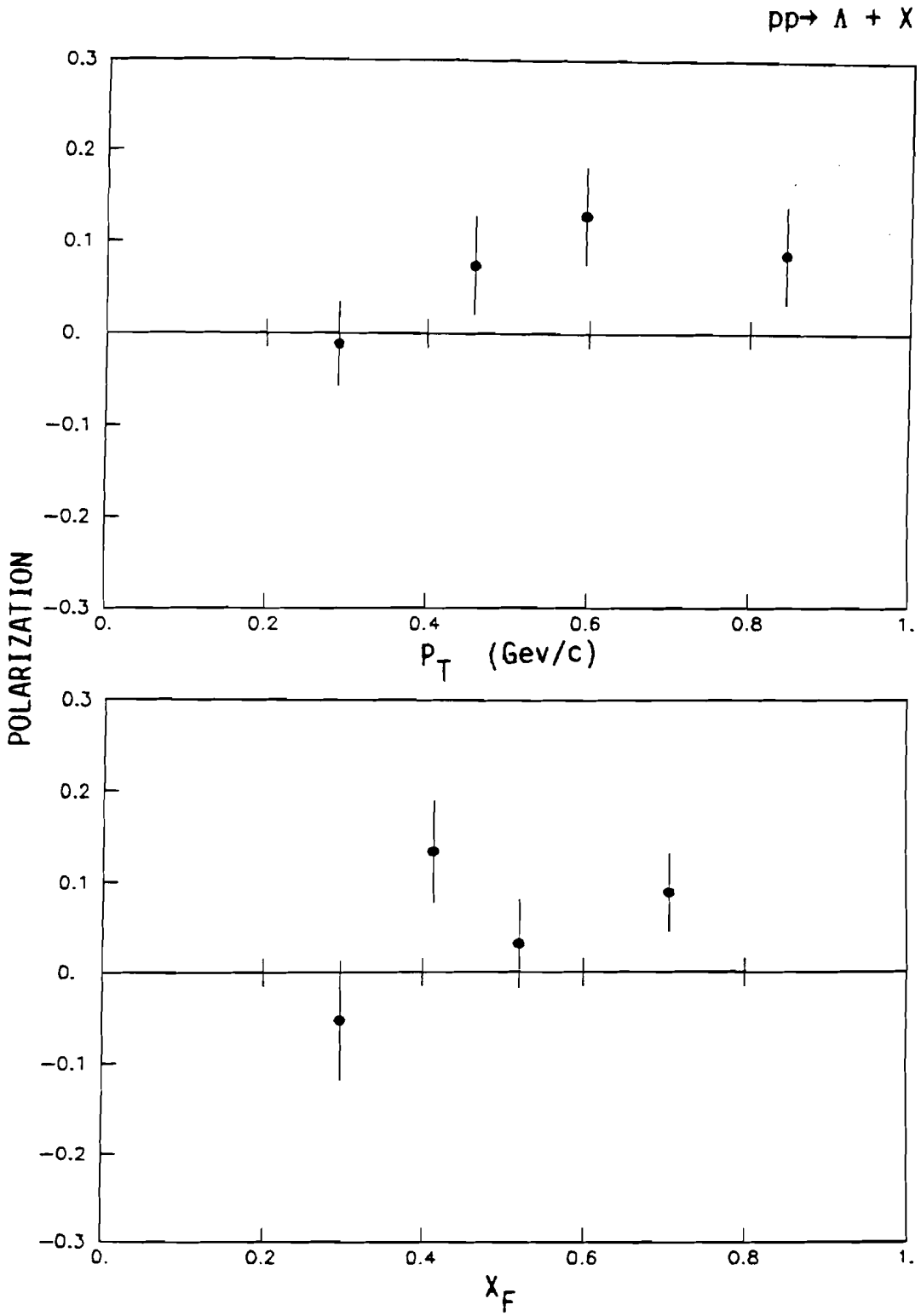

Figure 4.8. Polarization as a Function of P_T and X_F for pp→ Λ.

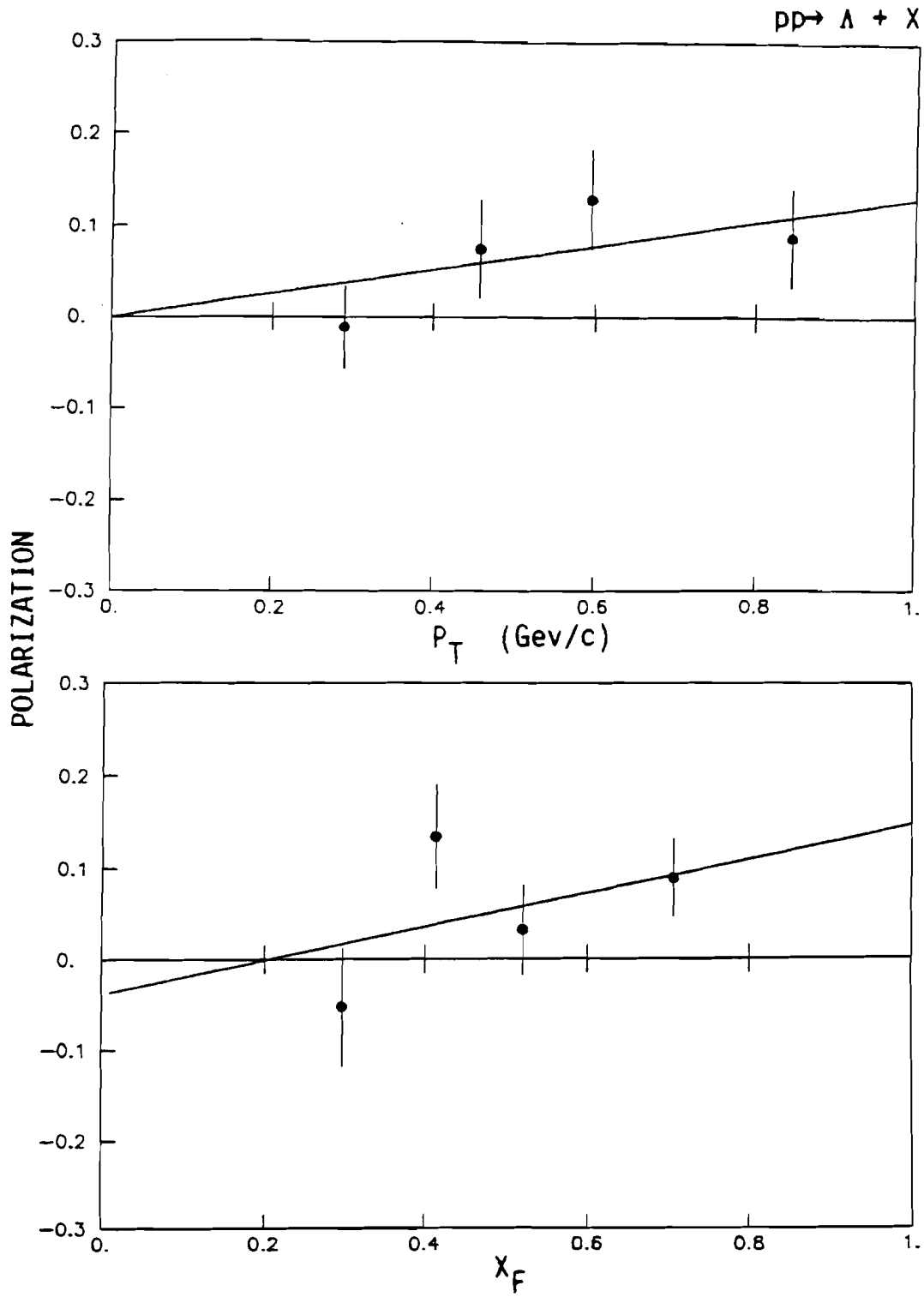

Figure 4.9. Polarization as a Function of P_T and X_F for pp→ Λ with Fits.

The polarization of Λ's produced by protons on beryllium and hydrogen has been studied extensively by [17,18] at incident beam momenta of 300 and 400 GeV/c. Within the kinematic range of this experiment, $0.0 < P_T < 1.0$, they find that the polarization increases linearly with P_T, is slowly increasing with X_F and independent of the center of mass energy.

The data from [18] are shown plotted in Figure 4.10 with the data from this experiment as a function of P_T and a comparison of the results is given in Table 4.4.

Table 4.4. Comparison of Λ Polarization for the Channel $pp \rightarrow \Lambda$ at 175 GeV/c and 400 GeV/c.

	$P_z = \beta_z P_T$		
	β_z	$\langle P_z \rangle$	$P_z(P=0.8)$
	0.130 ± 0.046	0.063 ± 0.026	0.104 ± 0.037
[18]	0.097 ± 0.002	0.068 ± 0.002	0.078 ± 0.002

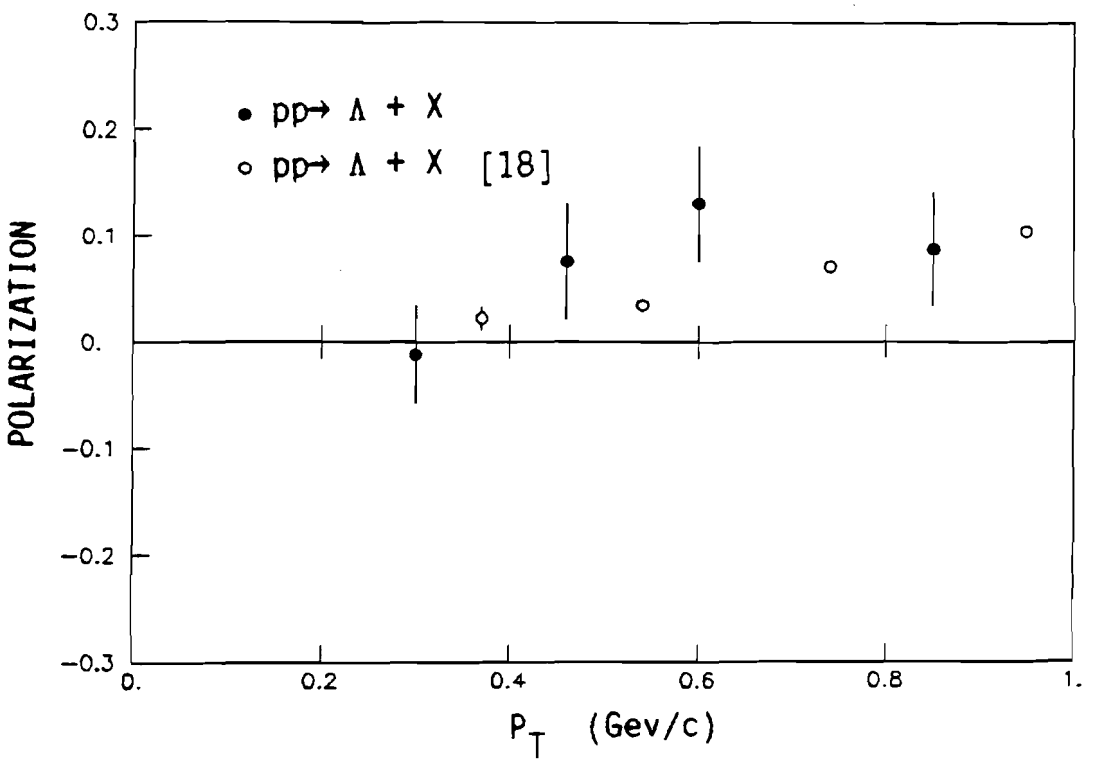

Figure 4.10. Comparison of Polarization for pp→ Λ from this Experiment and Reference 18.

4.3 $\bar{p}p \to \bar{\Lambda}$ Results

In Figures 4.11 and 4.12 A_z is shown as a function of P_T and X_F. The polarization is obtained from $P_z = A_z/\alpha_{\bar{\Lambda}}$ where $\alpha_{\bar{\Lambda}} = -\alpha_{\Lambda} = +0.642$. P_z is plotted as a function of P_T and X_F in Figure 4.13 and is shown with the fits in Figure 4.14. The results, given in Table 4.5, are consistent with an increase in polarization as a function of P_T with the sign the same as that for Λ's from protons. As a function of X_F the polarization is non-zero only at large X_F and a linear hypothesis is not valid.

Table 4.5. Results of $\bar{p}p \to \bar{\Lambda}$ Polarization Analysis.

$$P_z = \beta_z P_T$$

β_z	$\langle P_z \rangle$	$P_z(P=0.8)$	χ^2
0.171 ± 0.066	0.070 ± 0.038	0.140 ± 0.050	4.0

$$P_z = \gamma_z X_F + \delta_z$$

γ_z	δ_z	$\langle P_z \rangle$	χ^2
0.368 ± 0.024	-0.130 ± 0.043	0.069 ± 0.038	6.8

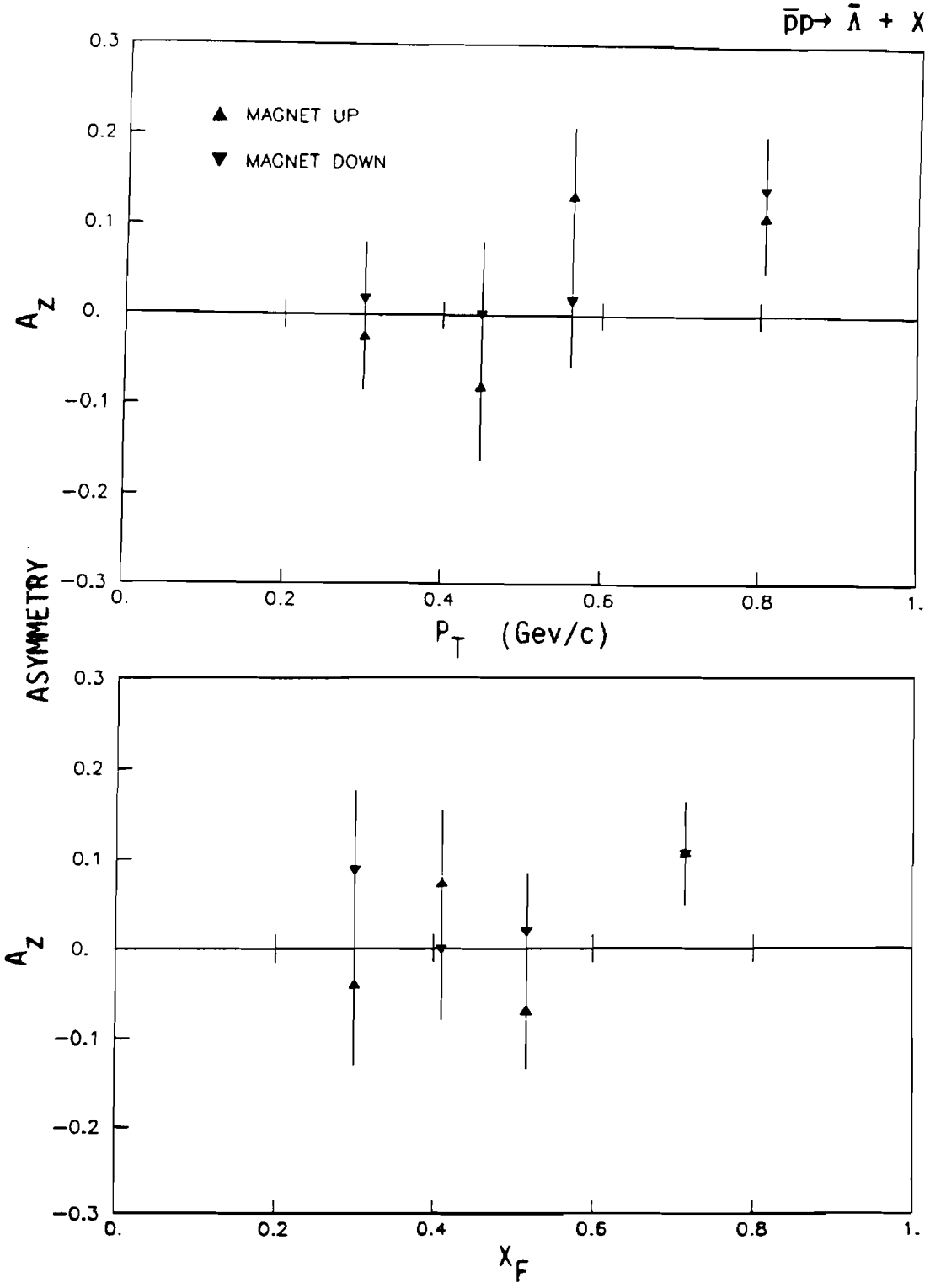

Figure 4.11. Parity Conserving Asymmetry A_Z as a Function of P_T and X_F for $\bar{p}p \rightarrow \bar{\Lambda}$ Magnet Up/Magnet Down Data.

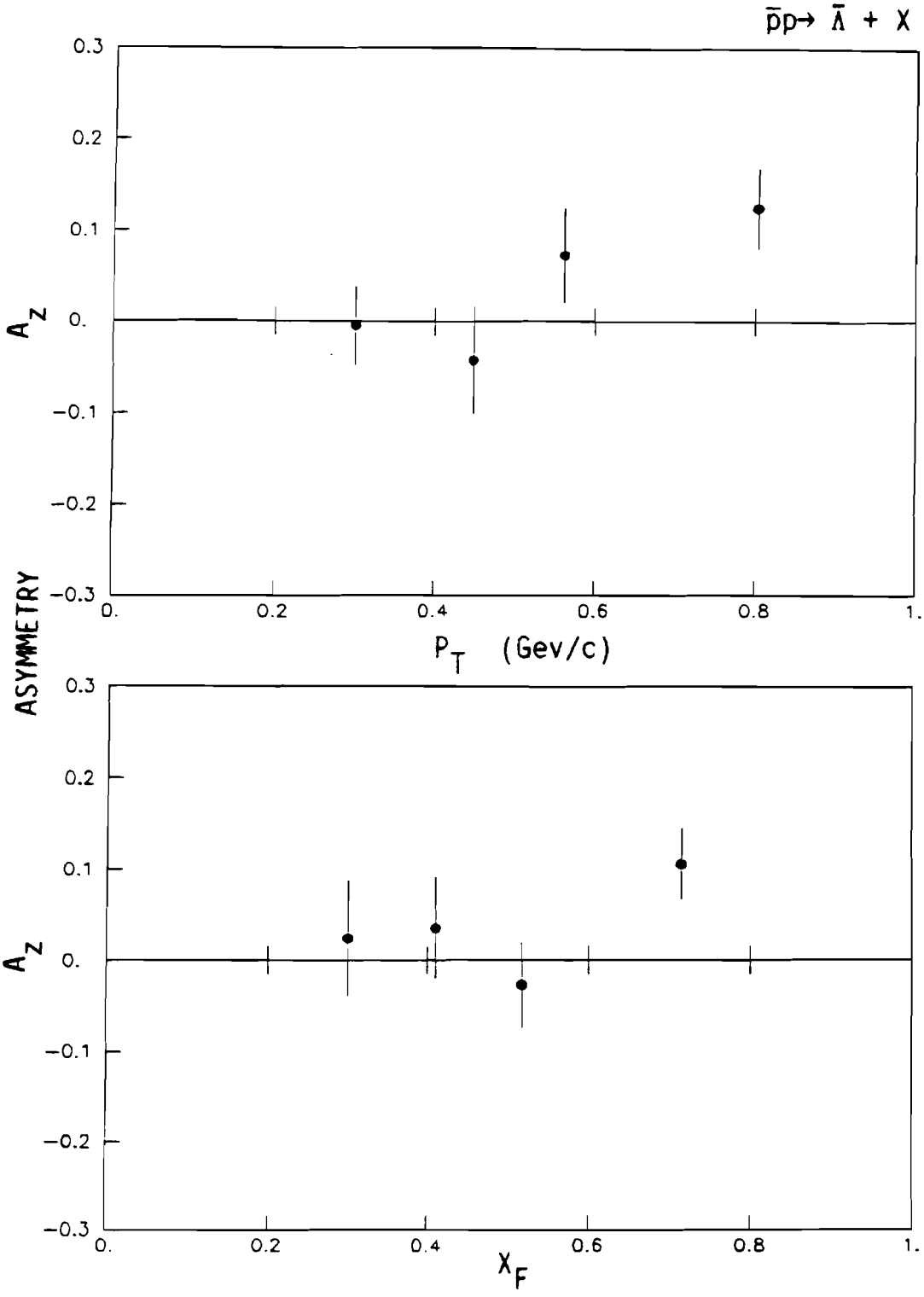

Figure 4.12. Parity Conserving Asymmetry A_z as a Function of P_T and X_F for $\bar{p}p \rightarrow \bar{\Lambda}$ Combined Data.

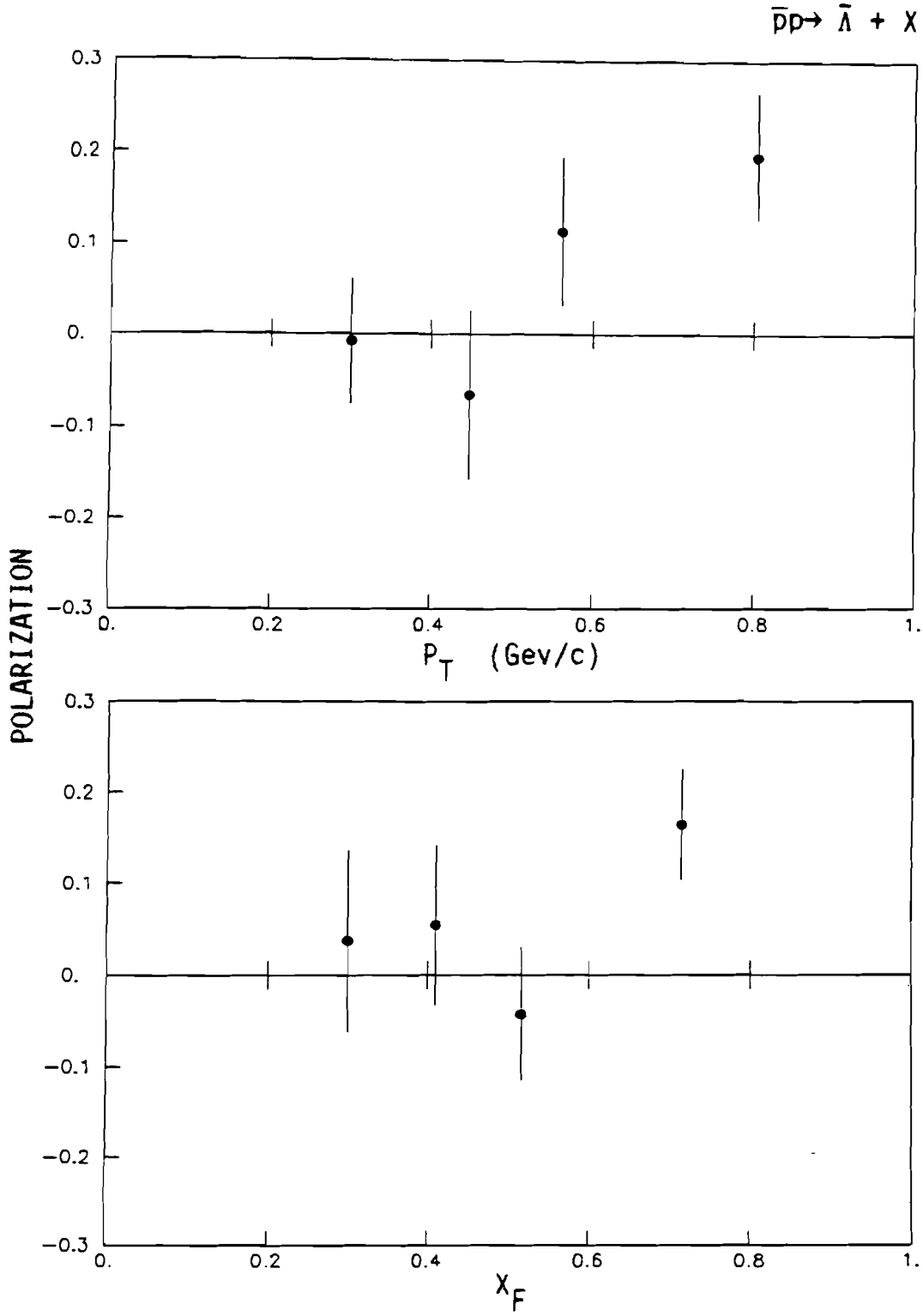

Figure 4.13. Polarization as a Function of P_T and X_F for $\bar{p}p \to \bar{\Lambda}$.

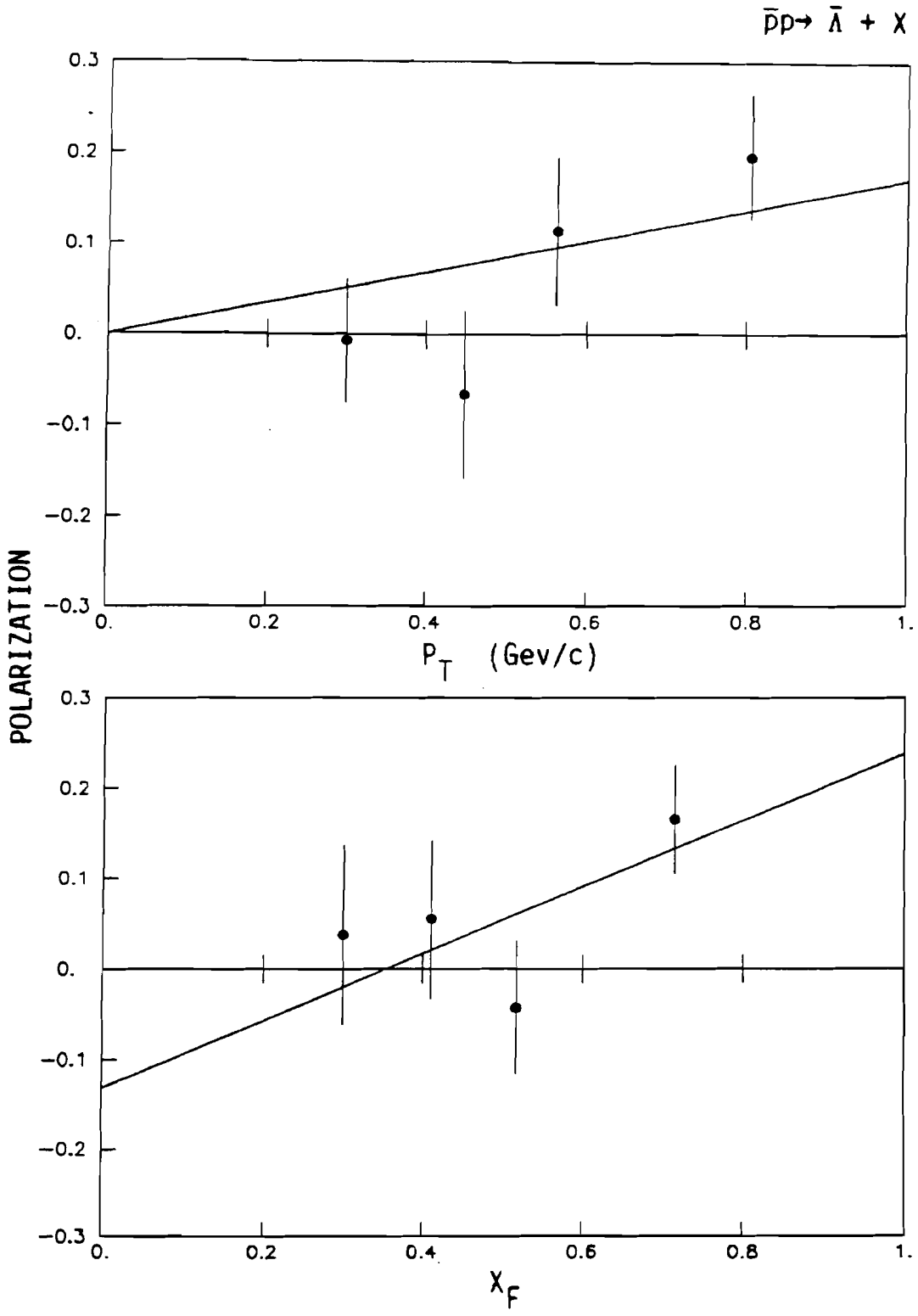

Figure 4.14. Polarization as a Function of P_T and X_F for $\bar{p}p \to \bar{\Lambda}$ with Fits.

The $\bar{p}p \rightarrow \bar{\Lambda}$ and $pp \rightarrow \Lambda$ data are compared in Figure 4.15. Though the low statistics of the $\bar{p}p \rightarrow \bar{\Lambda}$ data prevent any detailed analysis of the X_F and P_T dependence it may still be observed that the polarization of $\bar{\Lambda}$'s produced by $\bar{p}$'s is consistent in sign and magnitude with the polarization of Λ's produced by protons. Previous experiments were performed a 6 GeV/c [19] and in a colliding beam experiment at CERN [20] with a center of mass energy of 31 GeV. The polarization data from Reference 20 and this experiment are compared in Figure 4.16 and have the same qualitative behavior despite the large difference in center of mass energy.

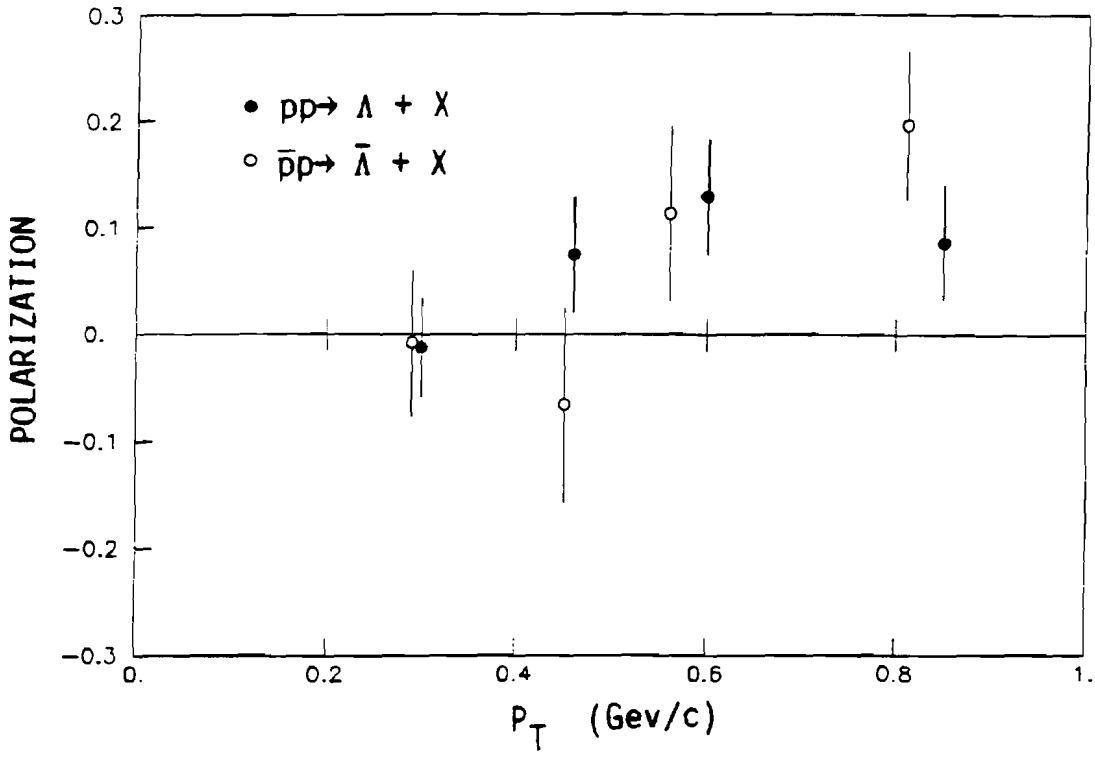

Figure 4.15. Comparison of Polarization for $\bar{p}p \rightarrow \bar{\Lambda}$ with $pp \rightarrow \Lambda$.

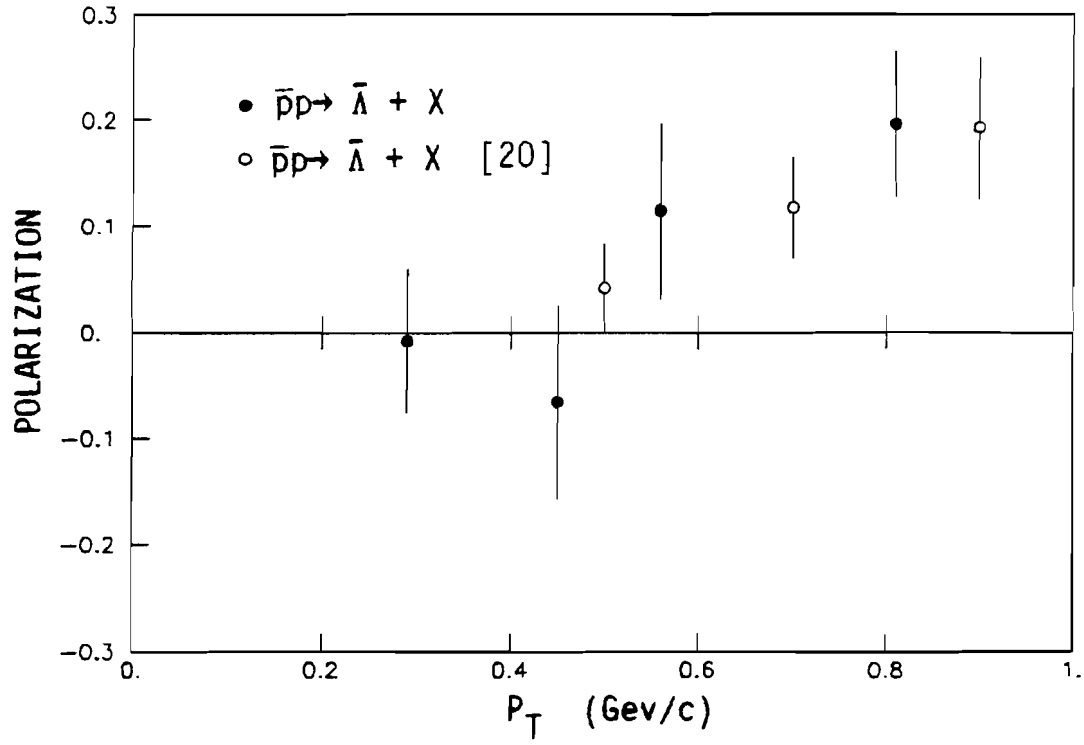

Figure 4.16. Comparison of Polarization for $\bar{p}p \to \bar{\Lambda}$ from this Experiment and Reference 20.

4.4 $K^-p \to \Lambda$ Results

The polarization of Λ's produced by K^- has been previously studied at incident beam momenta of 32 GeV/c and below [21,22,23,24,25]. This experiment presents the first data at high energy. In Figures 4.17-4.20 are shown the asymmetries and polarization. The results (Table 4.6) indicate a striking difference between the polarization of Λ's and $\bar{\Lambda}$'s from p's and $\bar{p}$'s respectively and the Λ's produced by K^- both in sign and magnitude.

Table 4.6. Results of $K^-p \to \Lambda$ Polarization Analysis.

$P_z = \beta_z P_T$			
β_z	$\langle P_z \rangle$	$P_z(P=0.8)$	χ^2
-0.747 ± 0.047	-0.417 ± 0.028	-0.600 ± 0.040	3.0

$P_z = \gamma_z X_F + \delta_z$			
γ_z	δ_z	$\langle P_z \rangle$	χ^2
-0.447 ± 0.018	-0.195 ± 0.036	-0.413 ± 0.028	7.4

The polarization data for $K^-p \rightarrow \Lambda$ at 8.25 GeV/c are presented in [22]. The results of this experiment and Reference 22 are compared in Figure 4.21 as a function of X_F and P_T. The qualitative features are the same supporting the general observation of energy independence of polarization phenomena.

Another interesting comparison can be made with the data from this experiment and the polarization of $\bar{\Lambda}$'s produced by K^+. $K^+p \rightarrow \bar{\Lambda}$ has been done by [26] at incident momenta of 32 and 70 GeV/c. Figure 4.22 shows the $K^-p \rightarrow \Lambda$ polarization from this experiment with the $K^+p \rightarrow \bar{\Lambda}$ data from Reference 26 as a function of X_F and P_T. The polarization in the two channels has the same sign and approximately the same dependence on X_F but differs greatly in P_T dependence.

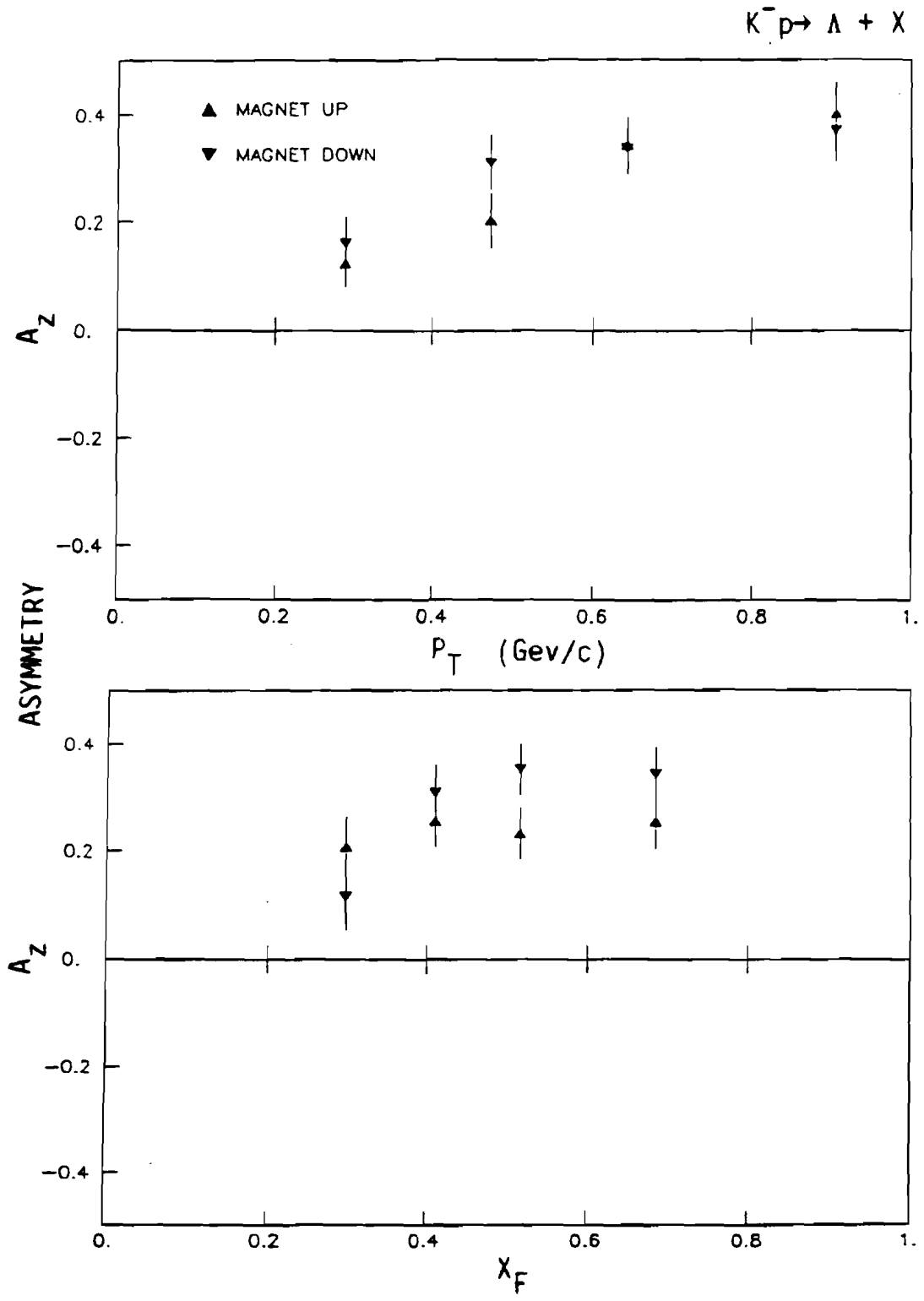

Figure 4.17. Parity Conserving Asymmetry A_Z as a Function of P_T and X_F for $K^-p \rightarrow \Lambda$ Magnet Up/Magnet Down Data.

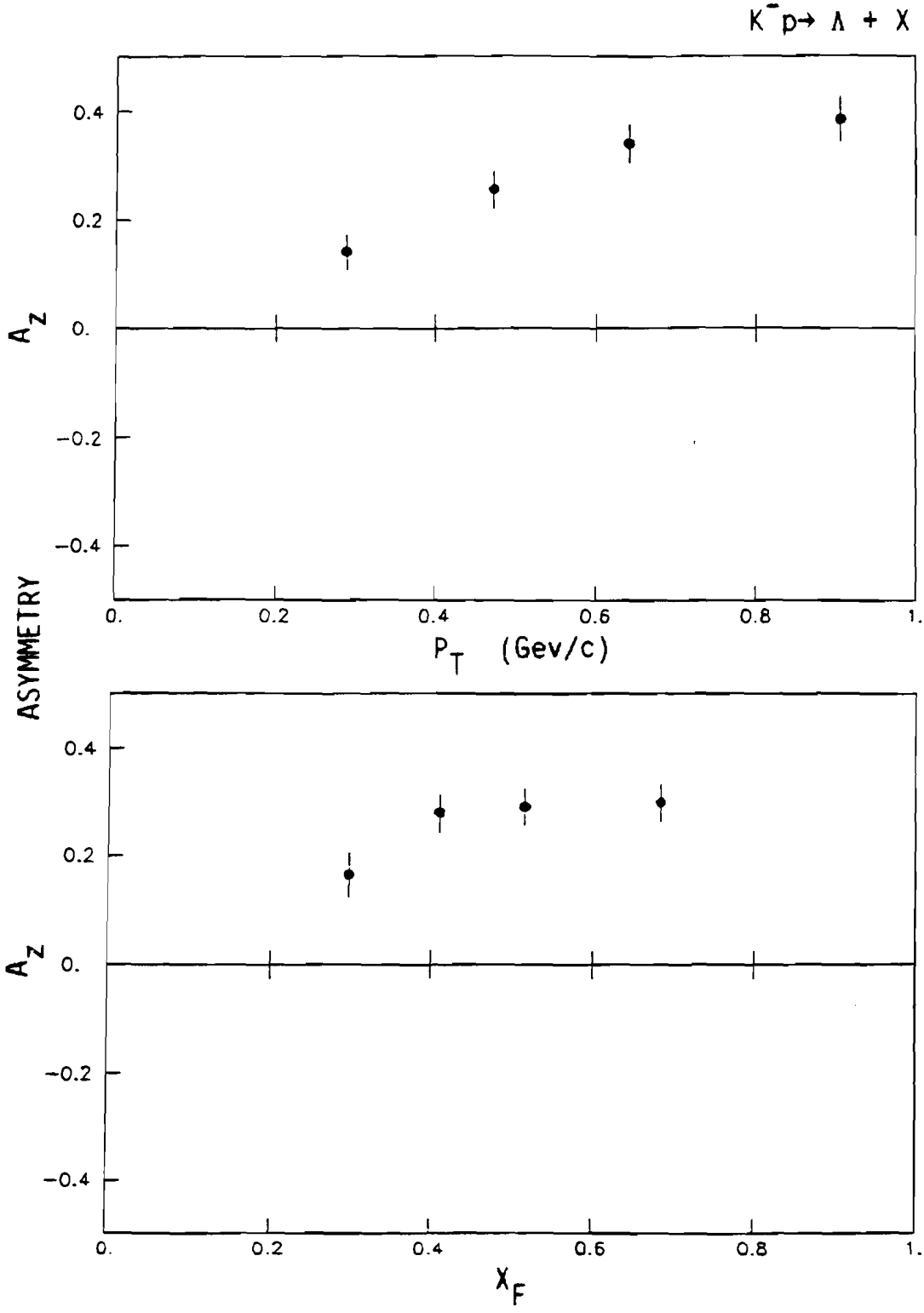

Figure 4.18. Parity Conserving Asymmetry A_Z as a Function of P_T and X_F for $K^-p \rightarrow \Lambda$ Combined Data.

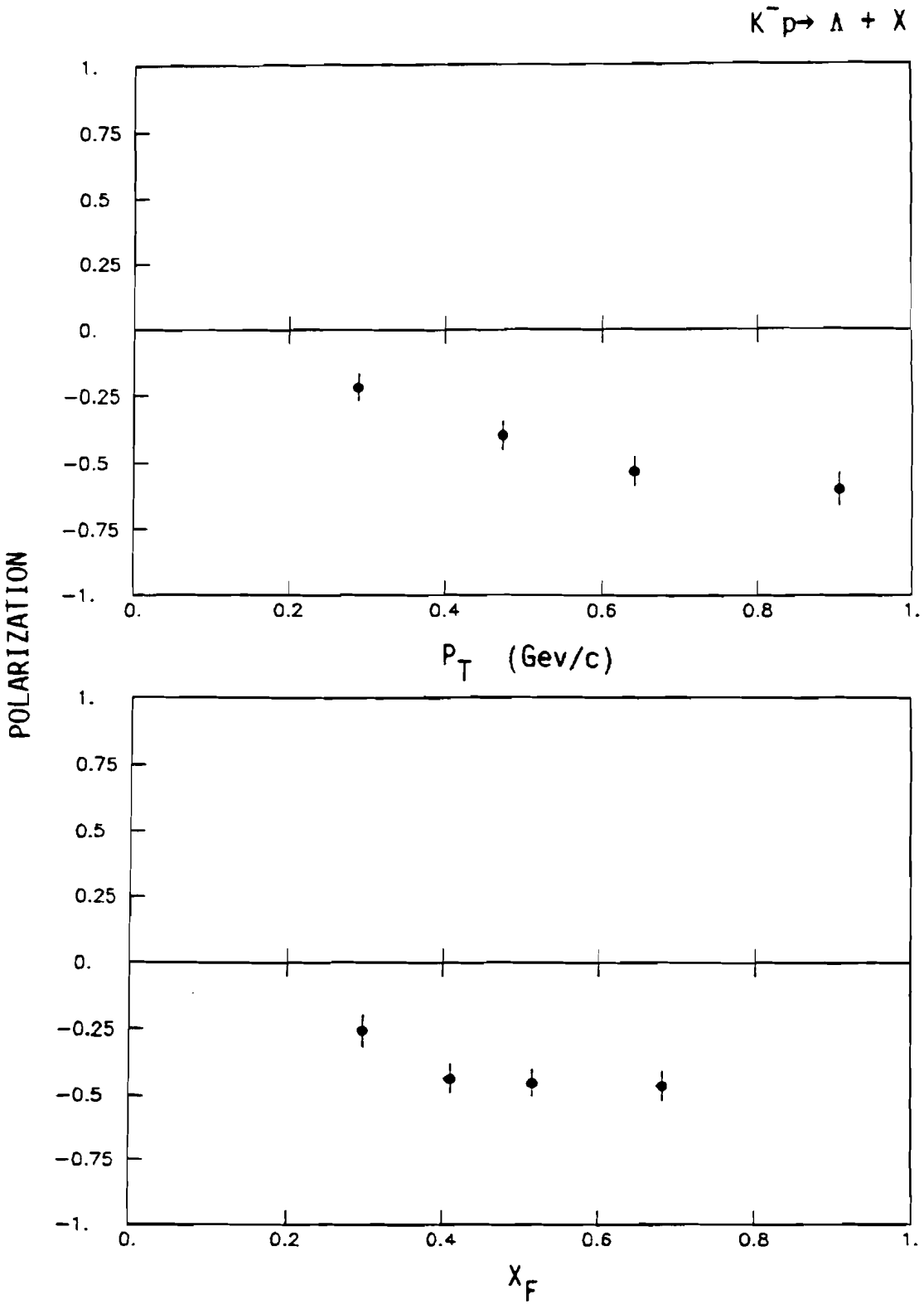

Figure 4.19. Polarization as a Function of P_T and X_F for $K^-p \rightarrow \Lambda$.

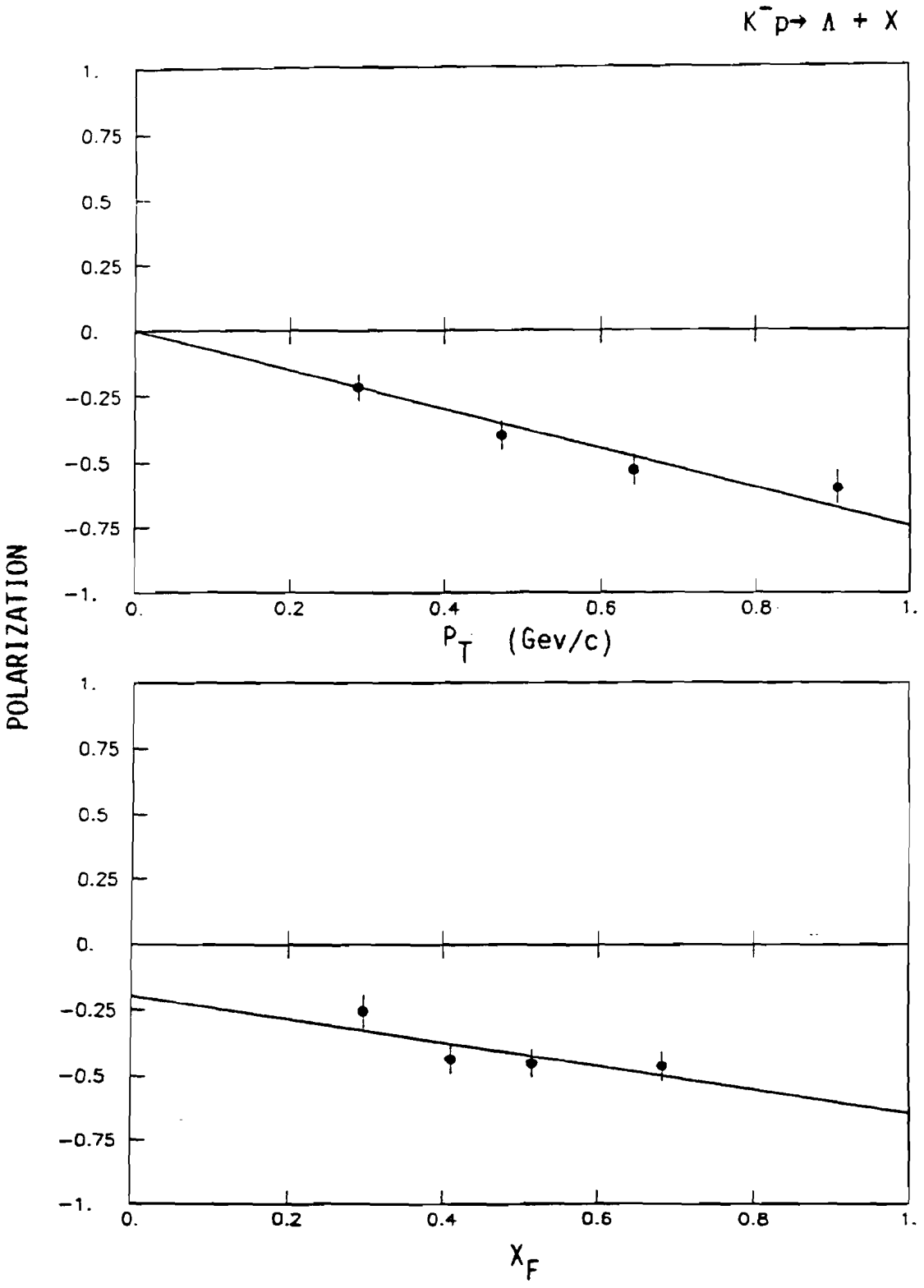

Figure 4.20. Polarization as a Function of P_T and X_F for $K^-p \rightarrow \Lambda$ with Fits.

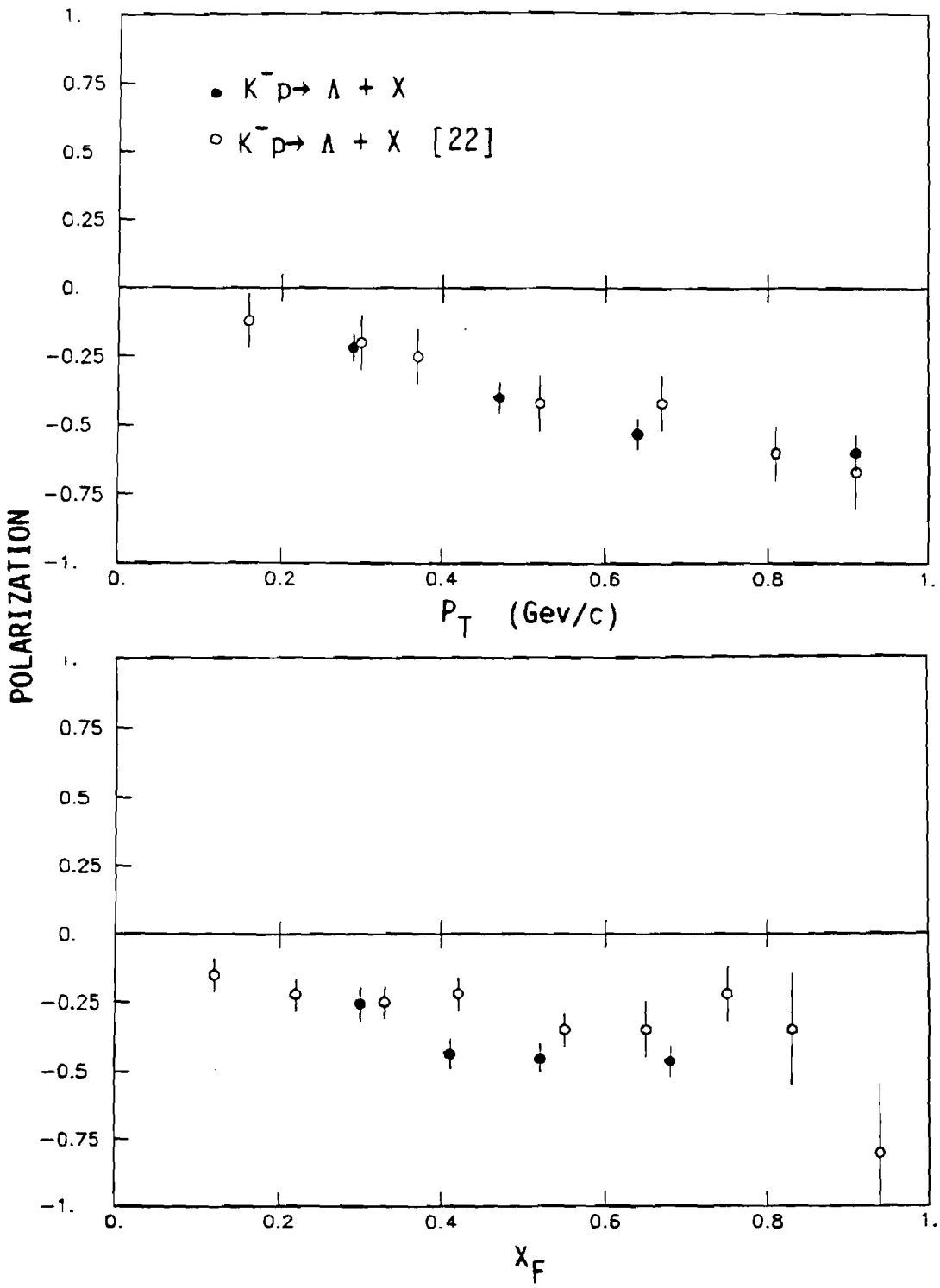

Figure 4.21. Comparison of Polarization for $K^-p \rightarrow \Lambda$ from this Experiment and Reference 22.

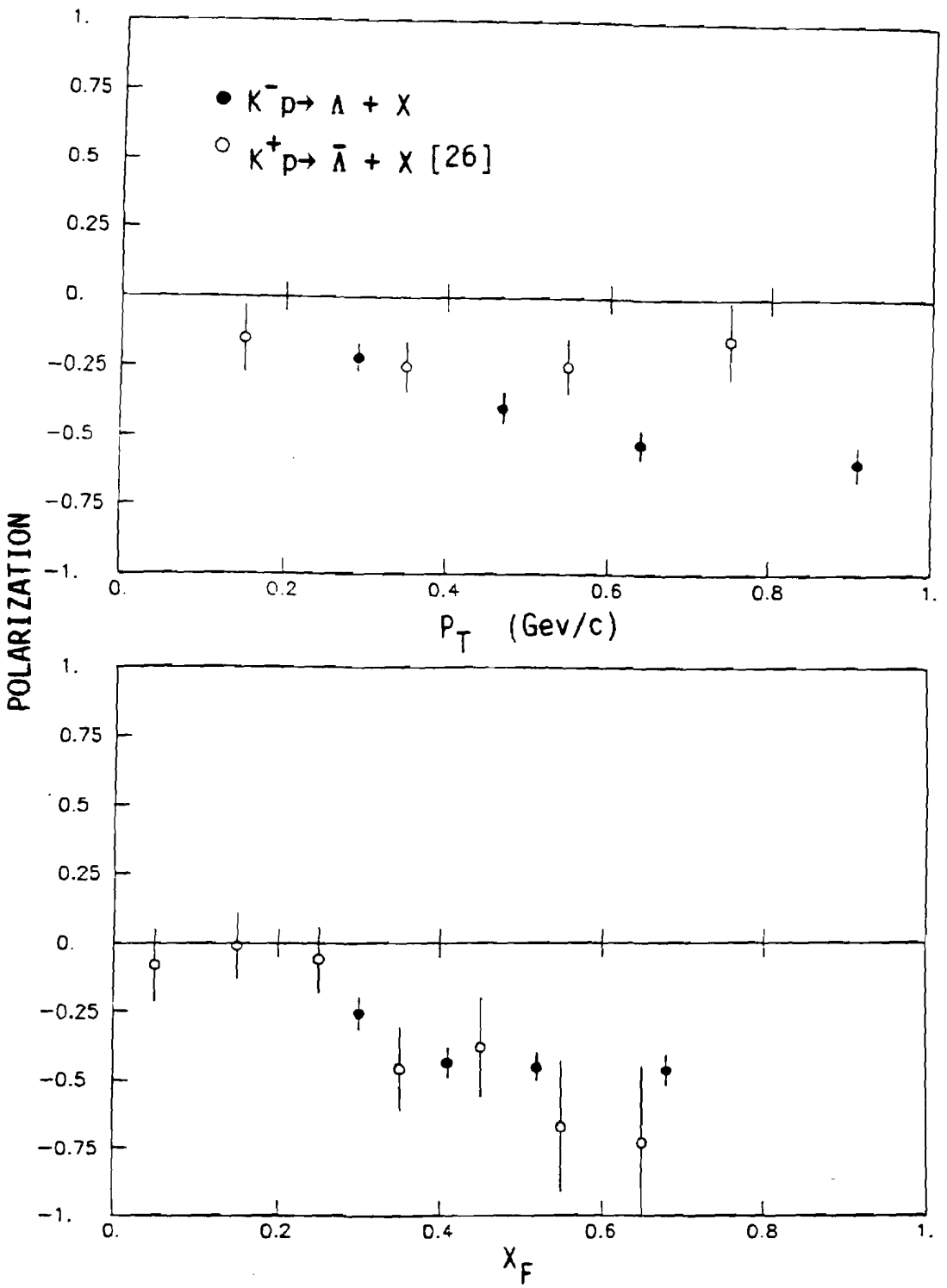

Figure 4.22. Comparison of Polarization for $K^-p \rightarrow \Lambda$ from this Experiment and $K^+p \rightarrow \bar{\Lambda}$ from Reference 26.

4.5 Systematic Errors/Backgrounds

The question of systematic errors has already been discussed in the study of biases which are one form of systematic effect. The results of the analysis of the parity nonconserving asymmetries A_x and A_y and the "polarization" of K^0_S's indicate no statistically significant systematic effects.

More direct investigations were performed by varying the field integral of the sweeping magnet, the upstream-downstream spectrometer alignment and the resolution of important kinematic parameters. Again, there were no significant effects observed. However, these methods are not sensitive to infiltration of the Λ or $\bar{\Lambda}$ sample by K^0_S's reconstructed as Λ or $\bar{\Lambda}$ and non-direct Λ or $\bar{\Lambda}$'s.

K^0_S Background

Table 4.7 has the estimated K^0_S background in the Λ and $\bar{\Lambda}$ data for the three channels.

Table 4.7. K^0_S Background.

Channel	K^0_S Background
$\bar{p}\, p \to \bar{\Lambda}$	0.7%
$p\, p \to \Lambda$	0.7%
$K^- p \to \Lambda$	13.0%

The Monte Carlo generated distributions contained the estimated K^0_S backgrounds for each channel. The cosθ distribution for K^0_S's which were reconstructed as Λ or $\bar{\Lambda}$ was peaked at zero and symmetric and thus could not affect the value of the measured polarization. Monte Carlo tests were conducted in which the K^0_S/Λ ratio was varied even well outside reasonable limits and no statistically significant effect was found.

Non-Direct Λ's and $\bar{\Lambda}$'s

Another source of bias arises from Λ's or $\bar{\Lambda}$'s coming from Σ^0 or $\bar{\Sigma}^0$ decay which are included in the data sample. On the average the polarization of Λ's or $\bar{\Lambda}$'s from Σ^0 or $\bar{\Sigma}^0$ decays is $-\frac{1}{3}P(\Sigma^0/\Sigma^{\bar{0}})$ [27]. The measured polarization may be expressed by

$$P(\Lambda)_{meas} = P(\Lambda)_{direct} \frac{\sigma(\Lambda_{direct})}{\sigma(\Lambda_{tot})} - \frac{1}{3} P(\Sigma^0) \frac{\sigma(\Sigma^0)}{\sigma(\Lambda_{tot})} \quad .$$

The ratio of inclusive cross sections $\frac{\sigma(\Sigma^0)}{\sigma(\Lambda_{tot})}$ is approximately 0.3 for K^-p reactions at 8.25 GeV/c [28] and for protons on beryllium at 28 GeV/c the ratio is ~ 0.26 [29]. These ratios are approximately independent of P_T and X_F. Making the further assumptions that the ratios are independent of energy, that the acceptance for Λ's from Σ^0's is the same as for directly produced Λ's and the ratio for $\bar{p}p$ interactions is the same, then the measured polarization is given by

$$P(\Lambda)_{meas} = \frac{2}{3} P(\Lambda)_{direct} - \frac{1}{9} P(\Sigma^0).$$

which is valid for $pp \to \Lambda$, $K^-p \to \Lambda$ and $\bar{p}p \to \bar{\Lambda}$.

It then remains only to insert the polarization of Σ^0 or $\bar{\Sigma}^0$s to obtain the direct Λ or $\bar{\Lambda}$ polarization.

The polarization of Σ^0's produced by protons has been measured by [30] and is approximately the same magnitude but is opposite in sign to the measured polarization of Λ's produced by protons. Therefore the polarization of directly produced Λ's is

$$P_{\text{direct}}(pp\to \Lambda) = \frac{4}{3} P_{\text{meas}}(pp\to \Lambda)$$

Previous experiments that measured the polarization of Λ's produced by protons were not able to correct for the $\Sigma^0\to \gamma\Lambda$ background since at that time the polarization of Σ^0's was unknown. The Σ^0 background is however significant. Figure 4.23 shows the fit to the measured polarization of Λ's produced by protons from this experiment and the "corrected" polarization as a function of P_T.

The polarization of Σ^0 or $\bar{\Sigma}^0$ produced by K^- or $\bar{p}$ is not known and can in principle range between -1 and +1. The polarization of directly produced Λ's or $\bar{\Lambda}$'s from incident K^-'s or $\bar{p}$'s would be given by

$$\left(P_{\text{meas}}(\Lambda/\bar{\Lambda}) - \frac{1}{9}\right)\frac{3}{2} \le P_{\text{direct}}(\Lambda/\bar{\Lambda}) \le \left(P_{\text{meas}}(\Lambda/\bar{\Lambda}) + \frac{1}{9}\right)\frac{3}{2}.$$

Given the large magnitude of the $K^-p\to \Lambda$ polarization and a non-direct Λ background from Σ^0's of 30% it is possible to set limits on $P_{\text{direct}}(K^-p\to \Lambda)$ and the polarization of Σ^0's produced by K^- which depends on the maximum value of $P_{\text{meas}}(K^-p\to \Lambda)$.

The expression

$$P(K^-p\to \Lambda)_{direct} = \frac{3}{2}P(K^-p\to \Lambda)_{meas} + \frac{1}{6}P(K^-p\to \Sigma^0)$$

is plotted in Figure 4.24 for three values of $P(K^-p\to \Lambda)_{meas}$ which are consistent with the results of this experiment. For $P(K^-p\to \Lambda)_{meas} = -0.6$, which is the largest measured value, and $P(K^-p\to \Sigma^0)$ negative the polarization of directly produced Λ's is greater than 90%. If instead the linear fit is extrapolated to $P_T = 1.0$ GeV/c then $P(K^-p\to \Lambda)_{meas} = -0.75$ and the polarization of directly produced Λ's is greater than 95% and the Σ^0 polarization must be positive and greater than 70%. The Σ^0 polarization would be positive for a threshold value of $P(K^-p\to \Lambda)_{meas} \leq -0.67$. At any value for the Σ^0 polarization the polarization of Λ's produced by K^-'s is exceedingly large.

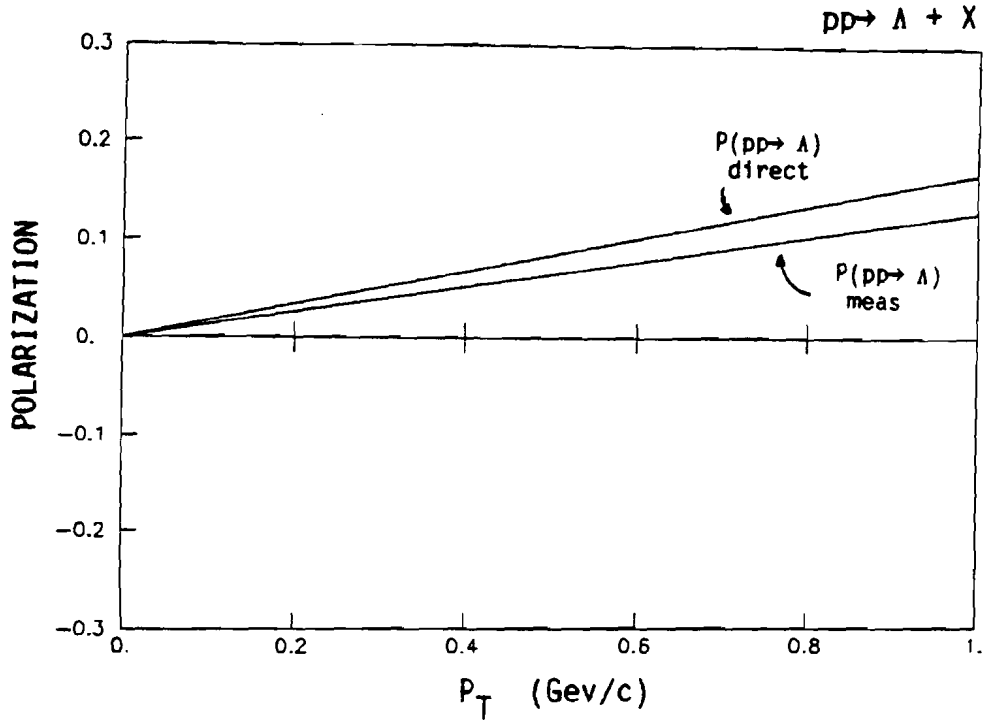

Figure 4.23. Measured and Direct Polarization as a Function of P_T for pp→ Λ.

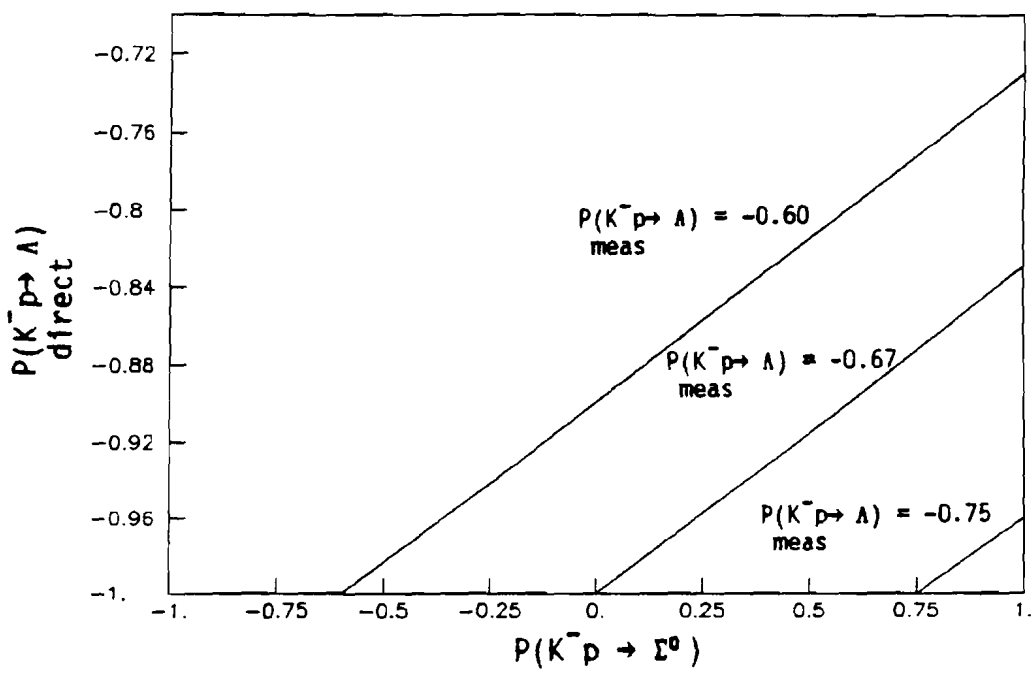

Figure 4.24. Polarization of Λ's and Σ^0's Produced by K^- for Possible Values of the Measured Λ Polarization.

4.6 Discussion

The polarization of Λ's produced via two-body scattering at low energies is a well known and reasonably understood phenomenon. However, the discovery of Λ polarization in 300 GeV/c inclusive $pp \rightarrow \Lambda$ interactions at Fermilab [31] is evidence that spin also plays an important role at high energies. This was an unexpected result considering the opinion at the time that the increasing number of amplitudes through which the final state is created would preclude significant polarization [32].

Hyperon polarization has been observed in many production channels in addition to those studied in this experiment. A partial list is given below:

$pp \rightarrow \Lambda, \bar{\Lambda}$	[33]
$K^+p \rightarrow \bar{\Lambda}$	[34]
$pp \rightarrow \Sigma^0$	[35]
$pp \rightarrow \Sigma^+, \Sigma^-$	[36,37]
$pp \rightarrow \Xi^0, \Xi^-$	[38,39]

It is clear that polarization is a pervasive phenomenon in inclusive hyperon production and that any serious model must be able to explain the existence of polarization wherever it manifests itself.

The Triple-Regge model has been successful in describing Λ production in the low P_T region but can only accommodate polarization effects of the order of 5% [40] compared to the measured values of greater than 20%. It has been applied to $K^-p \rightarrow \Lambda$ interactions by S.U. Chung et al., [41] and others [42,43,44]. Each of the numerous channels

in which polarization is observed requires a unique treatment not in line with the global nature of the phenomenon. Thermodynamic and statistical models used to describe low P_T interactions are incapable of producing polarization. The observation of large polarization effects suggests that the mechanism involved in high energy low P_T interactions is not as complicated as was once believed. By its very nature polarization indicates that the hadronization process must be relatively simple since its existence requires information between the incoming and outgoing particle be preserved. This implies that polarization effects in low P_T interactions could be described in terms of a constituent model.

At the opposite end of the kinematic spectrum is the current favorite constituent model for describing strong interactions, Quantum Chromodynamics or QCD. In a calculation involving perturbative QCD, Kane, Pumplin and Repko [45] have shown that for $P_T > 4\text{-}5$ GeV/c, where QCD is assumed to be valid, the polarization in hadron interactions goes to zero. Conventional Quantum Chromodynamics is not a viable alternative since effects at low P_T are not calculable, but it will be interesting to see if the prediction of zero polarization at high P_T holds.

A set of models which attempt to explain polarization phenomena in the P_T range below where QCD is valid are based on the interaction of the strange quark which forms the Λ and the quark-gluon field. In these models the Λ is pictured as being composed of a u-,d-, and an s-quark where the u and d form a spin singlet and the spin of the Λ is determined by the spin of the s-quark.

Szwed [46] postulates that polarization arises by scattering of the s-quark in the external color-field. An expression for the polarization as a function of the s-quark mass, momentum, and scattering angle is obtained through a quantitative calculation which depends on the strong coupling constant and the external field. It's application is limited to exclusive and semi-exclusive production processes and the predictions that the model would make for the inclusive interactions presented here are not clear.

Andersson, Gustafson and Ingelman [47,48] explain the observed polarization effects seen in $pp \rightarrow \Lambda$ interactions by considering the process of producing an s-$\bar{s}$ pair in a confined color field. Based on the assumption of a string field which has no transverse degrees of freedom they use local angular momentum conservation and Thomas precession to produce polarized s and $\bar{s}$ quarks. This mechanism does not work for valence s-quarks such as in $K^- p \rightarrow \Lambda$ interactions, and additional arguments are needed to explain polarization.

The disadvantage of the above two models is that their predictions depend on a specific process to generate polarization effects.

A more useful model in terms of comparing polarization results has been proposed by DeGrand and Miettinen [49], discussed in Section 1.2. They formulate a rule, based on the observed polarization in inclusive $pp \rightarrow \Lambda$ and $pp \rightarrow \Sigma^+$ interactions, that slow partons recombine with spins down in the scattering plane ($\bar{p}_{beam} \times \bar{p}_\Lambda$) while fast partons preferentially recombine with spins up. Then by using SU(6) symmetry they can relate polarizations in inclusive baryon production. The slow spins down - fast spins up rule is explained if the s-quark undergoes Thomas precession during formation of the hyperon. The sign of the

polarization depends on the relative acceleration of the s-quark and the ud pair that form the Λ. In the case of $pp \rightarrow \Lambda$ for example, there is no relative acceleration since the u-bar, d-bar and s-bar all come from the sea and consequently $\bar{\Lambda}$'s from protons should not be polarized. This has been shown experimentally by Lundberg [50].

The predictions of the three constituent interchange models discussed above are in many respects similar though the specific mechanisms responsible are in detail quite different. They all predict a dependence on P_T and weak dependence on X_F.

The dynamical mechanisms proposed in the above three models are suspect in that they rely on too many assumptions relative to the predictive power. Detailed examination of the mechanisms proposed to explain polarization indicates that the dynamical origin of the effect is still an open question. The most useful results come from the straightforward relationships obtained by incorporating the simple rule proposed by DeGrand and Miettinen and SU(6) symmetry which are independent of the source of the polarization.

The results of this experiment are summarized in Figure 4.25. The polarization of Λ's ($\bar{\Lambda}$'s) produced by protons (anti-protons) has the same sign and qualitatively the same increase as a function of P_T. In contrast, the polarization of Λ's produced by K^-'s is opposite in sign and has a magnitude several times greater than the baryon-baryon channels. Discussion of the X_F dependence is difficult given the limited range examined in this experiment. The polarization for $pp \rightarrow \Lambda$ and $\bar{p}p \rightarrow \bar{\Lambda}$ is consistent with a non-zero value only well into the beam fragmentation region whereas for $K^-p \rightarrow \Lambda$ the polarization is significant at a lower value of X_F.

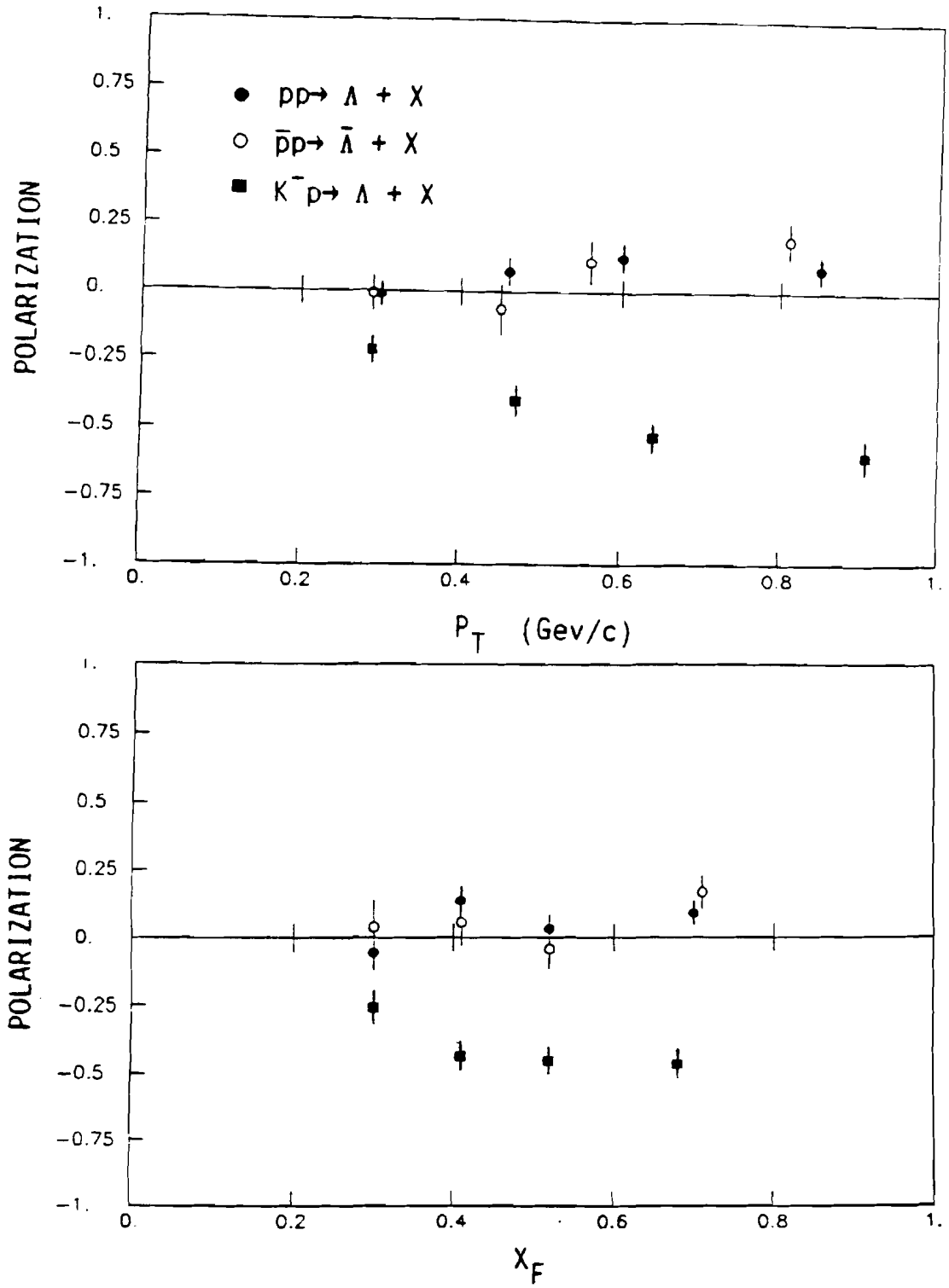

Figure 4.25. Summary of Polarization Results.

The sign of the polarization observed in the production channels of this experiment as well as those of other inclusive baryon channels studied to date is explained by DeGrand and Miettinen's slow spins down - fast spins up rule. Andersson, Gustafson and Ingelman along with DeGrand and Miettinen can obtain an absolute sign for a variety of interactions by using Thomas precession of the strange quark as part of two relatively different mechanisms by showing that one spin state is favored over another.

One of the more important features of Λ and $\bar{\Lambda}$ polarization, beyond the fact of its existence, is the energy independence which is exhibited in comparisons with previous experiments. This experiment presents the first measurement of polarization at high energy for the production channel $K^-p \rightarrow \Lambda$. The data for this channel have been compared to previous results for the reactions $K^-p \rightarrow \Lambda$ at 8.25 GeV/c [51] and $K^+p \rightarrow \bar{\Lambda}$ at 70 GeV/c [52] and found to be in qualitative agreement. The baryon-baryon channels, $pp \rightarrow \Lambda$ and $\bar{p}p \rightarrow \bar{\Lambda}$, compare favorably with previous results at different energies ([53] and [54] respectively). Since polarization is a function of the kinematical variables P_T and X_F care should be taken when making detailed comparisons with other experimental results. The important fact remains however that polarization effects persist strongly at high energy. The energy independence for the $K^-p \rightarrow \Lambda$ channel is discussed in terms of the Triple-Regge model in [55,56], however description of the other features of polarization seem overly contrived [57,58,59]. Some attempts are made to relate the scaling of inclusive cross sections to the scaling observed in polarization phenomena [60] but a study of Λ polarization and production at large P_T [61] has shown that distinct changes in the behavior of the polarization as a function

of P_T do not imply a corresponding change in the cross section.

A dependence of the polarization on transverse momentum is explained by the constituent models as a "trigger bias effect". By selecting Λ's with a given P_T a sample of events is chosen where the transverse momentum of the s-quark or diquark is in the same direction as the transverse momentum of the Λ. Polarization will arise if there is a correlation between the spin and the transverse momentum of the recombining quark.

Only a weak X_F dependence is expected by any of the constituent models due to the large difference in energy between the valence and sea quarks which form the Λ. Zero polarization for the baryon-baryon channels studied in this experiment at low X_F might be expected to be due to the increased number of soft production mechanisms that dominate that region. The stronger polarization at low X_F for $K^-p \rightarrow \Lambda$ may be explained by the fact that the s-quark, which determines the polarization of the Λ, is the leading particle.

None of the above models can make absolute predictions of the magnitude of the polarization. All rely on the input of known results. For channels studied in this experiment DeGrand and Miettinen predict that:

$$P(pp \rightarrow \Lambda) = P(\bar{p}p \rightarrow \bar{\Lambda}) = -P(K^-p \rightarrow \Lambda).$$

The $pp \rightarrow \Lambda$ and $\bar{p}p \rightarrow \Lambda$-bar data agree in magnitude but the polarization for $K^-p \rightarrow \Lambda$ is several times that of the baryon-baryon channels contrary to the model predictions. At a P_T of 0.8 GeV/c the measured value of the polarization is 60% which is much larger than expected by any current model. This value is consistent with the results of $K^-p \rightarrow \Lambda$ data at much

lower energy [62] and also the $K^+p \rightarrow \bar{\Lambda}$ channel [63] where the $s(\bar{s})$-quark is the leading particle.

The contribution of non-direct Λ's or $\bar{\Lambda}$'s has been shown to have a significant effect on the polarization results. The magnitude of the effect cannot be determined for $K^-p \rightarrow \Lambda$ and $\bar{p}p \rightarrow \bar{\Lambda}$ until the polarization for $K^-p \rightarrow \Sigma^0$ and $\bar{p}p \rightarrow \bar{\Sigma}^0$ has been measured. The polarization of $K^-p \rightarrow \Lambda$ would still greatly exceed that of $pp \rightarrow \Lambda$ even taking into consideration the most extreme background contribution. Depending on the polarization of Σ^0's produced by K^-'s the polarization of directly produced Λ's could range from 75 - 100%. None of the models presented here implicitly take into account the effects of non-direct background. Production of Λ's with low X_F is probably dominated by non-direct mechanisms which contribute to the X_F dependence in that region. This is another possible explanation of the difference in the X_F dependence observed between the baryon-baryon channels and $K^-p \rightarrow \Lambda$. Clearly, any detailed comparison of polarization data must take into account the non-direct background as a function of energy, P_T and X_F.

The results of this experiment are striking and simple yet no model exists which can explain the data quantitatively. Both the Triple-Regge description and Quantum Chromodynamics which cover the kinematic extremes fail to adequately describe inclusive polarization phenomena. The existence of substantial polarization at high energy and low momentum transfer has shown that quark dynamics plays an important role in the hadronization process in this kinematic region.

The relative signs of the hyperon polarizations can be accounted for using the models of DeGrand and Miettinen [64] and Andersson, Gustafson and Ingelman [65,66] but no satisfactory explanation for the

dynamical origin of the polarization yet exists. Furthermore, the large polarization observed in this experiment for the $K^- p \rightarrow \Lambda$ channel is totally unexpected. Any future models must explain the large difference in the magnitude of the polarization when the s-quark is valence as opposed to when it comes from the sea. The lack of quantitative theoretical success is impetus for further study of polarization phenomena and adds to the list of important variables that can be used in the study of inclusive interactions.

ACKNOWLEDGEMENTS

I would like to express appreciation to the following people who helped make this endeavor a success.

My friend and mentor Phil Yager, for his guidance and support. I consider our relationship a valuable part of my years in graduate school. It has had an undeniable and beneficial influence on my evolution as a person and a physicist.

My fellow graduate student Harry Melanson, for discussions and arguments which led inevitably to useful solutions and whose friendship was an unexpected bonus which I hope will continue unabated into the future.

Hans Kobrak from whom I learned the importance of what it means to do things right.

The other members of the collaboration, Bob Swanson, Maris Abolins, Bill Francis, Dan Owen and Ken Edwards for their help and interest, and Werner DeRosario for pulling all those night shifts.

I would especially like to thank my wife Treva for her endurance, patience and most of all her support, both moral and monetary, throughout this long and sometimes arduous process.

My family for their understanding and encouragement despite their lack of comprehension as to why I did this.

Finally, my son Matthew, who unknown to him provided the final impetus needed to finish this project.

REFERENCES

1. G. Bunce et al., Phys. Rev. Lett. 36, 1113 (1976).

2. C.G. Wohl et al., (Particle Data Group), Rev. Mod. Phys. 56, (1984).

3. T. DeGrand and H. Miettinen, Phys. Rev. D23, 1227 (1981).

4. B. Andersson, G. Gustafson and G. Ingelman, Phys. Lett. 85B, 417 (1979).

5. J. Szwed, Phys. Lett. 105B, 403 (1981).

6. K. Heller et al., Phys. Rev. Lett. 41, 607 (1978).

7. S.U. Chung et al., Phys. Rev. 11, 10[illegible] (1975).

8. R.J.N. Phillips, G.A. Ringland and R.P. Worden, Phys. Lett. 40B, 239 (1972).

9. H.G.E. Kobrak, R.E. Pitt and R.A. Swanson, Fermilab TM-597, (1975).

10. Model WCS-200 Wire Chamber Scanner. Manufactured and available from: Nanometric Systems, Inc. 837 North Cuyler Avenue, Oak Park, Il. 60302.

11. M. Abolins et al., Nucl. Instrum. Methods, 192, 331 (1982).

12. T.F. Droege, M.M. Watson and T.R. Wesson, IEEE Trans. Nucl. Sci. NS-23 No.1 , 248 (1976)

13. C.M. Ma et al., MIT Technical Report 129 (1982).

14. S. Goudsmit and J. Saunderson, Phys. Rev. 57, 24 (1940).

15. C.G. Wohl, op. cit.

16. Ibid

17. G. Bunce et al., op. cit.

18. K. Heller et al., op. cit.

19. H. Becker et al., Nucl. Phys. B141, 48 (1978).

20. P. Chauvat et al., CERN preprint, CERN-EP/83-104, 1983).

21. M.L. Faccini-Turluer et al., Z. Phys. C1, 19 (1979).

22. M. Baubillier et al., Nucl. Phys. B148, 1 (1979).

23. H. Abramowicz et al., Nucl. Phys. B105, 222 (1976).

24. H. Grassler et al., Nucl. Phys. B136, 386 (1978).

25. S.U. Chung et al., op. cit.

26. I.V. Ajinenko et al., Phys. Lett. 121B, 183 (1983).

27. R. Gatto, Phys. Rev. 109, 610 (1957).

28. M. Baubillier et al., op. cit.

29. Marilyn W. Sullivan et al. Phys. Lett. 142B, 451 (1984

30. E.C. Dukes, Ph.D. thesis, University of Michigan, 1984.

31. G. Bunce et al., op. cit.

32. G. Giacomelli, Phys. Rep. 23C, 123 (1976).

33. B. Lundberg, Ph.D. thesis, University of Wisconsin-Madison, 1984.

34. I.V. Ajinenko et al., op. cit.

35. E.C. Dukes, op. cit.

36. P . Cooper, in Proceedings of the 1982 gh Energy Spin Physics Conference, edited by G.M. Bunce (Brookhaven National Laboratory, 1982), pp. 102-107.

37. C. Wilkinson et al., Phys. Rev. Lett. 46, 803 (1981).

38. Oliver E. Overseth, in High Energy Physics with Polarized Beam and Polarized Targets, Proceedings of the 30 International Symposium, Lausanne, edited by C. Joseph and J. Soffer (Basel, Switzerland, Birkhauser). 1981.

39. K. Heller et al., Phys. Rev. Lett. 51, 2025 (1983).

40. F. Paige, D. Sidhu, Phys. Rev. D14. 2307 (1976).

41. S.U. Chung et al., op. cit.

42. H. Abramowicz et al., op. cit.

43. H. Grassler et al., op. cit.

44. M.L. Faccini-Turluer et al., op. cit.

45. G.L. Kane, J. Pumpin and W. Repko, Phys. Rev. Lett. 1389 (1978).

46. J. Szwed, op. cit.

47. B. Andersson, G. Gustafson and G. Ingelman, op. cit.

48. G. Gustafson, in Proceedings of the 1982 High Energy in Physics Conference, edited by G.M. Bunce (Brookhaven National Laboratory, 1982), pp. 355-358.

49. T. DeGrand and H. Miettinen, op. cit.

50. B. Lundberg, op. cit.

51. M. Bellier et al., op. cit.

52. I.V. Ajinenko et al., op. cit.

53. K. Heller et al., Phys. Rev. Lett. 41, 607 (1978).

54. P. Chauvat et al., op. cit.

55. S.U. Chung et al., op. cit.

56. H. Abramowicz et al., op. cit.

57. F. Paige, D. Sidhu, Phys. Rev. D14, 2307 (1976).

58. K. Moriarty et al., Nuovo Cimento 17, 366 (1976).

59. M. Baubillier et al., op. cit.

60. I.V. Ajinenko, op. cit.

61. B. Lundberg, op. cit.

62. M. Baubillier et al., op. cit.

63. I.V. Ajinenko et al., op. cit.

64. T. DeGrand and H. Miettinen, op. cit.

65. B. Andersson, G. Gustafson and G. Ingelman, op. cit.

66. G. Gustafson, op. cit.